

Contributions to modelling actinide transport in potential host rock formations: Elementary processes and influence of heterogeneous structures

Holger Lippold, Johannes Kulenkampff, Marion Gründig, Abdelhamid Zakhnini

Helmholtz-Zentrum Dresden-Rossendorf (HZDR)
Institut für Radiochemie
Forschungsstelle Leipzig*
Permoserstr. 15, 04318 Leipzig

ABSCHLUSSBERICHT

Vorhabensbezeichnung:

„Beiträge zur Modellierung des Actinidentransports in potentiellen Wirtsgesteinsformationen – Teilthema 1: Mobilitätsbestimmende Elementarprozesse des huminstoffgebundenen Transports, Teilthema 2: Einfluss der heterogenen Struktur auf den Lösungs- und Kolloidtransport“

Förderkennzeichen: 02E10176

Berichtszeitraum: 01.07.2006 bis 30.06.2011

Projektleiter: Dr. H. Lippold

Teilprojekt im Rahmen des Verbundvorhabens

„Wechselwirkung und Transport von Actiniden im natürlichen Tongestein unter Berücksichtigung von Huminstoffen und Tonorganika“

Leipzig, Dezember 2011

* bis Dezember 2009: Institut für Interdisziplinäre Isotopenforschung (IIF)

Das diesem Bericht zugrunde liegende Vorhaben wurde mit Mitteln des Bundesministeriums für Wirtschaft und Technologie unter dem Förderkennzeichen 02E10176 gefördert. Die Verantwortung für den Inhalt dieser Veröffentlichung liegt bei den Autoren.

Kurzfassung

Die wesentliche Zielsetzung des Gesamtvorhabens bestand in der Bereitstellung von Bewertungsgrundlagen zur Abschätzung des Einflusses natürlicher organischer Komplexbildner auf die Mobilität von Actiniden in Tongestein als möglicher Endlagerformation. Ein Schwerpunkt lag auf der Hinterfragung der Gültigkeit vereinfachender Prozessvorstellungen bei der Modellierung huminstoffgebundener Transportvorgänge. Durch Nutzung des analytischen Potentials von Radiotracerverfahren und spektroskopischen Sondenmethoden wurden die maßgeblichen Wechselwirkungsprozesse innerhalb des ternären Systems Metall / Huminstoff / Tongestein eingehend untersucht. Fragen der Verknüpfung von Elementarprozessen waren dabei ebenso zu betrachten wie die Reversibilität von Adsorptionsvorgängen und kinetische Effekte in der Metall-Huminstoff-Komplexbildung.

Umfangreiche Adsorptionsstudien mit Opalinuston und anderen Tonmaterialien haben gezeigt, dass sowohl Huminstoffe als auch niedermolekulare Tonorganika einer Desorption von Metallen bei pH-Wert-Abnahme prinzipiell entgegenwirken. Dies kann auf die pH-Abhängigkeiten der Wechselwirkungen in den binären Randsystemen zurückgeführt werden, lässt sich jedoch nicht quantitativ anhand der zugehörigen Verteilungskoeffizienten beschreiben. Entsprechende Annahmen zur linearen Additivität von Einzelprozessen in Transportmodellen müssen daher grundsätzlich für das jeweilige System verifiziert werden.

Der dynamische Charakter der Adsorption von Huminstoffen konnte in Traceraustausch-Studien erstmals direkt nachgewiesen werden, obwohl Desorptionsversuche zunächst nicht auf einen reversiblen Prozess hindeuteten. Der Austausch im Sättigungszustand erfordert allerdings wesentlich mehr Zeit als die Einstellung des Adsorptionsgleichgewichts. Die Adsorptionskinetik ist somit kein zuverlässiges Kriterium, um die Bedingungen für ein ständiges Gleichgewicht in Fließsystemen abzuschätzen.

Abweichend von gleichgewichtsthermodynamischen Modellansätzen ist die Huminstoffkomplexbildung mehrwertiger Metalle durch Stabilisierungsprozesse über längere Zeiträume gekennzeichnet, in deren Ergebnis sich auch Konkurrenzeffekte verstärken. Diese Phänomene müssen in Experiment und Modell berücksichtigt werden. Das notwendige Verständnis der zugrunde liegenden Vorgänge auf molekularer Ebene konnte wesentlich verbessert werden.

Gleichrangig mit chemischen Wechselwirkungen auf molekularer Skala müssen die Transporteigenschaften des realen Barrierematerials untersucht werden, da diese den tatsächlichen Retardationseffekt der Wechselwirkung determinieren. Da auf jeder Größenskala transportbestimmende Strukturen vorhanden sind, bestimmen deren Skalierungseigenschaften zugleich die Übertragung von der molekularen auf die makroskopische Skala.

So wurden im Rahmen eines weiteren Aufgabenpaketes Transportstudien an möglichen Barrierematerialien (Tonen und Kristallingestein) durchgeführt. Hierzu wurde die GeoPET-Methode eingesetzt, die eine äußerst selektive und extrem empfindliche Konzentrationsbestimmung für radiomarkierte chemische Spezies in Raum und Zeit mit geeigneter Auflösung ermöglicht. Durch die Beschaffung eines

hochauflösenden PET-Scanners konnten die experimentellen Bedingungen gegenüber dem bisher genutzten Human-PET-Scanner und einer Eigenentwicklung optimiert werden. Es zeigte sich aber, dass die deutlich höhere Auflösung und Empfindlichkeit einen höheren Aufwand bei der Korrektur von materialbedingten Abbildungsfehlern erfordert.

Mit Hilfe des GeoPET-Verfahrens konnte die Ausbreitung konservativer Tracer durch Advektion in geklüftetem Kristallingestein und in gering kompaktierten Tonen quantitativ abgebildet werden. Der gemessene räumlich-zeitliche Verlauf der Tracerausbreitung zeigt vergleichbare Eigenschaften wie Transportsimulationen am selben Material, wenn ausreichend genaue Strukturinformationen vorliegen. In allen anderen Fällen weisen deutliche Abweichungen zwischen Modell und Beobachtung auf die besondere Bedeutung der Berücksichtigung heterogener Materialstrukturen hin.

Für die Beobachtung rein diffusiver Stoffausbreitung in Bohrkernen wurde ein Verfahren entwickelt, das geeignet ist, Anisotropie und präferentielle Wegsamkeiten nachzuweisen. Dabei stellte sich heraus, dass sich der Ausbreitungsprozess in realen, druckentlasteten Tonbohrkernen aufgrund der Teilsättigung deutlich komplizierter darstellt als reine molekulare Diffusion. Derartige Bedingungen sind in-situ relevant und in Auflockerungszonen ebenfalls zu erwarten.

Das Projekt war Bestandteil des Verbundvorhabens „Wechselwirkung und Transport von Actiniden im natürlichen Tongestein unter Berücksichtigung von Huminstoffen und Tonorganika“ (Förderkennzeichen 02E10156, 02E10166, 02E10176, 02E10186, 02E10196, 02E10206, 02E10216) unter Beteiligung folgender Einrichtungen:

- Helmholtz-Zentrum Dresden-Rossendorf (HZDR), Institut für Radiochemie
- Johannes-Gutenberg-Universität Mainz, Institut für Kernchemie
- Karlsruher Institut für Technologie (KIT), Institut für Nukleare Entsorgung
- Universität des Saarlandes, Institut für Anorganische und Analytische Chemie und Radiochemie
- Universität Potsdam, Institut für Chemie – Physikalische Chemie
- Technische Universität München, Fachgebiet Theoretische Chemie

Die Abschlussberichte zu den einzelnen Projekten werden im Rahmen eines zusammenfassenden Gesamtberichtes durch KIT veröffentlicht.

Abstract

As a main objective of the project, a basis was to be provided which allows an evaluation of the influence of natural organic complexants on the mobility of actinides in clay rock as a possible geological host formation for a final repository. A major focus was placed on the critical assessment of the applicability of simplifying assumptions for modelling humic-bound transport. Taking advantage of the analytical potential of radiotracer techniques and spectroscopic probe methods, relevant interactions within the ternary system metal / humic substance / clay were investigated in detail. The question of linking elementary processes was considered, as was the reversibility of adsorption as well as kinetic effects in metal-humic complexation.

Extensive adsorption studies with Opalinus clay and other clay materials have shown that metal desorption on acidification is generally counteracted by humic substances as well as low-molecular-weight clay organics. This can be explained by the pH dependences of the interactions in the constituent binary subsystems, but it cannot be quantitatively described by means of the corresponding partition coefficients. Thus, the assumption of linear additivity for single processes in transport models must be verified for every individual system under consideration.

By means of tracer exchange studies, the dynamic character of adsorption of humic matter was directly proven for the first time, although desorption experiments did not indicate a reversible process. The exchange at surface saturation requires, however, much more time than attaining the overall adsorption equilibrium. Thus, adsorption kinetics is not a reliable criterion for assessing the conditions of a steady equilibrium in flow systems.

Deviating from modelling approaches on the basis of equilibrium thermodynamics, complexation of higher-valent metals with humic substances is characterised by long-term stabilisation processes, leading to an increase in competition effects as well. These phenomena need to be considered in experiment and model. The necessary understanding of the underlying processes on a molecular scale was significantly improved.

Transport properties of the real barrier material are equally relevant as are chemical interactions on the molecular scale because the actual retarding effect of these interactions is determined by the transport behaviour. A hierarchy of transport-determining structures is present over a large scale. Therefore, the transfer function from the molecular scale to the macroscale is governed by the scaling characteristics of these structures.

For this reason, we conducted transport studies with possible barrier materials (clays and crystalline rocks). We applied the GeoPET method, benefiting from its exceeding selectivity and extreme sensitivity for concentrations of radiolabelled chemical species, providing time-dependent tomographic images of the tracer concentration at due spatial resolution. The acquisition of a high-resolution PET scanner greatly improved the experimental conditions compared to the human-medical PET scanner and the in-house developed scanner applied before. It turned out, however, that the significant improvement in resolution and sensitivity required higher expenses for proper corrections of image artifacts induced by material properties.

By means of the GeoPET method, the propagation of conservative tracers by advection in jointed crystalline rocks and low-compacted clays was mapped quantitatively. The measured spatio-temporal evolution of the tracer concentration shows features comparable to transport simulations on the same material, provided that structural information is available at a sufficient precision. In all other cases, significant deviations between model and observation demonstrate the particular importance of a consideration of heterogeneous material structures.

Another method was developed for the observation of diffusive spreading of substances in drill cores, capable of establishing anisotropy and preferential transport pathways. These measurements revealed a more complex propagation process than pure molecular diffusion in real and decompressed clay cores, which is related to their partial saturation. Such conditions are relevant in-situ, and they are expected to be present in excavation-damaged zones as well.

The project was part of the joint project “Interaction and transport of actinides in natural clay rock considering humic substances and clay organic matter” (reference numbers 02E10156, 02E10166, 02E10176, 02E10186, 02E10196, 02E10206, 02E10216) of the following institutions:

- Helmholtz-Zentrum Dresden-Rossendorf (HZDR), Institut für Radiochemie
- Johannes-Gutenberg-Universität Mainz, Institut für Kernchemie
- Karlsruher Institut für Technologie (KIT), Institut für Nukleare Entsorgung
- Universität des Saarlandes, Institut für Anorganische und Analytische Chemie und Radiochemie
- Universität Potsdam, Institut für Chemie – Physikalische Chemie
- Technische Universität München, Fachgebiet Theoretische Chemie

The final reports of the individual projects will be published within the framework of a comprising report by KIT.

Table of contents

1. Introduction	7
2. Experimental	10
2.1. Materials	10
2.1.1. Humic materials	10
2.1.2. Radiochemicals	10
2.1.3. Clay materials	11
2.2. Methods	13
2.2.1. General remarks, analytical equipment	13
2.2.2. Quantitative determination of metal-humate complexation	13
2.2.3. Studies on adsorption / desorption	14
2.2.4. Laser fluorescence spectroscopy	15
2.2.5. Positron emission tomography (PET)	15
3. Results and discussion	23
3.1. Co-adsorption of Tb(III) and humic acid onto clay materials as a function of pH	23
3.1.1. Tb(III) adsorption in the absence and presence of humic acid	23
3.1.2. Adsorption of humic acid and humate complexation of Tb(III)	24
3.1.3. Modelling co-adsorption of Tb(III) and humic acid by means of a combined K_d approach (linear additive model)	25
3.2. Adsorption of Tb(III) onto clay materials in the presence of propionate and lactate	29
3.3. Radiotracer studies on the dynamics of adsorption equilibria for the system Tb(III) / humic acid / kaolinite	32
3.4. Elucidating time-dependent changes in the competition effect of Al(III) on Tb(III)-humate complexation	38
3.4.1. Evidence of stabilisation processes	38
3.4.2. Spectroscopic probing	40
3.5. Transport studies by means of positron emission tomography	45
3.5.1. Advection in homogenised clay samples	45
3.5.2. Advection in rock cores	51
3.5.3. Diffusion	55
4. Conclusions and outlook	66
5. References	69

List of abbreviations

CPU	central processing unit
DOC	dissolved organic carbon
EIT	electrical impedance tomography
FA	fulvic acid
FEM	finite element method
FWHM	full width at half maximum
HA	humic acid
HS	humic substance
LOR	line of response
LuYAP	cerium-doped lutetium yttrium aluminium perovskite
LYSO	cerium-doped lutetium yttrium orthosilicate
MRT	magnetic resonance tomography
MWCO	molecular weight cut-off
NIST	National Institute of Standards and Technology
OPA	Opalinus clay
OSEM	ordered subsets expectation maximisation
PE	polyethylene
PET	positron emission tomography
STIR	software for tomographic image reconstruction
VSG	visualisation science group
X- μ CT	X-ray computed microtomography

List of symbols

c	concentration
c	velocity of light
D	solid / liquid distribution ratio (mol / mol)
E	energy
I	intensity
K_d	solid / liquid distribution coefficient (mL / g)
m_e	rest mass of an electron
$t_{1/2}$	half-life
x	distance
β	stability constant
λ	wavelength
μ	linear attenuation coefficient
θ	scattering angle

1. Introduction

Predictive models on the migration of radionuclides in the event of release from underground disposal facilities are an important component of risk assessment studies in the selection process for a repository site. Because of their high radio- and chemotoxicity in conjunction with very long half-lives, actinides are in the focus of long-term safety analyses. In addition to the adsorption behaviour of the metal species, their interaction with colloidal components of the aqueous phase has been recognised to be of primary relevance. The capability of clays to adsorb cationic contaminants is outstanding, and it provides a barrier function as long as the net positive charge is not eliminated by negatively charged ligands. Besides formation of hydroxo / carbonate species at high pH values, interaction with aquatic humic substances as main constituents of colloidal DOC (dissolved organic carbon) can be decisive for the mobility of actinides or other contaminant metals [1-6]. Similarly, complex formation with organic components of natural clay is a potential mechanism to subvert the geochemical barrier.

It must be noted, however, that both mobilising and retarding effects are possible. Solid-liquid distribution of metals in the presence of humic substances is determined by the interaction of three elementary processes: (i) metal adsorption (ii) metal-humic complexation and (iii) adsorption of the humic substance. Extensive studies are undertaken to collect equilibrium data for these interactions, which are controlled by acid-base equilibria, redox processes and electrolyte composition. Since the dependencies are different for each interaction process, it is impractical to collect conditional data on metal adsorption for ternary systems (metal / humic substance / solid phase). In order to describe the influence of humic substances in transport models, data collected for binary systems need to be linked in an appropriate manner. As a major topic of this project, a combined K_d approach (linear additive model [7, 8]) was tested for suitability in reconstructing ternary systems on the basis of data determined for the binary subsystems. This conception has been incorporated in advanced transport codes where humic carriers are considered (for a literature review, see [9]). In its simplicity, it is, however, not unanimously accepted.

The adsorption studies presented in this report are focused on clay rock as a potential host formation for a final repository. According to an agreement within the joint project "Interaction and transport of actinides in natural clay rock considering humic substances and clay organic matter", natural clay material from the Opalinus clay formation (Mont Terri, Switzerland) was used as a reference sample. In addition, the clay minerals montmorillonite, illite and kaolinite were applied as adsorbent materials. The pH-dependence of metal adsorption was investigated in the absence and presence of humic acid as well as of propionic acid and lactic acid as representatives of low-molecular-weight organic matter occurring in natural clay rock.

The applicability of equilibrium approaches such as the linear additive model is affected by so-called kinetic effects. Complexation of higher-valent metals with humic substances has been found to be accompanied by slow processes leading to an increase in complex inertness [10-15]. In order to consider such phenomena in transport systems, a kinetically controlled availability model (KICAM) was developed [16, 17] and implemented in a coupled chemical transport code based on equilibrium and rate constants (K1-D) [18, 19]. In this model, a rapid complexation step is followed by a slow step, in which the metal changes from a fast-dissociating state to

a slowly-dissociating state. However, the chemical background of the different binding modes could not be elucidated so far. In this project, systematic studies were conducted to shed more light on the underlying processes, using laser fluorescence spectroscopy as a powerful technique to detect structural alterations on a molecular scale [20]. These investigations were focused on time-dependent phenomena in the competitive complexation with Al(III) as an important higher-valent electrolyte constituent in terrestrial waters.

In simple models on reactive solute transport, it is presumed that all involved interaction processes are in a steady local equilibrium under flow conditions. More sophisticated models also consider slow kinetics, but in any case, a dynamic exchange must be possible, i.e., the processes must be reversible. As regards adsorption of humic matter, it is unclear whether this requirement is actually met for these colloidal substances. In column experiments with geological materials, recoveries were found to be considerably lower than 100%. Besides filtration effects, irreversible adsorption may be a reason. As yet, the dynamics of adsorption equilibria has never been investigated for these substances. Tracer exchange experiments are uniquely suited for this purpose. By means of a homemade technique for ^{14}C -labelling of humic substances, it became possible to examine the reversibility of this process for the first time.

In addition to the possibility of distinction, an important advantage of radiotracers is the very low detection limit. Partitioning of actinides in DOC-containing systems has been found to be concentration-dependent [21] and therefore must be investigated at adequate concentration levels in order to generate reliable data. Conventional analytical methods are too insensitive for this purpose. Radioactive tracers provide analytical access to very dilute systems, in accordance with scenarios to be considered in the far-field of a nuclear waste repository. Besides ^{14}C -labelled humic and fulvic acids, [^{160}Tb]terbium(III) was used in this project, suitable as a short-lived tracer analogue of trivalent actinides such as Am(III), Cm(III) or Pu(III).

Another benefit of radiotracers is that they can be quantitatively localised in solid matrices. Migration of radionuclides fundamentally depends on the transport properties of the host rocks – including structural parameters from the nanoscale up to the field scale – and on interactions of dissolved or particle-bound radionuclides with the solid matrix. Since these structural influences are only present in the intact material, transport parameters of the real barrier material with its original structure need to be investigated to the same extent as geochemical interactions in suspensions. Experiments with compacted columns of ground material mainly reflect the effect of the reduced volume fraction of the fluid.

Transport properties of porous media have always been in the focus of petrophysics as well as chemical and reservoir engineering [22-24]. The porosity effect, which can be studied to some extent with compacted homogeneous material, is strongly modified by tortuosity effects, which reflect the topology, i.e., geometry distributions and network structure of the transport paths. The actual tortuosity effect depends on the nature of the processes (advection, molecular diffusion), state variables and driving forces, and thus is an effective, process-dependent tensor quantity. Presumably, it controls chemical reactions within the fluid volume and across the internal surface area, and thus the “effective reaction kinetics”. In tight materials like barrier rocks, transport limitation of chemical interactions plays a decisive role.

We apply positron emission tomography (PET) to investigate the behaviour and pathway distribution of radionuclides in order to reveal these transport effects in barrier material [25-27]. With the method of GeoPET, we benefit from the quantitative and spatially resolved detectability of radiotracers in solid matrices. The method has been adapted from applications in nuclear medicine. PET cameras are sensitive to positron-emitting radionuclides such as ^{18}F or ^{124}I . ^{18}F is the most frequently applied medical PET nuclide. Its half-life ($t_{1/2}$) of 110 min is, however, rather short. For geosciences, we also apply longer-lived nuclides, e.g., ^{58}Co ($t_{1/2} = 70.8$ d) or ^{22}Na ($t_{1/2} = 2.6$ y), which enables long-term diffusion experiments using other labelling methods, albeit at the expense of a higher noise level because these nuclides are non-pure positron emitters.

We fully customised a preclinical PET scanner to geoscientific applications. This GeoPET instrument is one-of-a-kind for the quantitative 4D (3D + time) visualisation of transport processes in geological matrices. Due to the higher density of geological material compared to body tissue, well-engineered correction procedures had to be developed and have been successfully implemented in the software. In this way, the physical limit of the spatial resolution (1.3 mm) has been finally reached. Compared to other solute visualisation techniques such as electrical impedance tomography (EIT) or nuclear magnetic resonance tomography (MRT), PET is about 10^{10} times more sensitive. Moreover, it is selective towards radiolabelled chemical species. This makes it an ideal method for the quantitative observation of labelled compounds in time and space. These data can be applied for model validation and parameterisation, improvement of process understanding as well as for the direct evaluation of process parameters (e.g., effective transport volume, flow path distribution and heterogeneity).

2. Experimental

2.1. Materials

2.1.1. Humic materials

Humic acid (HA) from Sigma-Aldrich (Germany), herein referred to as Aldrich HA, was purified by repeated precipitation and redissolution with 0.1 M HCl and 0.1 M NaOH / 0.01 M NaF, respectively, followed by dialysis and lyophilisation. An aquatic fulvic acid (FA) was isolated from surface water collected on the raised bog "Kleiner Kranichsee" (near Carlsfeld, Germany). Purification was carried out according to the recommendations of the International Humic Substances Society [28] (adsorption onto DAX-8 resin at pH 2, rinsing with 0.1 M HCl, elution with 0.1 M NaOH, evaporation, salt removal by cation exchange and dialysis, lyophilisation). Basic properties of the humic materials are specified in Table 1. Elemental analyses were performed with a Vario EL III (Elementar, Germany), acidities were determined by means of an automatic titrator TitroLine alpha (Schott, Germany) as described in Ref. [29].

Table 1. Elemental compositions, total acidities and contents of functional groups of humic materials used in the project.

		Aldrich HA	Bog water FA
C	(wt.-%)	50.5	49.2
H	(wt.-%)	4.8	4.4
N	(wt.-%)	3.8	4.5
Total acidity	(meq g ⁻¹)	6.0	8.1
Carboxylic groups	(meq g ⁻¹)	5.2	5.5
Phenolic hydroxyl groups*	(meq g ⁻¹)	0.8	2.6

* Taken as difference between total acidity and COOH content.

2.1.2. Radiochemicals

[¹⁶⁰Tb]Tb(III) ($t_{1/2} = 72.3$ d) was produced by neutron activation of natural Tb(III) (1 mg mL⁻¹, as nitrate) at the TRIGA Mark II reactor of the University of Mainz. 40 h of irradiation at a neutron flux of 7×10^{11} n cm⁻² s⁻¹ yielded a specific activity of 2 MBq mg⁻¹. After transformation into a perchlorate system by evaporating with concentrated HClO₄, a stock solution in 0.1 M NaClO₄ was prepared. [¹²⁴I]NaI ($t_{1/2} = 4.1$ d) was purchased from Eckert & Ziegler (Germany), [⁵⁸Co]CoCl₂ ($t_{1/2} = 70.8$ d) from Polatom (Poland). N.c.a. [¹⁸F]KF ($t_{1/2} = 1.8$ h) was kindly provided by the University of Leipzig, clinic and polyclinic for Nuclear Medicine. [⁸⁶Y]YCl₃ ($t_{1/2} = 14.7$ h) was produced by HZDR. [1-¹⁴C]propionate and [1-¹⁴C]L-lactate (specific activity: 2 GBq mmol⁻¹) were supplied as sodium salts by American Labelled Chemicals Inc. (US).

¹⁴C-labelled humic substances were prepared by an azo-coupling reaction [30]. The reaction scheme is shown in Fig. 1. For preparing the reactive benzenediazonium ion, ~ 6 MBq [¹⁴C]aniline hydrochloride (Biotrend, Germany) were added to 400 µL of a

solution of 0.1 M NaNO₂ in 1 M HCl, placed in an ice bath. 50 µL of this mixture were then given to 1000 µL of a solution of 0.5 g L⁻¹ of humic or fulvic acid in borate buffer (also cooled to 0°C), together with 80 µL of 0.1 M NaOH to maintain the pH value in a range between 8 and 9. This mixture was allowed to react in the ice bath for 30 min.

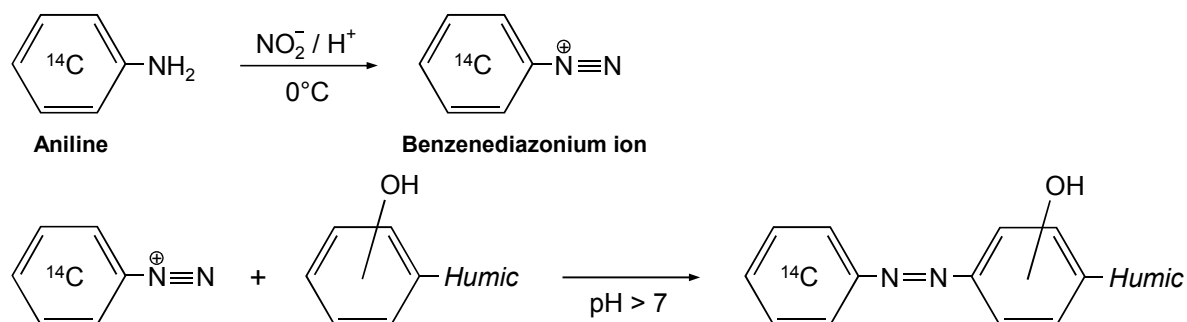


Figure 1. Reaction scheme for labelling humic acid with ¹⁴C by azo coupling with [¹⁴C]aniline.

For PET studies, humic acid was labelled with ¹²⁴I by the Iodogen method [31]. Halogenation is achieved by electrophilic substitution at activated positions within aromatic structures of humic molecules after oxidation of [¹²⁴I]I⁻ by Iodogen (1,3,4,6-tetrachloro-3a,6a-diphenylglycouril). The heterogeneous reaction was performed in glass vials with 150 µg Iodogen coating (added in 200 µL chloroform). A solution of [¹²⁴I]NaI (~ 100 MBq) and HA in borate buffer (pH 8) was prepared, and portions of 500 µL were dispensed into several vials containing Iodogen, followed by permanent shaking for 10 min.

For separating from non-reacted radioactive material, humic acid was precipitated by acidification to pH < 1 with concentrated HClO₄. After centrifugation (20 min at 5000 rpm), the supernatant was removed with a pipette, and the precipitate was redissolved in 10⁻² M NaOH. This procedure was repeated (8-10 times) until the activity in the supernatant was negligible. Finally, the precipitate was dissolved in 0.1 M NaClO₄ / 10⁻³ M NaOH. Fulvic acid (which cannot be precipitated) was purified by ultrafiltration, using Microsep centrifuge filters (Pall, US) with a MWCO of 1 kDa. The retentate was rinsed ~ 10 times with 1 mL 0.1 M NaClO₄ until the activity in the filtrate was negligible (60 min centrifugation at 7000 rpm for each filtration step). Specific activities were about 1 MBq mg⁻¹ and 500 MBq mg⁻¹ for ¹⁴C- and ¹²⁴I-labelled humic material, respectively.

2.1.3. Clay materials

Opalinus clay samples (BHE-24/1) from the Mont Terri rock laboratory (Switzerland) were provided the German Federal Institute for Geosciences and Natural Resources (BGR). The clay minerals kaolinite (KGa-1b), illite (IMt-1) and Na-montmorillonite (SWy-2) were standard materials obtained from the Source Clays Repository of the Clay Minerals Society of America. Some characteristics are given in Table 2. All samples except for kaolinite were ground. Illite was suspended in water to remove coarse particles.

Table 2. Characteristics of the clay materials used in the project.

	Kaolinite KGa-1b	Illite IMt-1	Montmorill. SWy-2	OPA clay BHE-24/1
BET surface area (m ² g ⁻¹)	14 [32]	39 [35]	29 [37]	41 [39]
Cation exch. capacity (meq g ⁻¹)	0.03 [33]	0.08 [35]	0.87 [37]	0.10 [39]
Point of zero charge (pH)	5.5 [34]	3.5 [36]	4.2 [38]	n.a.

n.a.: not applicable.

2.2. Methods

2.2.1. General remarks, analytical equipment

All experiments were conducted under ambient conditions (atmospheric CO₂ pressure, room temperature where not otherwise stated). Water was purified with an SG Ultra Clear system. Adjustment of pH values was accomplished by adding diluted HClO₄ or NaOH, using a Sentix 41 combination electrode (WTW, Germany) for measurement. Usage of buffer systems was avoided. All batch experiments were performed with 0.1 M NaClO₄ as a background electrolyte, using PE vials.

A 1480 Wallac WIZARD 3" gamma counter (Perkin Elmer, US) was used for measurements of ¹⁶⁰Tb activities. All samples of a test series were made up to equal volumes to ensure a uniform measuring geometry. ¹⁴C determinations were carried out with a Tri-Carb 3110 TR Liquid Scintillation Analyser (Perkin Elmer, US). Aliquots of 1 mL were mixed with 10 mL Ultima Gold scintillation cocktail (Perkin Elmer, US). The results were corrected for colour quenching caused by humic material.

UV-Vis spectrometry was conducted by means of a Lambda 45 spectrophotometer (Perkin Elmer, US). Elemental analyses by ICP-OES were performed by means of a Spectroflame P/M instrument (Spectro, Germany).

2.2.2. Quantitative determination of metal-humate complexation

Anion exchange method. Following a study by Hiraide et al. [40], the anion exchange resin Sephadex DEAE A-25 (Sigma-Aldrich) was used as a separating agent. Prior to use, it was washed with methanol, rinsed with 0.1 M NaClO₄ and kept therein after pH adjustment. Metal / HA systems were prepared with pH-adjusted stock solutions. For separating the humic-bound metal fraction from the free metal fraction, the exchange resin was added as a slurry of ~ 300 mg to 4 mL solutions. Humic material, including bound metals, is quantitatively adsorbed. After shaking for 1 min and sedimentation, an aliquot of the supernatant was taken, and the decrease in metal concentration relative to the initial concentration was measured. Corrected for the water content of the slurry, this depletion is equal to the concentration of humic-bound metal. For time-dependent studies on the competition effect of Al(III), solutions of Al(III) and HA were mixed and left to stand in the dark for different periods of time (up to 6 months) before Tb(III) was introduced to the system. The exchange resin was then added after a reaction time of 2 - 5 min. Preliminary stopped-flow experiments based on fluorescence quenching had proven that the process of Tb(III)-humate complexation is accomplished within few seconds (Fig. 2).

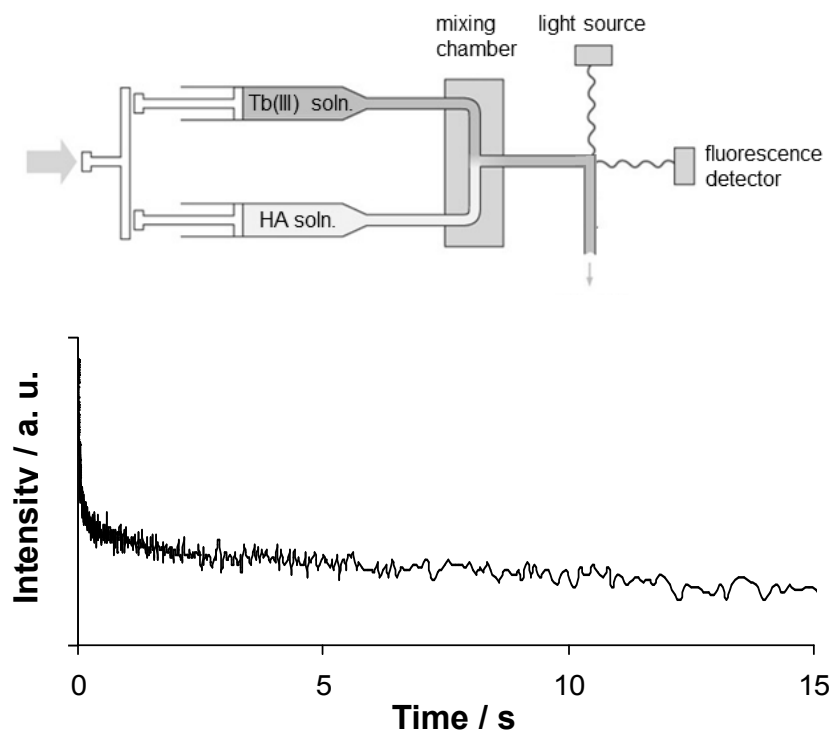


Figure 2. Stopped-flow experiments for monitoring the process of Tb(III)-humate complexation as a function of time, based on the quenching of fluorescence light emitted by HA (5 mg L⁻¹ HA, 10 μM Tb, 0.1 M NaClO₄, pH 4.0, λ_{exc} = 325 nm, 380 nm < λ_{em} < 580 nm).

Cation exchange method. Humic-bound Tb fractions were also determined on the basis of a metal exchange equilibrium between HA and a cation exchange resin, Bio-Rad AG 50W-X2. Humic acid is not adsorbed in this case. In order to avoid changes in pH, the cation exchanger was converted into its Na⁺ form by treating with 1 M NaOH. For equilibration, 10 mL of pH-adjusted solutions of Tb(III) or Tb(III) / HA in 0.1 M NaClO₄ were shaken with 10 mg of exchange resin. After 48 h, an aliquot was taken for analysis. The concentration of humic-bound metal c_M^{HA} was calculated from the relationship

$$c_M^{HA} = c_M^{total} \left(1 - \frac{D}{D_0} \right) \quad (1)$$

with D and D_0 denoting the solid-liquid distribution ratios of the metal (moles adsorbed / moles in solution) in the presence and absence of HA, respectively [41].

2.2.3. Studies on adsorption / desorption

For pre-conditioning to a series of pH values, stock suspensions of montmorillonite, illite or Opalinus clay in 0.1 M NaClO₄ were prepared and weighed. Dispersing was facilitated by sonication. The pH was then adjusted by adding HClO₄ or NaOH until the buffering capacities of the solids were exhausted (20 - 30 readjustments within a period of several weeks). When the pH values were stable, another weighing was

carried out, and an appropriate amount of solution was removed to attain a final solid-liquid ratio of 5 g L^{-1} , allowing for the volumes of Tb(III) / HA / propionate / lactate solutions to be added. The pH of kaolinite suspensions (used in the studies described in Section 3.3.) was left unchanged at 4.7. While stirring, the suspensions were then dispensed into 5 mL centrifuge tubes (PP), and the solutes were introduced (small amounts of near-neutral solutions), giving a total volume of 4 mL. After rotating end-over-end at 10 rpm for different time periods, the systems were centrifuged at 7000 rpm for 5 min, an aliquot of the supernatant was sampled, and the depletion was determined. In desorption studies, 3 mL of the supernatant were replaced by 3 mL of 0.1 M NaClO₄ solution, and the diluted systems were again rotated for different time periods. After centrifugation, aliquots were analysed for changes in concentration. Wall adsorption was found to be negligible for all solutes. Details on tracer exchange experiments are given in Section 3.3.

2.2.4. Laser fluorescence spectroscopy

Spectroscopic probing studies on possible structural backgrounds of kinetic effects in metal-humate complexation were carried out in cooperation with the university of Potsdam. Steady-state fluorescence spectra were recorded by means of a FluoroMax-3P spectrofluorometer (Jobin Yvon, US). For time-resolved laser-induced fluorescence spectroscopy (TRLFS), a pulsed Nd-YAG laser (Spectra-Physics, US) was used in combination with an optical parametric oscillator (GWU Lasertechnik, Germany). The fluorescence emission was detected by an iCCD camera coupled to a spectrograph (Andor Technology, UK). To record a full fluorescence decay of Tb(III) as a spectroscopic probe, 120 spectra (in the range of $450 \text{ nm} < \lambda_{\text{em}} < 700 \text{ nm}$) were acquired in steps of $15 \mu\text{s}$ (100 accumulations each in $50 \mu\text{s}$ time slots) with an initial delay of $1 \mu\text{s}$ to exclude any contribution of HA fluorescence. Decay curves were obtained by integrating the intensities within the range of the principal spectral band ($^5\text{D}_4 \rightarrow ^7\text{F}_5$ transition, $533 \text{ nm} < \lambda_{\text{em}} < 562 \text{ nm}$). Emission spectra for Eu(III) as a probe were recorded with an initial delay of $10 \mu\text{s}$ in a decay time frame of 5 ms (10^4 accumulations). The fluorescence intensities were corrected for drifts in the laser light intensity and in the spectral background. Further details are given in the results chapter. Test series with Al(III) / HA systems of different ages were prepared as described in Section 2.2.2. Acquisition of spectra was started 2 min after addition of Tb(III) or Eu(III).

2.2.5. Positron emission tomography (PET)

Principle. The localisation of positron-emitting radionuclides is based on the coincident detection of annihilation photons that are emitted pairwise in antiparallel direction when a positron hits an electron after deceleration to the thermal state. With an annular arrangement of scintillation detectors, the source of radiation can be assigned to the connecting line. As this line of response (LOR) is randomly oriented for every annihilation event, the radionuclide can be exactly localised at the intersection point of a multitude of LORs. From the frequency of detected coincidences, the radiotracer activity in a volume element (voxel) can be quantitatively determined.

This rather simple principle of quantitative image generation is complicated by a number of additional physical effects which – in the case of biomedical PET applications – are regarded as second-order corrections. These are more significant in the case of dense material, and interactions between matter and radiation have to be considered in more detail. The effects are:

- (i) slowing down of the positrons to the thermal state; the slow-down length decreases with increasing material density (cross section) [42],
- (ii) absorption of single annihilation photons according to Lambert-Beer's law

$$I(x) = I_0 \exp(-\mu x) \quad (2)$$

where I is the intensity, x is the distance, and μ is the linear attenuation coefficient, which can be derived from the mass absorption coefficients [43],

- (iii) scattering of photons, predominantly by Compton scattering, which causes an energy loss of photons of the initial energy E_0 to E_f

$$E_f = \frac{E_0}{1 + \alpha_E (1 - \cos\theta)} \quad (3)$$

with

$$\alpha_E = \frac{E_0}{m_e c^2} \quad (4)$$

where θ is the scattering angle, m_e is the rest mass of an electron, and c is the velocity of light. In usual PET applications, small angle scattering with angles $< 30^\circ$ is prevailing. This could be confirmed with our own Monte Carlo simulations for dense material as well [44].

Equipment. In the application period for this project, a human-medical PET scanner at the clinic and polyclinic of Nuclear Medicine of the University of Leipzig and an inhouse-developed PET scanner with a higher resolution, yet lower efficiency, were applied, predominantly for testing the feasibility of PET studies on transport processes in geomaterials. Successful demonstrational experiments enabled the acquisition of a commercial high-resolution PET scanner “ClearPET” (Raytest, Germany), which was not expected at the time of application and which allowed us to expand our transport studies considerably.

ClearPET [45-47], which was actually designed for 3D radiotracer studies with small animals, consists of 20 detector modules, each with 256 double-layered scintillation crystals on 4 position-dependent photomultiplier tubes. In a first phase, until June 2008, only 8 cassettes were installed, entailing a lower efficiency and a lower signal-to-noise ratio. The crystals are LYSO-LuYAP-phoswich combinations, size $2 \times 2 \times 10$ mm. This allows directional filtering of the incident photons and thus precise localisation of the decay events. The complete gantry of about 2 m in diameter is rotating around the specimen, both increasing the spatial covering of detector positions and equalising differences in the detection probability of the individual channels. The diameter of the field of view is adjustable between 70 mm and

144 mm, with a maximum length of 110 mm. The activity range is in the order of 30 dB, with a maximum activity around 100 MBq. The sensitivity of the scanner is better than 10 kBq per voxel, only limited by the detection probability and the natural background radiation. The currently achievable spatial resolution of about 1 mm is due to the free path of the emitted positrons before annihilation. One disadvantage of the modular construction of the scanner is an inhomogeneous sensitivity distribution within the field of view, which is caused by the gaps between the individual detector crystals. All events (“singles”) are recorded on 5 CPUs in parallel as partial listmode files. These are later combined by coincidence sorting, with simultaneous random detection, to yield listmode files of all coincident and random events. These files of “prompts” and “randoms”, with sizes of 1-10 GBytes, are archived as raw data.

Software. The tomographic reconstruction scheme is based on the open-source STIR library (version 1.4) [48, 49], complemented by some proprietary software. The final reconstruction product is a time series of data sets (interfile format) of quantitative tracer concentrations in 3D with voxel dimensions of $1.15 \times 1.15 \times 1.15 \text{ mm}^3$. The STIR image reconstruction operates in the space of projections, i.e., the bin-wise presentation of the LORs as a function of segment (inclination of the projection plane), view (azimuth of the LOR), axial coordinate and tangential coordinate. The original reconstruction consists of 7 steps:

- (1) binning (computing bin-wise projections from the listmode files of prompts and randoms)
- (2) random correction (bin-wise subtraction)
- (3) deadtime correction (correction of the scanner response curve)
- (4) absorption correction by means of a transmission scan
- (5) scatter correction by subtracting a nonlinear fit of the counts outside the field of view (resp. radiation source) to a Gauss function
- (6) iterative image reconstruction and normalisation with the STIR OSEM algorithm
- (7) image calibration (application of the scanner efficiency factor)

Most of these steps had to be adapted to the conditions of geological specimens with their considerably higher mass attenuation coefficient and scatter fractions compared to tissue. These adaptations refer to the following details:

To (2): It was found in the course of the experiments that the random correction was deficient in the presence of high background radiation, which is caused by background gradients due to scattered radiation from sources within or outside the field of view. This is due to the weakly occupied projection arrays, which is a common characteristic of 3D-PET projection data. The algorithm of random detection by delayed coincidence sorting is prone to bin-wise prompt-random missing of proximate bins. Thus, in the presence of high background radiation, a high amount of bins with negative values was found when the original random correction was applied. These negative bins were not considered subsequently. This effect produced image artifacts and quantification errors. It was repaired by some spatial balancing of the negative bins over the nearest neighbors, applying the R-package “SPATSTAT” (open-source software for spatial statistics) [50].

To (4): It was not possible to apply transmission scans with line sources that were positioned outside the field of view because the strong attenuation of the material caused low count rates on the opposite sides, which were hardly above the

background. However, because the specimens have simple geometries and a well-defined composition, the attenuation image could be constructed with the help of mass attenuation coefficients from the NIST XCOM (photon cross sections database) [51]. The correction factor for each bin is calculated from the line integral over the attenuation coefficient distribution for each LOR, which is the projection of the attenuation image. It must be noticed that this correction is crucial for providing consistent input data for the reconstruction and thus has to be applied to the projections.

To (5): The scatter correction, based on an extrapolation of weakly occupied points of the projection outside the field of view into it, turned out to increase the noise level, rather than to improve image quality. Therefore, we skipped the scatter correction so far. However, scatter causes significant blurring and image artifacts. We could characterise and quantify the extent and origin of scatter by Monte Carlo simulations of a number of PET experiments with fixed radiation sources using the software OpenGATE [52]. The simulations show that scatter fractions of up to 70% have to be considered, mainly depending on the density of the material. Both the new version of STIR (2.1) and the Monte Carlo simulations provide potential correction methods which will be applied in future.

To (6): The OSEM algorithm appears to be sensitive to obscure coincidences, which may be due to erroneous corrections or scatter [53]. These obscure coincidences produce ring artifacts, which are related to the inhomogeneous sensitivity distribution, and they produce radial artifacts. Both effects can be distinguished in most tomograms. Such reconstruction artifacts could be eliminated or at least reduced by “physics-based” inversion algorithms. Prospectively, such algorithms could be developed by combining a physical model of the observed process (i.e., partial differential equations) with the Monte Carlo forward simulation of the PET measurements. However, this approach is hampered by the lack of computing resources up to now.

The inhomogeneous sensitivity distribution is another issue of the reconstruction procedure (normalisation). The sensitivity is determined by measuring a homogeneous source of radiation, filling the complete field of view (Fig. 3). The gaps between the detector blocks produce gaps in the projections and strong local variations near these gaps. The STIR OSMAPOS algorithm shows a marked influence of the normalisation on the final image, which is probably a deficiency of this algorithm. Therefore, other reconstruction algorithms and procedures for the normalisation will be tested and applied in future.

To (7): The normalisation, together with the errors of its measurements and image artifacts, enter into the image calibration. Thus, we usually skipped the original calibration procedure and applied image-derived calibrations, either based on the known total activity or on known point sources within the field of view.

The image files are in the Interfile format, an old-established image format for medical tomograms, consisting of a header file in text format and a binary file. The rudimentary information in these files was extended, and all corrections were applied to the binary data, including the radioactive decay correction.

Most manipulations of the images were conducted with the free statistical software environment “R” [54]. Image smoothing algorithms based on R-packages were added, such as mean and median filtering in the space domain and smoothing splines in the time domain. Also, fitting algorithms for parameter estimation were applied, such as “CXTFIT” [55]. Finally, the tomograms were converted to the format of the software “Avizo fire” (VSG) for 3D-t visualisation and image analysis. First steps were done to utilise the data sets for the calibration of calculations by the finite element method (FEM). Parameters were even directly derived by optimising the FEM parameterisation.

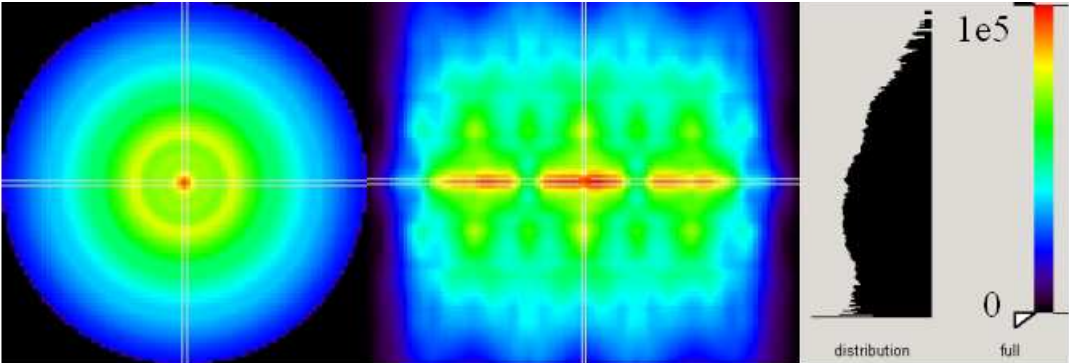


Figure 3. Normalisation image of ClearPET (backprojection image of a homogeneous activity distribution throughout the complete field of view).

Samples and their preparation. Homogeneous artificial clay samples as well as drill cores from intact crystalline and mud rocks have been investigated. The artificial samples were prepared from suspensions of kaolinite (Kao) and Opalinus clay (OPA1) in water and synthetic Opalinus clay pore water, respectively. These samples were compacted in a compression apparatus (Pero, Germany), shown in Fig. 4.

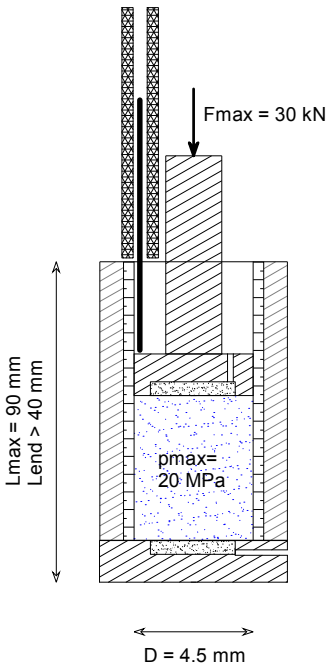


Figure 4. Schematic view of the compaction apparatus.

A highly viscous paste, prepared with the adequate pore water, was filled into a sample container (diameter 5 cm) with end plates of porous metal. Then, the sample was compacted at constant pressure on the mobile end plate, allowing drainage through the end plates. The compaction, recorded with a length transducer, was terminated after pore pressure equilibration (primary compaction), which is indicated by a significant decrease of the compaction rate when the secondary phase of structural particle rearrangement is reached after some days (depending on the material) (Fig. 5).

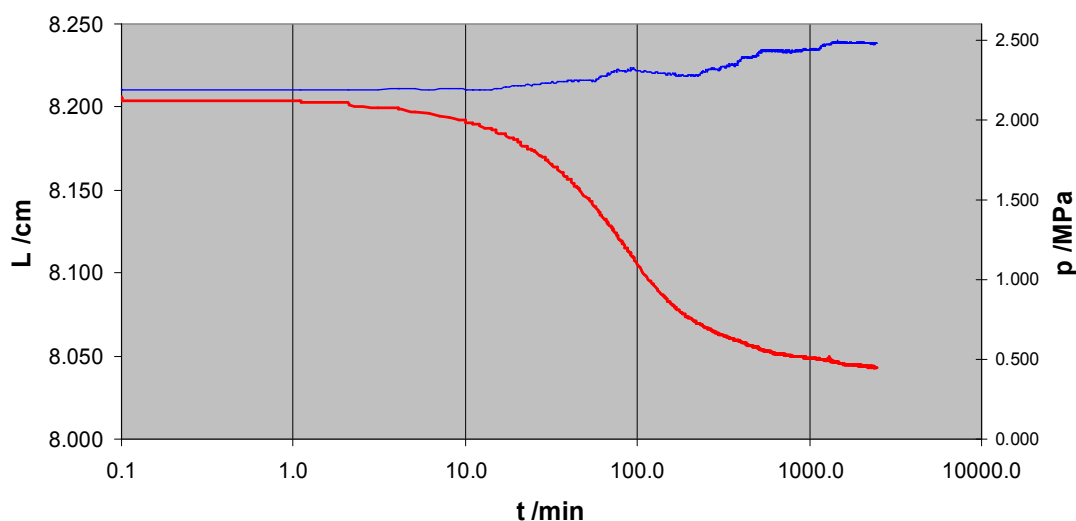


Figure 5. Compaction curve of the kaolinite sample (red: extension, blue: pressure).

The compacted sample was then transferred into a flow-through cell with end plates of sintered glass. The experimental conditions are shown in Table 3. The final porosities depend on a variety of conditions like particle size and added fluid volume.

Table 3. Experimental conditions for the preparation of compacted clay samples.

	Kao	OPA1
Material	kaolinite paste	Opalinus clay powder
Fluid	water	synthetic OPA pore water with 0.01 M KI
Pressure (MPa)	2.5	0.5
Compaction time (h)	120	50
Final porosity	0.63	0.41

Intact drill cores of consolidated material were cast into resin. The end plates with the fluid ports were made of plastic and were attached to the samples with a minimum gap (~ 0.1 mm) in order to reduce the dead volume. Otherwise, the radiation originating from the tracer accumulation in the dead volume would deteriorate the image quality. It could be shown that the shape of the tracer pulse is already smoothed strongly by passing the input volume.

Advection experiments. For advection-dispersion experiments, a tracer pulse was pumped through the sample (Fig. 6). Flow rate, driving pressure and tracer volume were chosen according to the properties of the sample. Before and after tracer

injection, the sample was conditioned with carrier solution in order to impede selective sorption of the tracer. During injection, repeated PET scans of the sample were recorded with a frame rate and duration according to the propagation time of the labelled compound and to the decay time of the radionuclide.

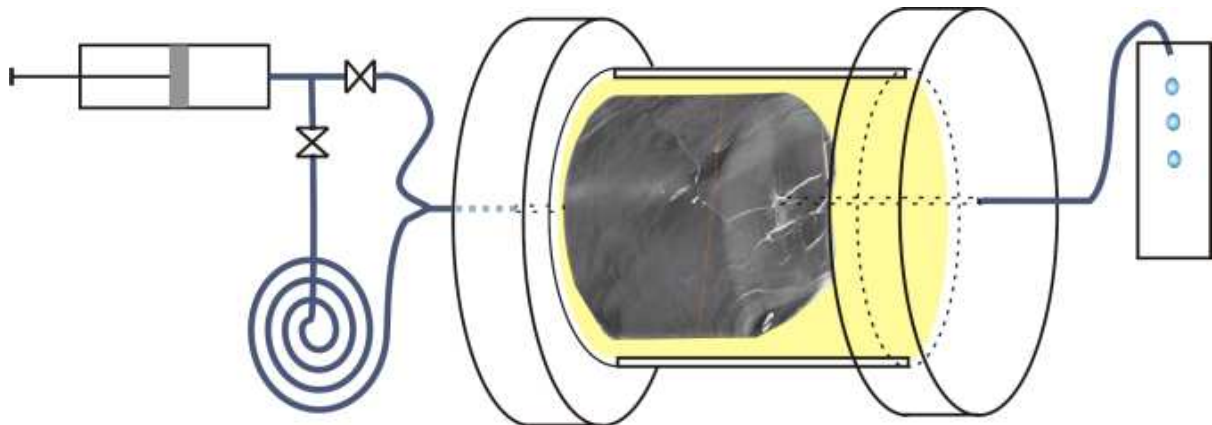


Figure 6. Typical setup of an advection experiment. In a first stage, the sample is preconditioned by injecting carrier solution. Then, the compound (labelled with an appropriate radionuclide) is injected, followed again by carrier solution.

Diffusion experiments. Diffusion experiments were conducted by introducing tracer solutions to an axial central blind hole (diameter 5 mm) in the sample which was completely cast into resin. The tracer-filled hole was closed with a screw. Then, repeated scans were taken over periods of up to 3 weeks with ^{124}I as a tracer. Prospectively, diffusion times of about 1 year will be feasible using ^{58}Co , or even 5 years using ^{22}Na .

It has to be noticed that unconventional PET nuclides like ^{124}I or ^{58}Co emit strong γ -radiation in the spectral range near 511 keV. The impact of these interferences has been studied, together with the scattering characteristics, by Monte Carlo simulations of all nuclear physical effects that are present, using the OpenGATE code (Fig. 7). First results from these simulations, which also served to quantify the strong effects of Compton scattering, show a significant decrease in the signal-to-noise ratio of the images compared to ^{18}F [44]. The results of the simulations will be applied in error estimations and in determinations of detection limits.

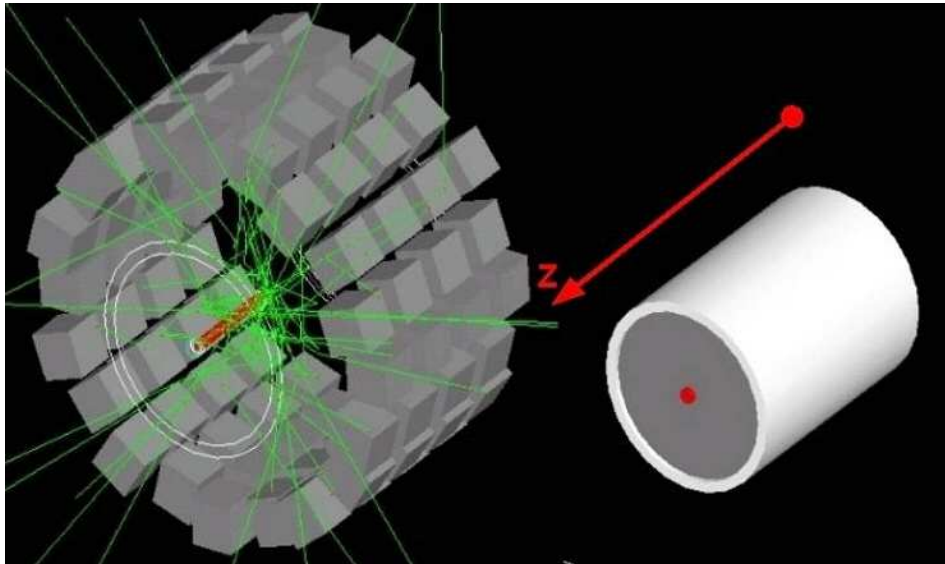


Figure 7. Definition of scanner configuration (left) and phantom (i.e., a model of source and sample, right), together with exemplary ray paths of the emitted photons (green lines) as simulated with OpenGATE. The locations of the detected events are stored in a listmode file, together with their history (e.g., origin, number of scatter events, scatter angle, energy loss).

3. Results and discussion

3.1. Co-adsorption of Tb(III) and humic acid onto clay materials as a function of pH

3.1.1. Tb(III) adsorption in the absence and presence of humic acid

In Figs. 8a - 8c, adsorption of Tb(III) onto illite, montmorillonite and Opalinus clay in the absence and presence of Aldrich humic acid is shown as a function of pH. The initial concentrations of Tb(III) and HA were fixed at 10^{-7} M and 5 g L^{-1} , respectively. The data are represented as solid-liquid distribution coefficients K_d . With increasing pH (limited to values of up to 6.4 due to the onset of Tb hydroxide precipitation), $\log K_d$ values increase from about 2 to 4 for illite and Opalinus clay, and from 3 to 4 for montmorillonite. Metal adsorption is promoted on raising the pH since more binding sites are provided by deprotonation of surface hydroxyl groups. At the highest pH, adsorption amounts to nearly 99%.

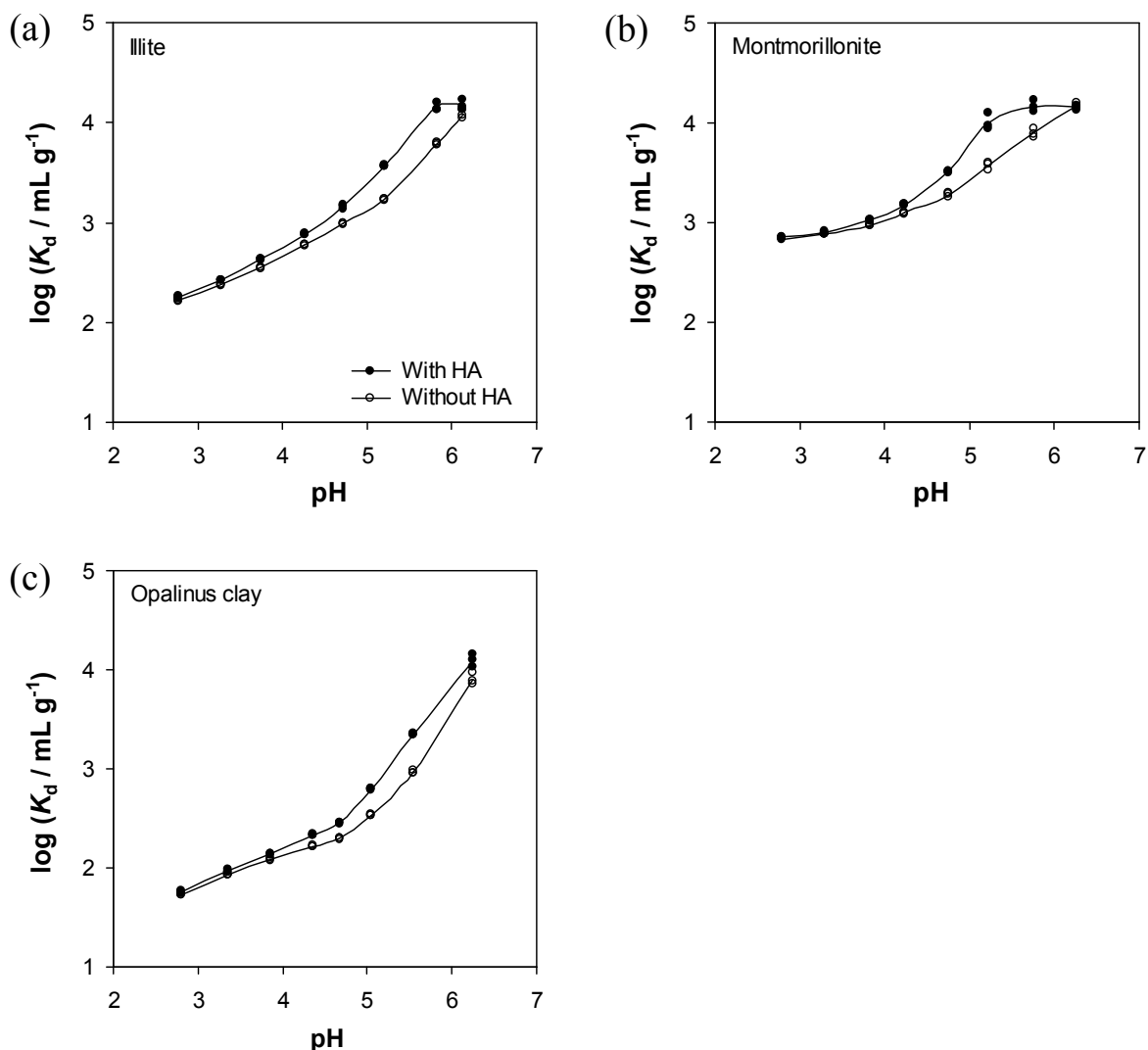


Figure 8. Adsorption of Tb(III) (10^{-7} M) onto clay materials (5 g L^{-1}) in 0.1 M NaClO_4 , in the absence and presence of humic acid (5 mg L^{-1}), as a function of pH.

For all clay materials under study, adsorption is increased in the presence of humic acid throughout the pH range investigated. Obviously, binding is mediated by HA in that additional Tb is co-adsorbed as a humate complex. An important conclusion that may be drawn is that desorption of metals from clay barriers, occurring in consequence of acidification processes, will be counteracted in the presence of humic matter, i.e., the situation will not deteriorate by humic-bound transport.

3.1.2. Adsorption of humic acid and humate complexation of Tb(III)

Fig. 9a shows the adsorption behaviour of humic acid on the clay materials. Adsorbed amounts are lowest for Opalinus clay, which also applies to the adsorption of Tb (Fig. 8c). This is explained by the content of non-argillaceous constituents such as quartz, calcite and pyrite. Generally, adsorption of HA increases on acidification since the electrostatic repulsion by negative charges on both HA and solid surface is reduced by protonation of acidic centres. The occurrence of a maximum in the case of illite is probably due to mineral dissolution.

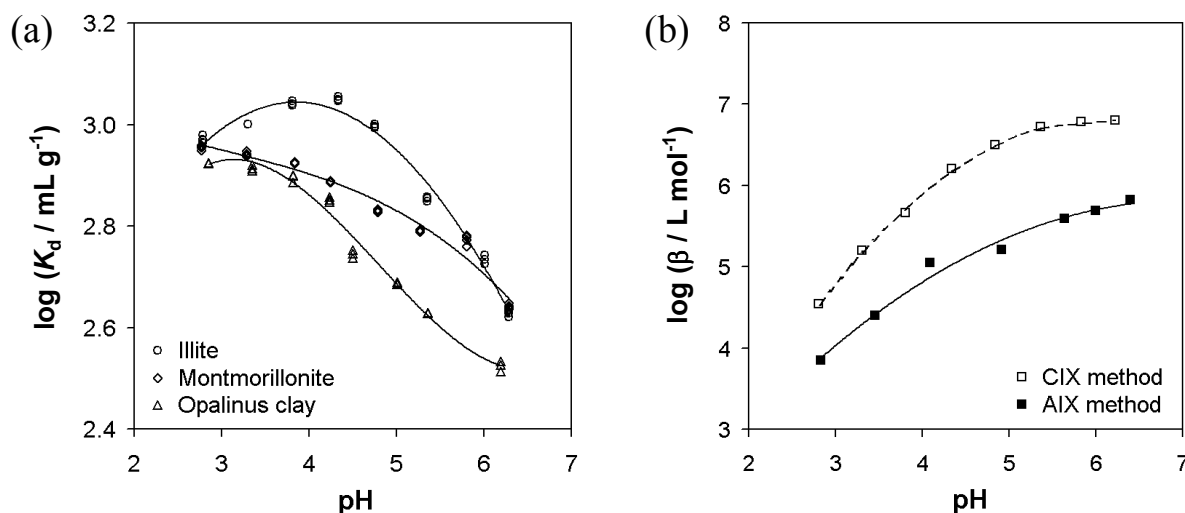


Figure 9. Adsorption of humic acid onto clay materials (a) and complexation of Tb(III) with humic acid (b) in 0.1 M NaClO₄ as a function of pH (CIX: cation exchange, AIX: anion exchange, concentrations as indicated in Fig. 8).

The pH dependence of Tb-humate complexation is shown in Fig. 9b. These data are given as conditional stability constants β , calculated according to Eq. (5) for a hypothetical 1:1 stoichiometry.

$$\beta = \frac{c_M^{\text{HA}}}{c_M c_L} \quad (5)$$

In this equation, c_L is the equilibrium concentration of free ligands, here simplistically defined by Eq. (6), where c_{HA} is the concentration of humic acid, and PEC is its proton exchange capacity per unit mass. The value of 5.6 meq g⁻¹ was taken from Ref. [56].

$$c_L = c_{HA}PEC - c_M^{HA} \quad (6)$$

The results from cation exchange experiments differ considerably from those obtained with the anion exchange method. This may be due to the fact that binding of HA to the anion exchange resin is a competitive reaction in respect of metal binding since the humic ligands are involved in the fixation. Thus, part of the bound metal fraction might be displaced in the separation process, which would explain the lower $\log \beta$ values. Errors in the cation exchange data may arise from adsorption of HA to the inner walls of the PE vials or even to the resin, but this has been checked.

From both data sets in Fig. 9b, it is visible that complexation is suppressed with decreasing pH because the ligands are blocked by protonation. Accordingly, the influence of humic acid on the adsorption of Tb(III) onto the clay materials diminishes at low pH, reflected by the convergence of the curves in Figs. 8a - 8c. Towards alkaline pH, a convergence is observed as well. Most likely, this can be explained by the decrease in adsorption of HA. Since Tb-humate complexation takes place in the aqueous phase to an increasing extent, the humic acid loses its mediating function in respect of Tb adsorption, and a competitive situation arises instead.

3.1.3. Modelling co-adsorption of Tb(III) and humic acid by means of a combined K_d approach (linear additive model)

With the apparent interrelations described above, it should be possible to predict the pH-dependent effect of HA quantitatively on the basis of the data for Tb adsorption in the absence of HA, Tb-humate complexation and HA adsorption. According to the linear additive model [7, 8], these processes are considered as a system of interdependent equilibria. For simplicity, they are all represented by K_d values in the following equations, where Γ is the adsorbed amount per unit mass of solid, and c is the equilibrium concentration. The indices S and M-HA stand for solid phase and metal-humate complex, respectively.

$$K_d^{M/S} = \frac{\Gamma_M}{c_M} \quad (7)$$

$$K_d^{M/HA} = \frac{\Gamma_M^{HA}}{c_M} = \frac{c_M^{HA}}{c_M c_{HA}} \quad (8)$$

$$K_d^{HA/S} = \frac{\Gamma_{HA}}{c_{HA}} = \frac{\Gamma_{M-HA}}{c_{M-HA}} \quad (9)$$

Combining Eqs. (7) - (9) yields Eq. (10) for co-adsorption of metal and metal-humate complex:

$$K_d^{(M + M-HA)/S} = \frac{K_d^{M/S} + K_d^{HA/S} K_d^{M/HA} c_{HA}}{1 + K_d^{M/HA} c_{HA}} \quad (10)$$

To reconstruct the pH dependence of Tb adsorption in the presence of HA, the experimentally determined values of $K_d^{M/HA}$, $K_d^{HA/S}$ and c_{HA} as a function of pH were fitted by polynomials, and $K_d^{(M+M-HA)/S}$ was calculated for the measured $K_d^{M/S}$ / pH data using values obtained by interpolation. The results are shown in Figs. 10a - 10c.

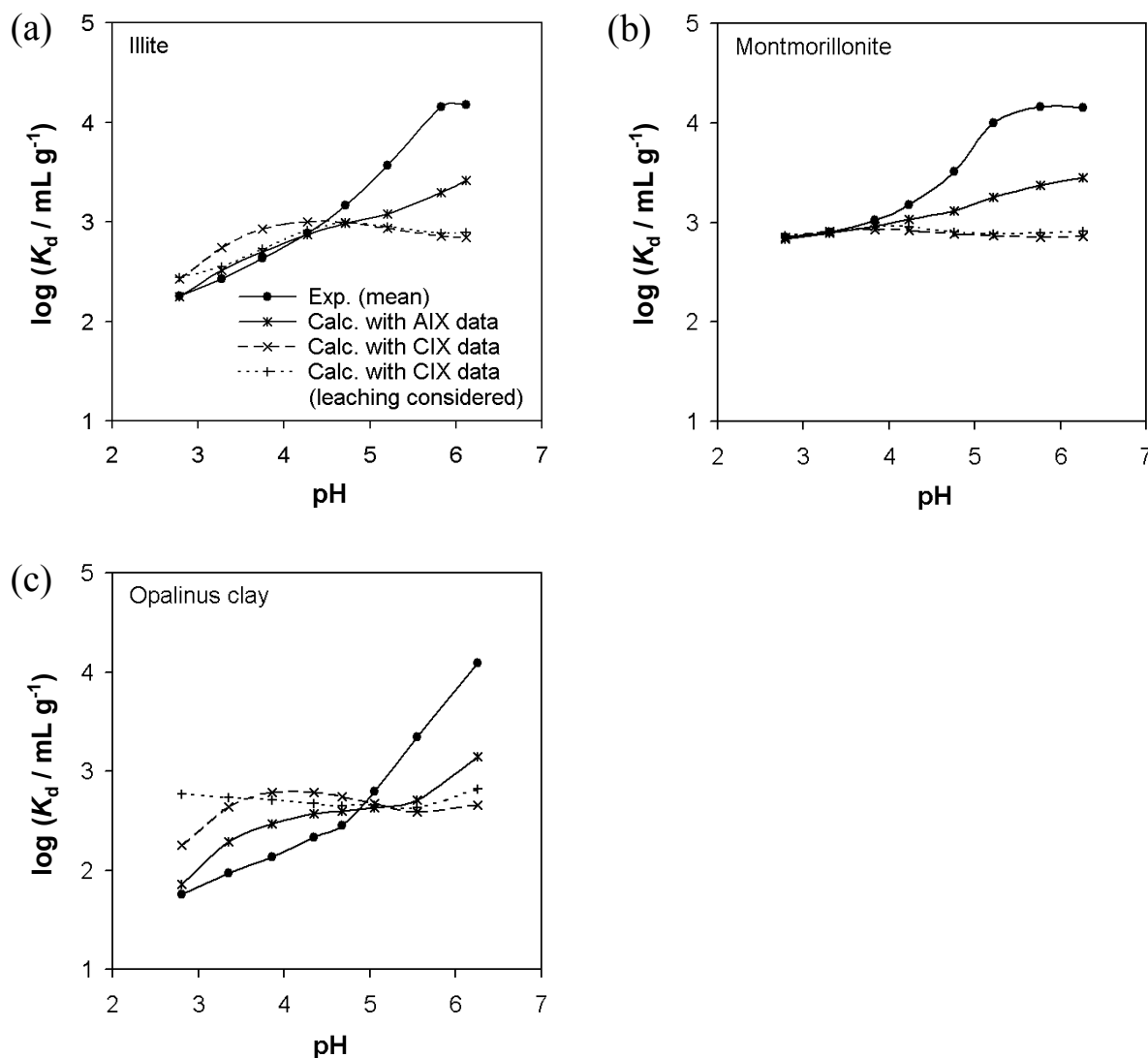


Figure 10. Adsorption of Tb(III) in ternary systems. Experimental data (solid dots) and calculated data based on the linear additive model.

Clearly, the linear additive model fails to reproduce the measured data, which applies to all clay materials investigated. Regarding experimental errors as a possible reason, the largest uncertainty is ascribed to the data for metal-humate complexation. Expectedly, there is a striking difference between the calculated results based on data from anion and cation exchange experiments, respectively, but neither of them approximates the experimental values. Leaching of metals from the clay materials by mineral dissolution could be a major source of error since, in the ternary systems, binding of Tb(III) to HA may be influenced by competitive effects, which are not accounted for if complexation data are determined for perchlorate

solutions only. Significant quantities of Ca, Mg, Al and Fe were detected in the supernatants of the adsorption systems. The highest concentrations were found for Opalinus Clay (Fig. 11).

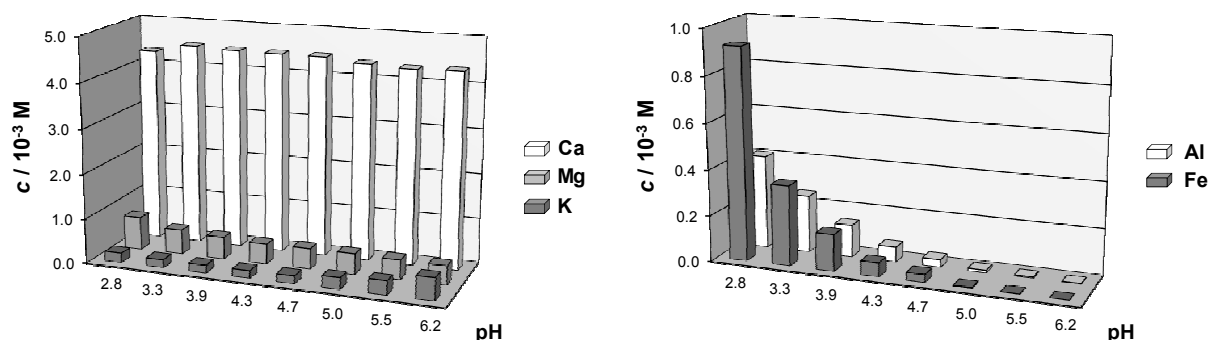


Figure 11. Metal concentrations in the supernatant solutions of the adsorption systems with Opalinus clay.

In particular, Ca is released due to calcite dissolution. Surprisingly, Ca concentrations were found to be independent of the pH. The expected increase on acidification was only observed for the trivalent metals Al and Fe. To investigate the competitive influence of all these metals, complexation studies were also conducted with the supernatant solutions, using the cation exchange method. In fact, Tb binding was found to be markedly reduced (data not shown). However, the implications on the model calculations turned out to be minor (see Fig. 10).

Erroneous data are also possible for HA adsorption. Radiolabelling of humic substances must not only meet the criterion of stability but also of non-selectivity to ensure that the detected tracers are representative of the humic molecules as a whole. Although this has been proven (cf. results in Section 3.3.), an element of uncertainty remains. However, enforcing the agreement between experimental and calculated values by adjusting HA adsorption as a fit parameter yields unrealistic trends beyond any reasonable limits of error.

Therefore, we conclude that the discrepancy is not attributable to experimental inaccuracies but to the conception of the model itself, specifically to the supposition that the individual processes are independent of each other. For instance, in Eq. (9), it is assumed that the adsorption of the M-HA complex is not different from the adsorption of HA. This cannot apply unrestrictedly since metal binding is comparable to protonation, and the influence of protonation on HA adsorption is evident from the pH dependence shown in Fig. 9a. In order to get an idea of the area of validity of Eq. (9), we investigated HA adsorption on montmorillonite as a function of metal concentration, using aluminium as an example of trivalent metals. As can be seen in Fig. 12, adsorption is increased on metal addition, but the effect is insignificant at concentrations below 10^{-5} M. Thus, it can be excluded that HA adsorption is affected by the presence of only 10^{-7} M Tb.

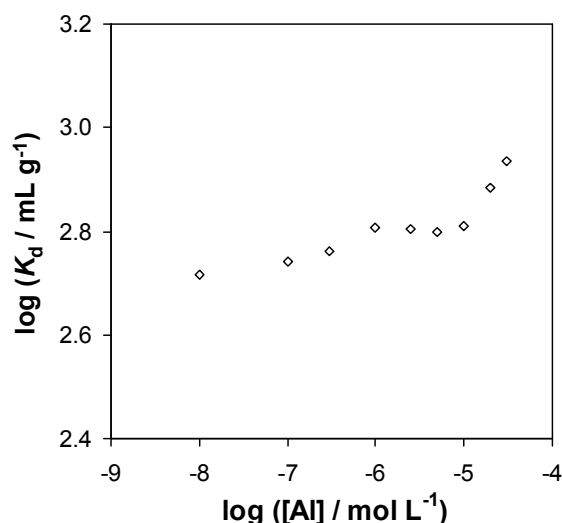


Figure 12. Adsorption of humic acid (5 mg L⁻¹) onto montmorillonite (5 g L⁻¹) in 0.1 M NaClO₄ (pH 6.0) in the presence of Al(III).

On the other side, direct adsorption of M will be impeded with increasing adsorption of M–HA. However, in consideration of the fact that the sorption capacity of humic material exceeds that of a mineral surface by orders of magnitude, a blocking effect should not be of major relevance to the performance of the model.

Another implicit assumption is that the stability of the M–HA complex in solution is equal to its stability in the adsorbed state. This is probably the weakest point of the model. First, it must be taken into consideration that complexation is potentially counteracted by adsorption, as may be inferred from the comparison between cation and anion exchange data in Fig. 9b. Furthermore, adsorption of humic substances, as multicomponent systems, is accompanied with some fractionation [57-59], and it has been reported that the capability of metal binding is not evenly distributed over molecular weight fractions [60-62]. If, for instance, fractions with high metal loads are preferably adsorbed, metal adsorption will be underestimated by the model as it operates with an averaged metal load, determined for the humic substance as a whole. For illite and montmorillonite, Tb adsorption is largely underestimated. For Opalinus clay, however, there is both underestimation and overestimation depending on the pH value, possibly as a consequence of the complexity of this material. A combined action of contrary effects is certainly conceivable.

3.2. Adsorption of Tb(III) onto clay materials in the presence of propionate and lactate

Propionic and lactic acid, besides formic and acetic acid, are the main components of low-molecular-weight organic matter present in natural clay rock. DOC quantities of 10 mg L^{-1} and 57 mg L^{-1} have been found in the pore waters of Opalinus clay and Callovo-Oxfordian clay, respectively [63]. In weakly acidic solutions, propionic and lactic acid are largely dissociated ($pK_a = 4.87$ and 3.86 , respectively). In this work package, we investigated the influence of these organic anions on Tb(III) adsorption onto the clay materials used in the studies with humic acid (Section 3.1.), covering the same range of pH values. In first experiments with Opalinus clay at constant pH, concentrations of propionate and lactate were varied in order to find the minimum amounts that cause a distinct effect (Fig. 13).

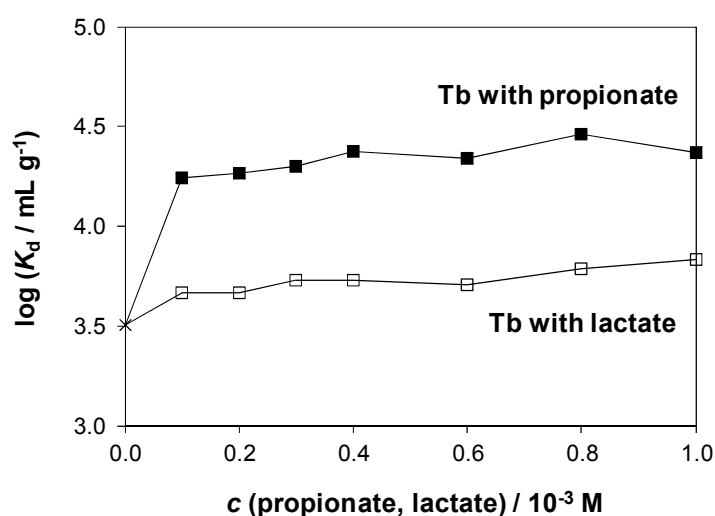


Figure 13. Adsorption of Tb(III) (10^{-7} M) onto Opalinus clay (1 g L^{-1}) in the presence of Na L-lactate or Na propionate, as a function of the concentration (0.1 M NaClO_4 , pH 6.0).

Obviously, the presence of propionate and lactate causes an increase in Tb(III) adsorption. This result is surprising, considering the fact that both the solid surface and the organic compounds are negatively charged. Given that both anions act as ligands that form complexes with Tb(III) – otherwise they would not cause any effect – only a decrease in adsorption is conceivable since the positive net charge of the metal would be reduced by all means.

Adsorption studies at variable pH values, using defined clay minerals in addition, should give more information that allows an interpretation of the unexpected behaviour. The concentrations of lactate and propionate were fixed at $2 \times 10^{-4} \text{ M}$ ($\sim 20 \text{ mg L}^{-1}$, corresponding to the DOC concentration found for Opalinus clay pore water). The results are shown in Fig. 14.

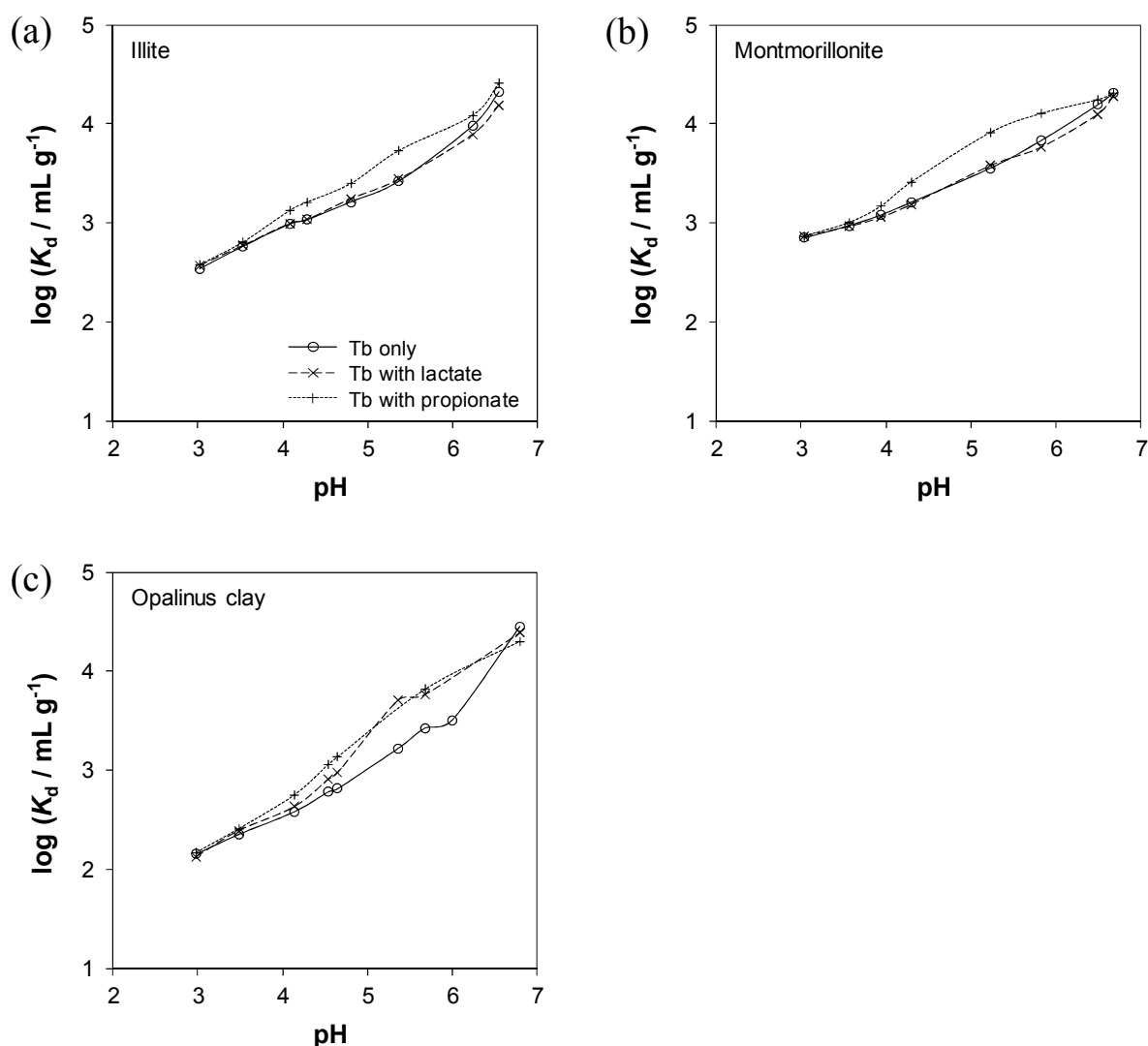


Figure 14. Adsorption of Tb(III) (10^{-7} M) onto clay materials (1 g L^{-1}) in 0.1 M NaClO_4 , in the absence and presence of Na L-lactate or Na propionate (2×10^{-4} M), as a function of pH.

For Opalinus clay, the increase in Tb(III) adsorption in the presence of both organic compounds was also found for more acidic solutions. The influence diminishes at low pH, which may be due to the increasing protonation of the acids. Similar results were obtained for illite and montmorillonite as far as the effect of propionate is concerned. In contrast, the effect of lactate was found to be negligible. Only in near-neutral solutions, a very minor decrease in Tb(III) adsorption occurs. It may be concluded that also the presence of low-molecular-weight organic matter, similarly to humic matter, does not cause an additional mobilisation of metals that are desorbed from clay rock in case of pH drops.

The reason of the observed immobilising effects is, however, far from obvious. By means of ^{14}C -labelled compounds, also adsorption of lactate and propionate onto the clay materials was examined. Only for Opalinus clay, adsorbed amounts were significant (Fig. 15). This may be due to the high degree of mineral dissolution (see Fig. 11). For Opalinus clay, amounts of released metals were found to be

considerably higher than for illite and montmorillonite. Presumably, the organic anions form complexes with these metals and may be adsorbed as such. It is thus possible that mixed complexes with Tb(III) are formed, which are stronger adsorbed than Tb(III) as an aqueous species. This may also apply to the other clay materials, even though no adsorption was found for the organic compounds in the absence of Tb(III).

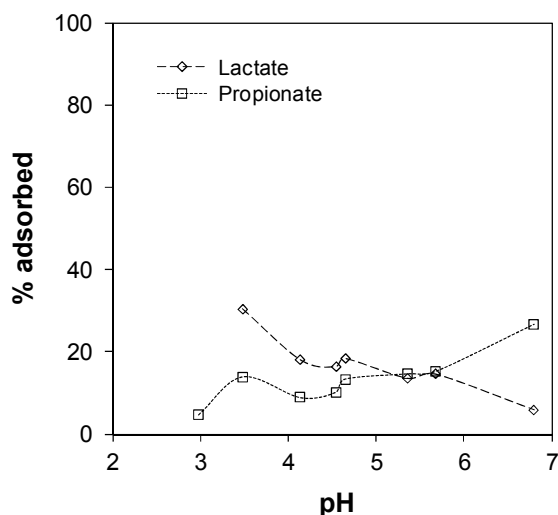


Figure 15. Adsorption of Na L-lactate and Na propionate (2×10^{-4} M) onto Opalinus clay (1 g L^{-1}) in 0.1 M NaClO_4 as a function of pH.

A contrary explanation is conceivable as well, namely, that the competition effect of released metals with respect to Tb(III) adsorption is reduced by the complexation process, given that the organic complexes are less adsorbed than the free metals. However, both these interpretations cannot be corroborated quantitatively and are thus merely speculative at this stage. Further studies are certainly necessary. Nonetheless, these findings show that the high electrolyte contents in pore waters must be explicitly considered when investigating the influence of clay organics.

3.3. Radiotracer studies on the dynamics of adsorption equilibria for the system Tb(III) / humic acid / kaolinite

These basic investigations were performed with kaolinite KGa-1b as a well-defined clay material of high purity. In addition to Aldrich humic acid, a fulvic acid isolated from bog water was used as an organic component. First, the kinetics of adsorption was examined for both humic substances. The results are shown in Fig. 16. For the humic acid, it takes about 2 days until the adsorption equilibrium is attained, which is very long compared to adsorption of metals for example. For the fulvic acid, the final state is already reached after few hours, probably due to the lower average molecular weight of this material.

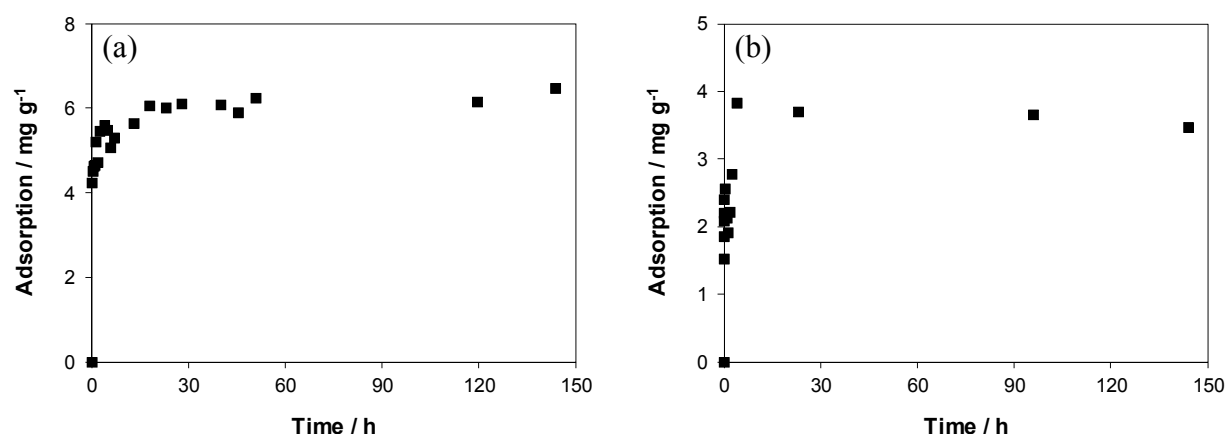


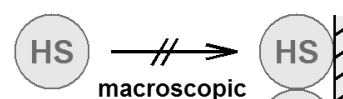
Figure 16. Adsorption of humic acid (a) and fulvic acid (b) onto kaolinite as a function of time (150 mg L⁻¹ HA or FA, 5 g L⁻¹ kaolinite, 0.1 M NaClO₄, pH 4.7, analysis: UV-Vis spectrometry – extinction at 400 nm).

The character of this equilibrium state is, however, an open question. As outlined in the introduction, low recoveries are obtained in flow-through experiments with packed columns. This may indicate that adsorption of humic substances is in part irreversible. Filtration effects, considered as a second possible reason, are unlikely to occur in column fillings with coarse particles (grain sizes in the mm range).

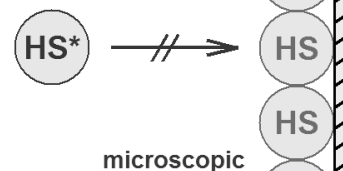
In this project, direct investigations on the reversibility of adsorption of humic materials were realised for the first time, taking advantage of the radiolabelling principle. In this way, it is possible to “look into” the dynamics of adsorption equilibria. The experimental approach is illustrated in Fig. 17. The state of surface saturation is visible from the fact that an increase in concentration no longer results in an increase in adsorption; the adsorption isotherm reaches a plateau. In this situation, a radiolabelled tracer is added to the system. If it is not adsorbed, the equilibrium is a static one. Adsorption is then a “sticking”, i.e., the interaction process is irreversible. If, however, a decrease in the concentration of the tracer is detected, an exchange must take place since free binding sites are not available. In this case, it can be concluded that there is a dynamic equilibrium of adsorption and desorption, i.e., the interaction process is reversible, and there is a permanent movement onto the surface and back into the solution.

Surface saturation:

no further adsorption when increasing the concentration

**Static equilibrium, irreversible adsorption:**

labelled tracer HS^* is not adsorbed

**Dynamic equilibrium, reversible adsorption:**

labelled tracer HS^* is adsorbed



Figure 17. Principle of tracer exchange experiments on the reversibility of adsorption of humic substances (HS).

For these studies, kaolinite suspensions were prepared as described in Section 2.2.3. The experimental conditions were not limited to the state of surface saturation. Instead, a series of systems was prepared for a range of HS concentrations (4 mg L^{-1} - 180 mg L^{-1}) to cover the whole adsorption isotherm, using non-labelled humic substances. The systems were completed by adding a small amount of ^{14}C -labelled humic material as a radiotracer. The concentration of the tracer solution was 0.1 mg L^{-1} , and the added volume of $20 \mu\text{L}$ was negligible compared to the total volume of 4 mL . Thus, the composition of the systems was not significantly changed by introducing the tracer.

Two different procedures were applied: In 1-step experiments, the radiotracer was added together with the non-labelled substance. In 2-step experiments, the tracer was not introduced right from the beginning. First, the system was allowed to equilibrate, containing the non-labelled substance only. An equilibration time of 48 h (end-over-end rotation) was chosen according to the adsorption kinetics shown in Fig. 16a. Subsequently, the tracer was added, and the system was again rotated for 48 h.

A prerequisite of this experimental concept is that the radiolabelled humic molecules are representative of the humic material as a whole, i.e., the labelling reaction must not be selective towards any fractions with specific properties, and the chemical modifications must be minor enough to avoid changes in the behaviour. In Fig. 18, adsorption isotherms for humic acid, obtained by using different analytical methods, are compared. The depletions in the adsorption experiment were determined (i) by means of UV-Vis spectrometry and (ii) by analysis of the ^{14}C -labelled tracer (1-step experiment). In the latter case, the measured decrease in the concentration of the tracer is scaled up to the decrease in the total concentration of humic acid. Here, the UV-Vis data were also needed to correct the measured count rates for colour quenching by HA. For this purpose, the decrease in the count rate at a constant tracer concentration was determined for aqueous solutions as a function of HA concentration. Obviously, both data sets are in good agreement. So it may be concluded that the humic material is well represented by the labelled portion.

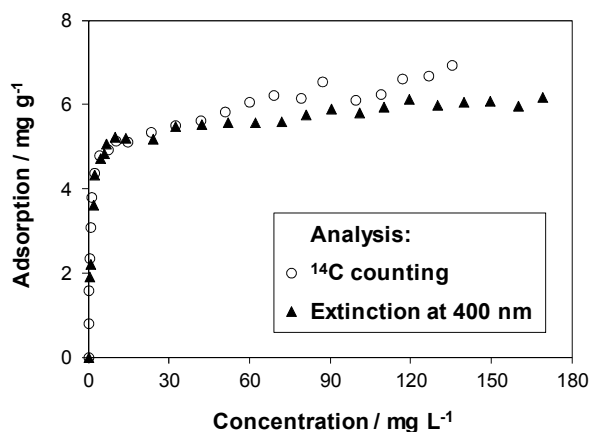


Figure 18. Isotherm of adsorption of humic acid onto kaolinite, based on radiotracer analysis and UV-Vis spectrometric analysis, respectively (5 g L^{-1} kaolinite, 0.1 M NaClO_4 , pH 4.7).

In order to test the experimental strategy, a first study was performed with $[^{160}\text{Tb}]\text{Tb(III)}$, presuming that adsorption is reversible in this case. Fig. 19a shows the results of 1-step and 2-step experiments, conducted according to the procedure described above even though equilibration times of 48 h were not necessary for the metal. The “normal” adsorption isotherm, obtained in the 1-step experiment (open circles), reaches its plateau value at equilibrium concentrations higher than $\sim 60 \text{ mg L}^{-1}$. If the radiotracer is subsequently introduced into these systems, it will certainly be confronted with saturated surfaces. However, the 2-step experiments (full circles) show that adsorption is not blocked at all. Instead, exactly the same adsorption isotherm is obtained. This result is very instructive as it clearly indicates a permanent exchange process between the adsorbed state and the dissolved state, i.e., the radiotracer is involved in a dynamic equilibrium of adsorption and desorption.

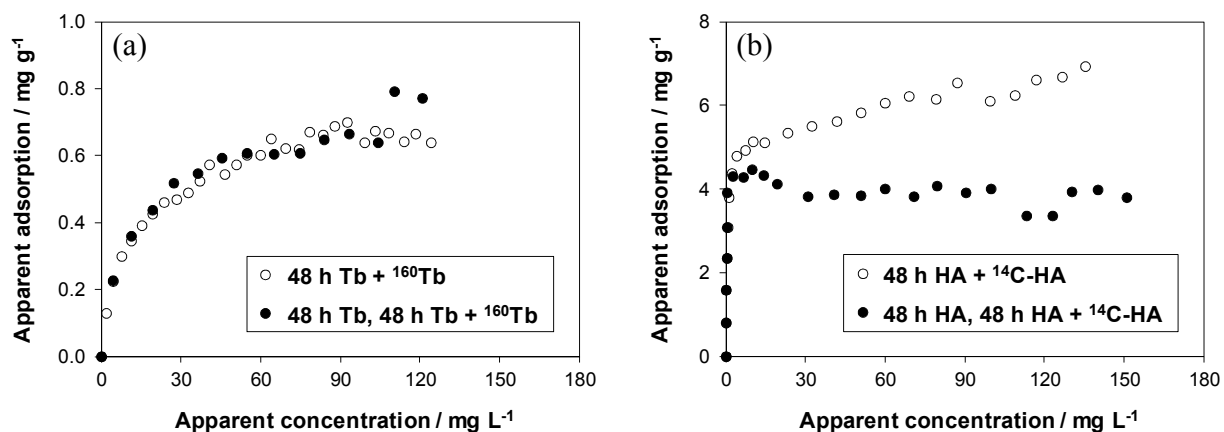


Figure 19. Isotherms of adsorption of Tb(III) (a) and humic acid (b) onto kaolinite in 0.1 M NaClO_4 , obtained with ^{160}Tb and ^{14}C -labelled HA as radiotracers, which were added in small amounts together with the non-radioactive substances (open circles) or after equilibration (full circles). Suspension concentrations for systems with Tb(III) and HA were 25 g L^{-1} and 5 g L^{-1} , resulting in pH values of 4.4 and 4.7, respectively. More details are given in the text.

Fig. 19b shows the results of analogous experiments with humic acid. Evidently, the adsorption isotherms obtained in 1-step and 2-step procedures are not identical. In the latter case, the adsorption plateau is lowered by about one third. However, it is not shifted to zero, which is the most remarkable finding. Consequently, an exchange must take place for humic molecules as well, even though they are extremely large compared to metal ions. It appears that adsorption of humic matter is in fact reversible. There is a dynamic equilibrium, which is, however, not quantitatively represented by the radiotracer. For this reason, the term “apparent” is used in the axis titles.

In view of the intermediate plateau level, it seemed likely that different results would be obtained if the time for exchange was varied. This supposition was confirmed, as can be seen from Fig. 20. If the second equilibration period is reduced to 6 h, the apparent adsorption plateau is situated considerably lower. It is remarkable that a maximum occurs at low concentrations. The following decrease reflects the approach to the state surface saturation. The hindrance of tracer adsorption is in fact limited to the plateau region of the isotherm. In another experiment, the tracer was given 168 h (one week) for exchange. In this case, the plateau level was found to be higher compared to the results for 48 h. If the time is increased to 672 h (4 weeks), further progress of the tracer can be observed.

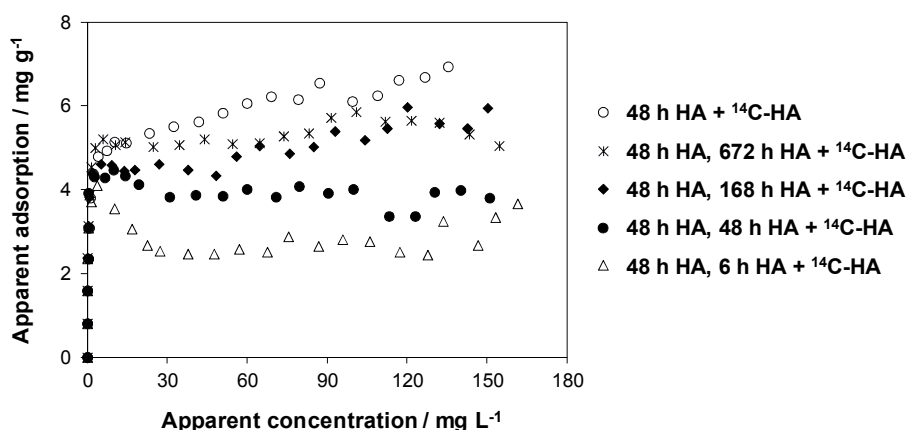


Figure 20. Apparent adsorption isotherms obtained in tracer exchange experiments at different times of exchange (experimental details as in Fig. 18).

In Fig. 21a, the averaged data of all apparent adsorption plateaus are plotted as a function of the time of exchange. Analogous experiments were performed with the fulvic acid. The results obtained (Fig. 21b) turned out to be similar. For both materials, the tracer exchange at surface saturation requires much more time than attaining the overall adsorption equilibrium (cf. Fig. 16). This is surprising since both processes, in principle, are governed by the same dynamics.

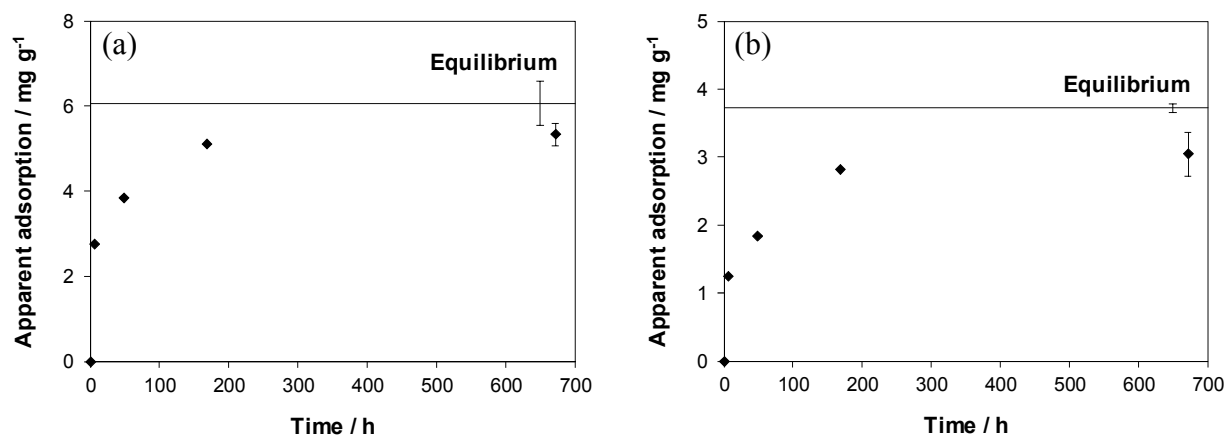


Figure 21. Mean plateau values of apparent adsorption isotherms obtained in tracer exchange experiments with humic acid (a) and fulvic acid (b) at different times of exchange (experimental details as in Fig. 18). The solid lines indicate the mean plateau values of the isotherms obtained for total adsorption (instantaneous tracer addition).

It appeared to be probable that the slow kinetics of exchange might be related to the desorption process as a rate-limiting step. To test this assumption, desorption experiments were performed, covering a time frame of 4 weeks as in the tracer exchange studies. The experimental layout is based on the adsorption isotherm (Figs. 22a and 23a for HA and FA, respectively). Starting from a total concentration of 40 mg L^{-1} HA or FA, a certain equilibrium concentration is attained. After centrifugation, 3 out of 4 mL of the supernatant were replaced by “fresh” 0.1 M NaClO_4 solution. With this dilution, the total concentration is reduced accordingly, and the new equilibrium state can be assigned by means of the adsorption isotherm. The corresponding shifts in adsorption and concentration are shown as grey arrows. Thus, desorption is to be expected. As the increase in concentration is, however, rather small, demands on the analytical precision are high. For the fulvic acid, results obtained by UV-Vis spectrometry were not satisfactory, mainly due to background values caused by dissolution of clay components. Using ^{14}C -labelled FA proved to be indispensable.

The concentrations of HA and FA in the supernatant as a function of time (after dilution) are shown in Figs. 22b and 23b, respectively. For the humic acid, no change in concentration was detected over the entire time span. For the fulvic acid, a minor decrease was observed. Apparently, there is a delayed adsorption process in spite of the dilution step. This is surprising, the more so as no comparable trend was observed in the adsorption kinetics (Fig. 16b). The essential outcome of these experiments is, however, that the expected desorption process does not take place for both humic materials.

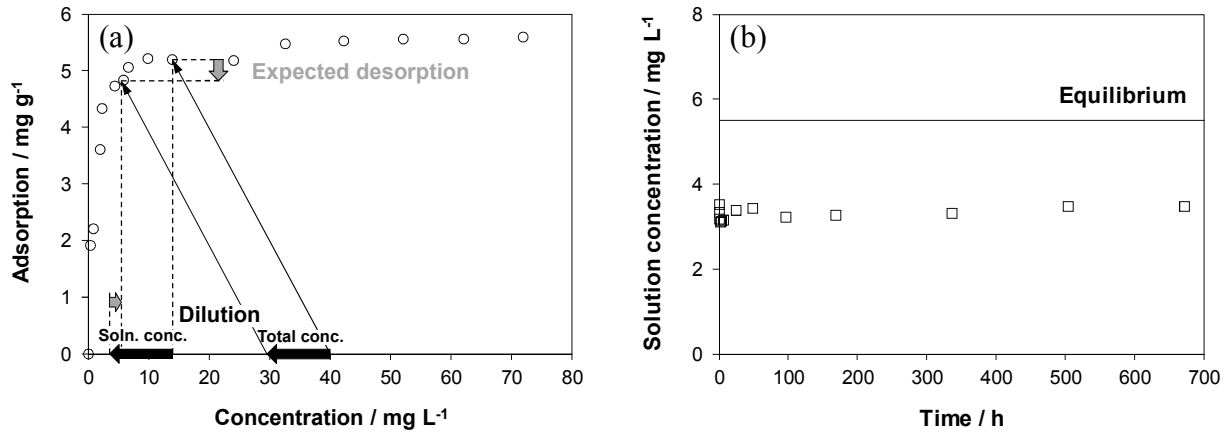


Figure 22. Desorption experiments with humic acid. Expected desorption after dilution, based on the adsorption isotherm (a), and measured solution concentrations after dilution as a function of time (b) (5 g L⁻¹ kaolinite, 0.1 M NaClO₄, pH 4.7, analysis: UV-Vis spectrometry – extinction at 254 nm).

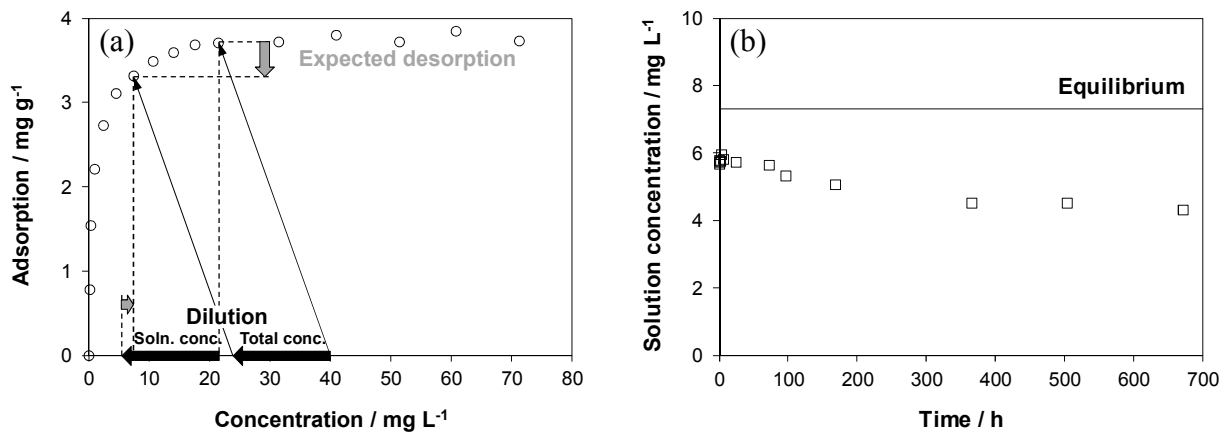


Figure 23. Desorption experiments with fulvic acid (¹⁴C-labelled). Expected desorption after dilution, based on the adsorption isotherm (a), and measured solution concentrations after dilution as a function of time (b) (5 g L⁻¹ kaolinite, 0.1 M NaClO₄, pH 4.7, analysis: ¹⁴C counting).

These results are problematic in view of reactive transport modelling since reversibility of adsorption is presumed in general (see literature review in [9]). On the other hand, the absence of any desorption is contradictory to our findings obtained from the tracer exchange experiments described above. If desorption is impossible, there should not be any exchange as well. Possibly, the competition exerted by the ¹⁴C-labelled tracer is a stronger driving force than a concentration gradient. The discrepancy is still in need of full clarification.

3.4. Elucidating time-dependent changes in the competition effect of Al(III) on Tb(III)-humate complexation

3.4.1. Evidence of stabilisation processes

The results of time-dependent complexation studies, obtained by using the anion exchange method, are shown in Fig. 24. Al(III) / HA systems had been pre-equilibrated over a time period of up to 6 days before Tb(III) was added. The dotted line in Fig. 24a shows the percentage of Tb(III) bound to HA in the absence of Al(III). The competition effect of Al(III) is reflected in the distance of the data points from this line.

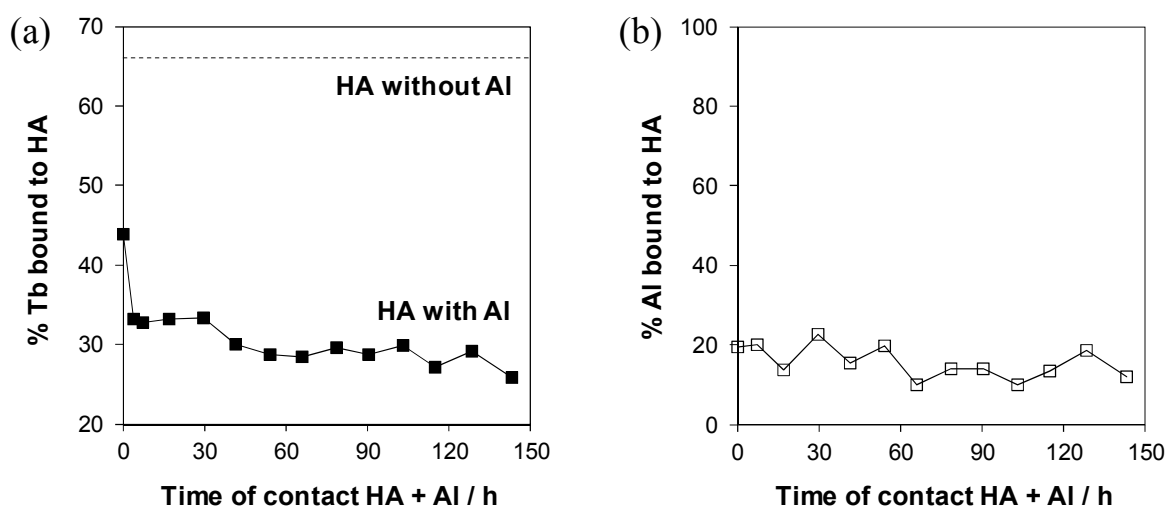


Figure 24. Complexation of Tb(III) with HA after pre-equilibration of HA and Al(III) (a) and complexation of Al(III) with HA (b) as a function of contact time, determined by the anion exchange method (10^{-7} M [^{160}Tb]Tb, 10^{-5} M Al, 5 mg L^{-1} HA, 0.1 M NaClO_4 , pH 4.0).

About one third of originally bound Tb(III) is instantaneously excluded from complexation, and interestingly, there is a further significant decrease within a period of 2 days. No corresponding changes in the stability of Al(III)-humate complexes were detectable, i.e., the amount of bound Al(III) was constant during the time of observation (Fig. 24b). Consequently, the increase in competition must be based on qualitative changes. A parallel series of experiments was prepared to cover a range of ageing times of up to 6 months since in the previous project, trends in the competition effect of Fe(III) were found on this time scale [64, 65]. However, no further changes in the humic-bound fractions of Tb(III) were observed in the Al(III) system.

To elucidate the background of the time-dependent effect, our first attention was given to possible shifts in the pH value of Al(III) / HA systems. For Fe(III), we found that the time-dependent increase in competition was accompanied by a concomitant increase in pH. Since reversal of Fe(III) hydrolysis is the only proton-consuming process possible in this system, we concluded that the polynuclear hydrolysis species are metastable when bound to HA. They are only slowly degraded, and the

increase in the counteractive effect is thus explained by the delayed occupation of binding sites [64].

Also the aqueous chemistry of Al(III) is characterised by the formation of polynuclear species. Depending on the concentration, the tridecamer $[\text{AlO}_4\text{Al}_{12}(\text{OH})_{24}(\text{H}_2\text{O})_{12}]^{7+}$ (“Al₁₃”) can dominate the speciation in weakly acidic solutions [66]. For Al(III) / HA systems, however, the time-dependent development of the pH value turned out to be completely different (Table 4). A decrease occurred straight away, and no further change was observed over a period of 4 weeks.

Table 4. Time-dependent changes in pH for metal / HA systems (5×10^{-5} M Fe(III) or Al(III), 20 mg L^{-1} HA).

Time	Fe(III) / HA	Al(III) / HA
0 min	pH 5.0	pH 5.0
5 min	pH 5.1	pH 4.6
28 days	pH 5.3	pH 4.6

Such a pH drop is the normal effect to be expected when metal ions are bound to acidic groups of humic substances since protons are released in exchange for the metal. Two different conclusions may be drawn: (a) Polynuclear Al(III) species remain stable when interacting with HA, or (b) the polycations are destructed immediately, consuming fewer protons than are released from the humic ligands. Anyway, the observed time dependence in the competition effect cannot be explained by a metastability of polynuclear species in this case.

Interestingly, this time frame corresponds to kinetic effects in respect of complex dissociation reported in the literature [10-12]. Based on these findings, a “diffusion theory” has been established. According to this hypothesis, complexation proceeds in two steps (Fig. 25a): Subsequent to a fast equilibration with weak binding sites on the colloid surface, there is a slow in-diffusion process to stronger sites which are not directly accessible.

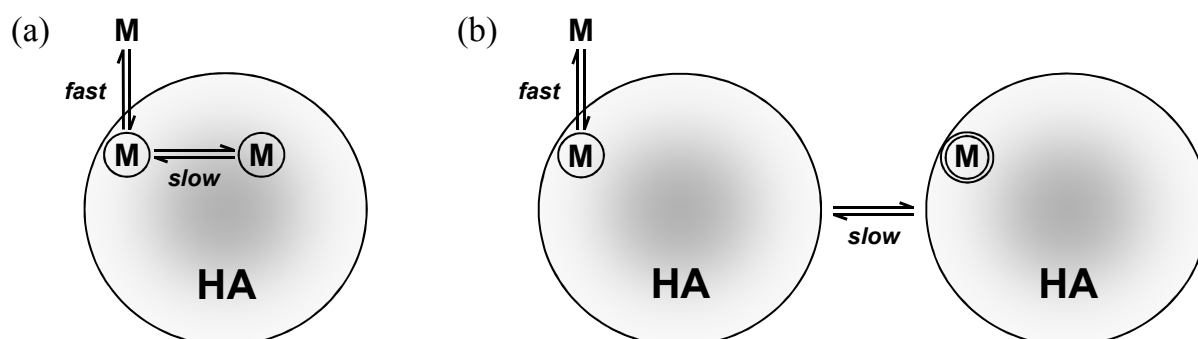


Figure 25. Intra-molecular “diffusion” (a) and on-site stabilisation (b) as possible explanations for an increase in complex inertness with time of contact.

This interpretation is now widely accepted as it provides a plausible explanation for an increasing hindrance of complex dissociation. However, in consideration of the fact that a similar time dependence was found for the competition effect on complex formation, the theory must be called into question since both phenomena probably reflect one and the same process. If we assume that Al(III) migrates from outer sites to inner sites during the time span concerned, the access for Tb(III) should be facilitated with time because the initial sites of Al(III) are vacated; but on the contrary, binding of Tb(III) is impeded with time. Consequently, in-diffusion cannot serve as an explanation for our results, and because of the temporal accordance, it may be inferred that this assumption is also inapplicable to the dissociation studies described in the literature.

Instead, our findings give rise to the conclusion that bound metals do not leave their initial binding sites but the sites themselves get “stronger”, as schematically illustrated in Fig. 25b. We suppose that structural changes are induced in the surroundings of the metal, keeping it more and more trapped, for instance due to bridging effects. In this way, the metal becomes less exchangeable for competing metals, and also the access to free binding sites may be increasingly hindered.

3.4.2. Spectroscopic probing

With the objective of providing evidence of structural alterations, we employed time-resolved laser-induced fluorescence spectroscopy (TRLFS) as a powerful technique for probing rearrangement processes on a molecular scale. Figure 26a shows the fluorescence decay of Tb(III), which is indirectly excited by the humic acid.

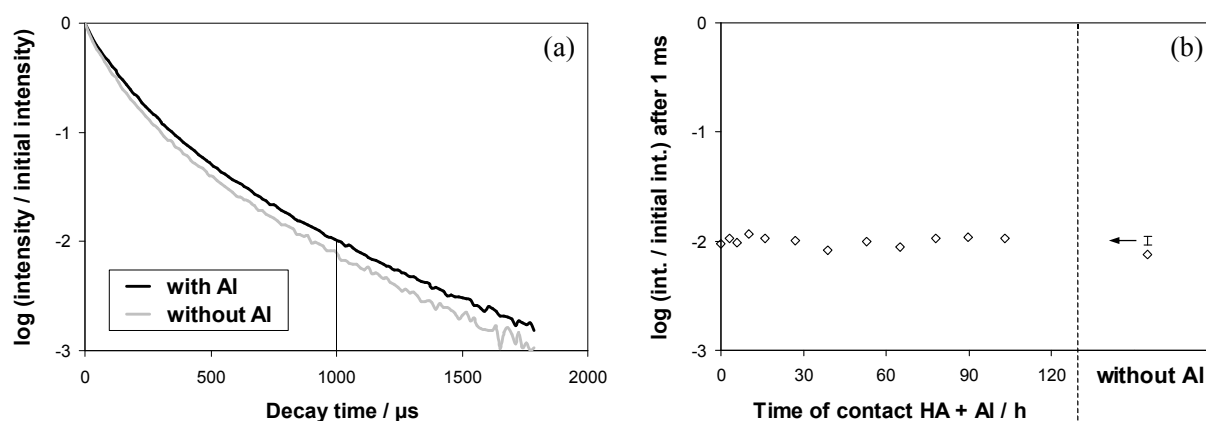


Figure 26. Fluorescence decay of Tb(III) in contact with HA in the absence and presence of Al(III) (a); decay value after 1 ms as a function of contact time (b) (10^{-5} M Tb, 2×10^{-5} M Al, 10 mg L^{-1} HA, 0.1 M NaClO_4 , pH 4.0, $\lambda_{\text{exc}} = 325.0 \text{ nm}$). The error bar indicates the standard deviation around the mean value of the time-dependent data series. The decay curve for the system with Al consists of the averaged data of all curves obtained for different contact times.

Generally, the fluorescence lifetime of the metal depends on the presence of opportunities for energy transfer, e.g., to water or other ligands, but also back to the humic molecule. This energy back transfer depends on the molecular structure in the microenvironment of Tb(III). Consequently, the fluorescence decay may be sensitive to possible changes induced by complexation with Al(III). In fact, it can be seen that the fluorescence lifetime is significantly influenced by the presence of Al(III).

In Fig. 26b, relative intensities after a decay time of 1 ms are plotted for Al(III) / HA systems that had been allowed to stand for different time periods before Tb(III) was added. On the right-hand side, the value for the system without Al(III) is shown together with the range of variation for the time-dependent data series. The time frame was chosen according to the observed increase in the competition effect. However, no corresponding trend can be found in the intensity values. The reflected structural changes occur immediately and thus cannot be the background of the stabilisation process in question.

The impact of Al(III) complexation is also visible in the fluorescence emission spectrum of the humic acid (Fig. 27a). The fluorescence is quenched in the range of higher wavelengths, i.e., the fluorophores with the largest π -systems are most influenced. Also these spectra do not show any dependence on the ageing time of Al(III) / HA systems, shown for the fluorescence intensity at 500 nm in Fig. 27b.

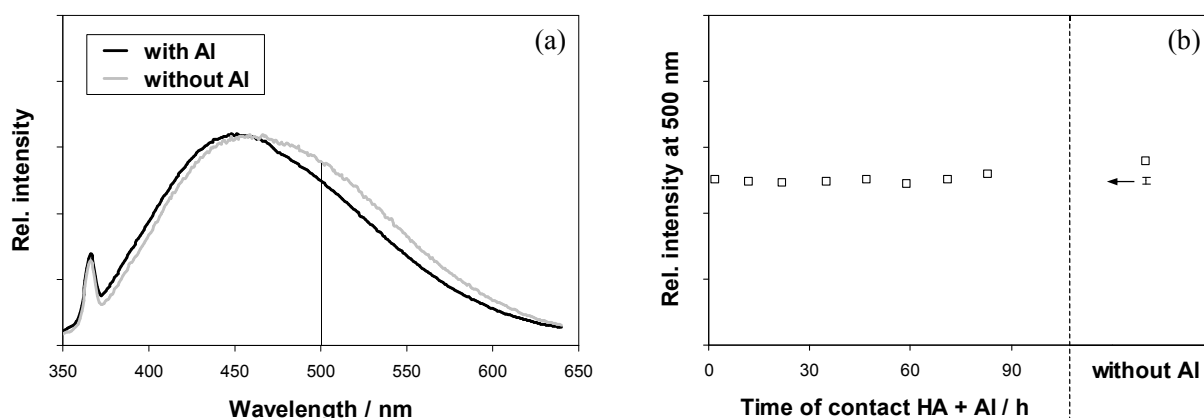


Figure 27. Fluorescence spectrum of humic acid in the absence and presence of Al(III) (a); intensity at 500 nm as a function of contact time (b) (2×10^{-5} M Al, 10 mg L^{-1} HA, 0.1 M NaClO_4 , pH 4.0, $\lambda_{\text{exc}} = 325.0 \text{ nm}$). Averaged data were used analogously to Fig. 26.

Further attempts to find indications of rearrangement processes on a longer time scale were undertaken with Eu(III) as a probe metal, which can provide more detailed information than Tb(III). Figure 28 shows fluorescence emission spectra of Eu(III), recorded by TRLFS with an initial delay of $10 \mu\text{s}$ to skip the fast decaying fluorescence of humic acid (cf. Fig. 27a). The two main spectral bands around 592 nm and 615 nm are assigned to the $^5\text{D}_0 \rightarrow ^7\text{F}_1$ and $^5\text{D}_0 \rightarrow ^7\text{F}_2$ transitions, respectively. At an excitation wavelength (λ_{exc}) of 361.7 nm, Eu(III) is directly excited (black spectrum). In the presence of humic acid, the fluorescence is enhanced by an

energy transfer from the humic ligands, i.e., there is an indirect excitation in addition (grey spectrum).

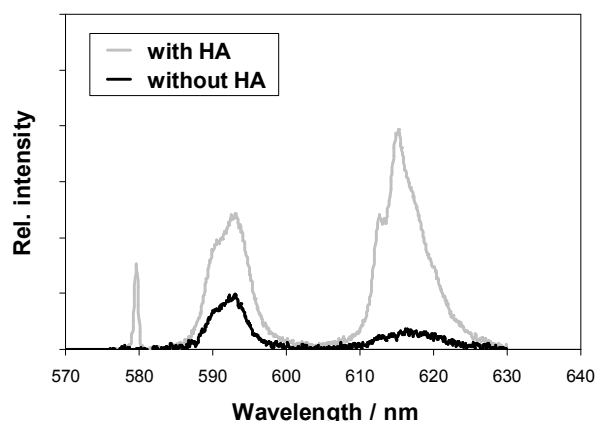


Figure 28. Fluorescence spectrum of Eu(III) in the absence and presence of HA (10^{-5} M Eu, 10 mg L^{-1} HA, 0.1 M NaClO_4 , pH 4.0, $\lambda_{\text{exc}} = 361.7 \text{ nm}$).

If the excitation wavelength is only slightly lowered to 356.0 nm, the direct excitation mode no longer exists, and Eu(III) is only indirectly excited by humic acid (Fig. 29a). When comparing the peak ratios, one can recognise that the grey spectrum in Fig. 28 is a composite of the grey spectrum in Fig. 29a and the black spectrum in Fig. 28. In a more quantitative analysis by a fitting procedure, the composite spectrum obtained via direct and indirect excitation can be separated into two constituent spectra resulting only from direct and only from indirect excitation, respectively. In this way, the Eu(III)-humate complex can be distinguished from non-bound Eu(III), and the humic-bound fraction can be directly derived from the relative contributions of the constituent spectra. In addition to this quantitative information, the spectrum is also sensitive to possible qualitative changes in the microenvironment of humic-bound Eu(III).

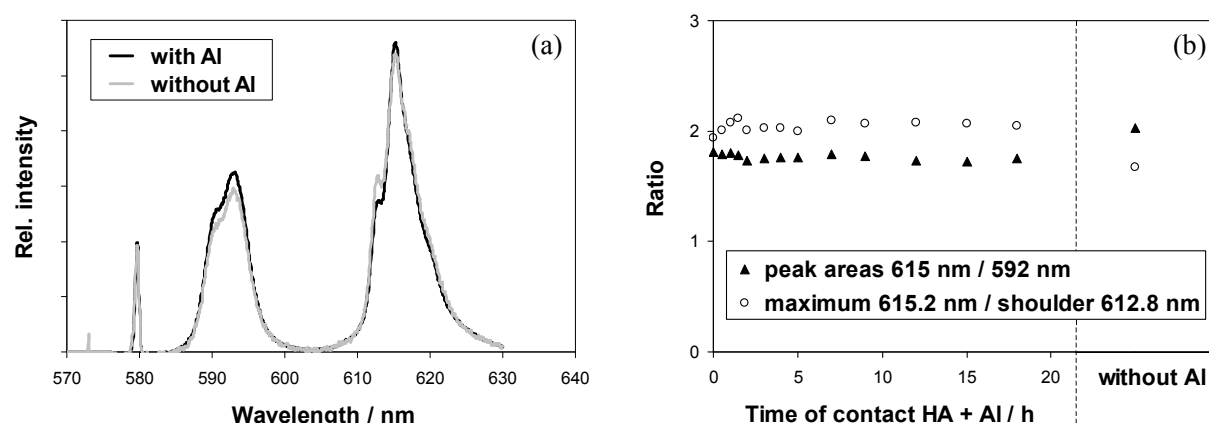


Figure 29. Fluorescence spectrum of Eu(III) in contact with HA in the absence and presence of Al(III) (a); intensity ratios as a function of contact time (b) (10^{-5} M Eu, 2×10^{-5} M Al, 10 mg L^{-1} HA, 0.1 M NaClO_4 , pH 4.0, $\lambda_{\text{exc}} = 356.0 \text{ nm}$). The spectrum for the system with Al consists of the averaged data of all spectra obtained for different contact times.

As can be seen in Fig. 29a, the intensity ratios within the spectrum are indeed slightly altered in the presence of Al(III). The integral intensity (area) of the band around 592 nm is increased with respect to the band around 615 nm, and the maximum intensity of the sub-band (shoulder) at 612.8 nm is decreased with respect to the band maximum at 615.2 nm. Since only humic-bound Eu(III) is “visible” at an excitation wavelength of 356.0 nm, these changes are not attributable to the partial displacement of Eu(III) by Al(III). Obviously, there are structural rearrangements. In Fig. 29b, the specified spectral features are plotted for systems where Al(III) and HA had been in contact for different time periods before Eu(III) was introduced. Again, it turned out that the changes occurred at once, and there was no indication of a time-dependent trend corresponding to the competition effect.

Such a time-dependent series of spectra was also recorded at an excitation wavelength of 361.7 nm where Eu(III) is excited both directly and indirectly. Together with the spectrum for Eu(III) in the absence of HA and the time-dependent spectra for indirect excitation ($\lambda_{\text{exc}} = 356.0 \text{ nm}$), these data allowed us to calculate the respective proportions of humic-bound Eu(III) as described above. They are shown in Fig. 30. The competition effect of Al(III) is clearly visible. However, a time dependence is not discernible from these data.

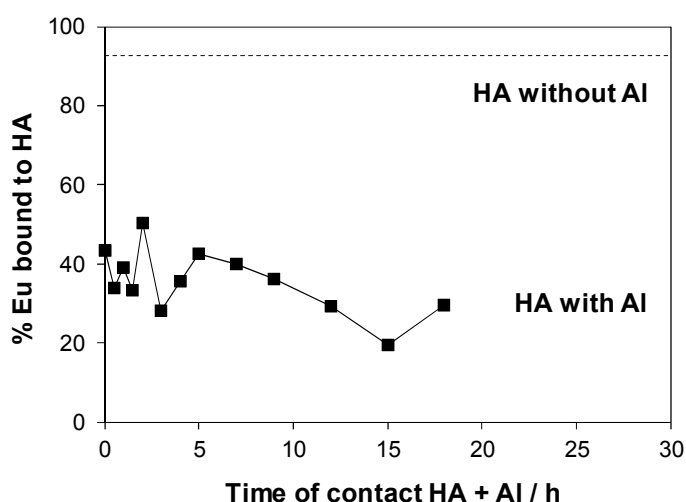


Figure 30. Complexation of Eu(III) with HA after pre-equilibration of HA and Al(III), determined by analysis of Eu(III) fluorescence spectra at $\lambda_{\text{exc}} = 356.0 \text{ nm}$ and $\lambda_{\text{exc}} = 361.7 \text{ nm}$ (concentrations as specified in Fig. 29).

At first sight, this result is surprising since it seems to contradict the findings for Tb(III) shown in Fig. 24a. It must be noted, however, that the concentration of Eu(III) is higher by two orders of magnitude. A concentration of at least 10^{-5} M is necessary to obtain sufficient fluorescence intensity. This is half of the concentration of Al(III), which was proven to induce instantaneous structural rearrangements. Thus, it is not unlikely that the subsequent addition of Eu(III) has similar implications. If the time dependence in the competition effect, observed for 10^{-7} M Tb(III), is caused by comparatively minor changes, these are probably outweighed by the complexation of the probe metal, and consequently, the kinetic effect simply does not occur. Possibly, this reasoning may also be applied to the TRLFS studies with Tb(III) where the same probe concentration was used, i.e., the probe metal could not “see” time-dependent

changes because they were eliminated by the probe itself. In addition, however, the fluorescence spectra of Al(III) / HA systems, recorded in the absence of probe metals, did not show any time-dependent trend (Fig. 27). One may conclude that stabilising rearrangements as a basis of the kinetic effect cannot be very massive compared to the initial impact of Al(III) complexation.

3.5. Transport studies by means of positron emission tomography

3.5.1. Advection in homogenised clay samples

Kaolinite test sample. A first continuous injection test was conducted with the sample Kao, which is a compacted sample prepared with a kaolinite-sand suspension. The fluid contained 0.01 M [^{124}I]KI with an activity of 66 MBq, the flow rate was set to 0.005 mL min $^{-1}$, and the pressure was 0.4 MPa. 40 images were recorded during the experimental period of one week. A selection of these images is shown in Fig. 31. The partial assembly of the scanner with only 8 cassettes caused noisy images. However, the tracer propagation is clearly discernible as a homogeneous dispersive advection.

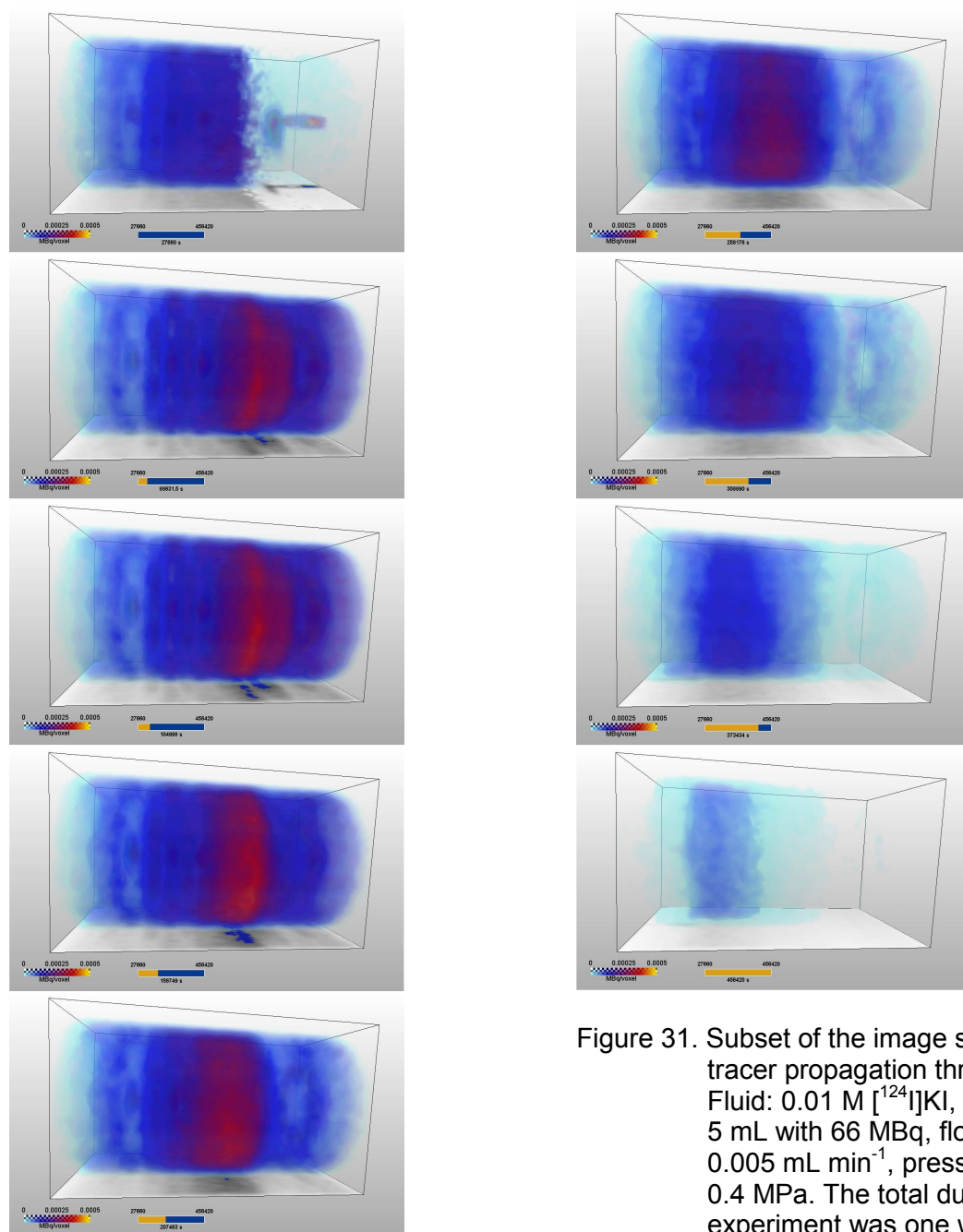


Figure 31. Subset of the image sequence of tracer propagation through Kao. Fluid: 0.01 M [^{124}I]KI, tracer pulse: 5 mL with 66 MBq, flow rate: 0.005 mL min $^{-1}$, pressure: 0.4 MPa. The total duration of the experiment was one week.

The tracer propagation was considered as 1D-dispersive advection and was analysed accordingly using CXTFIT (Figs. 32 and 33). The fit was based on the sum-activity of selected slices because the fitting algorithm is limited to a relatively small number of data points (about 150). The fit results indicated a velocity of 0.47 mm h^{-1} and a dispersivity of $1.1 \times 10^{-9} \text{ m}^2 \text{ s}^{-1}$.

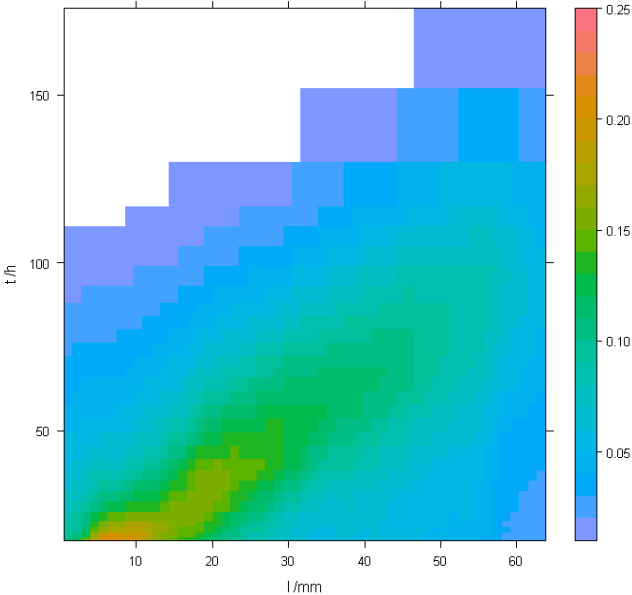


Figure 32. Sum of activity over each slice versus axial location and propagation time.

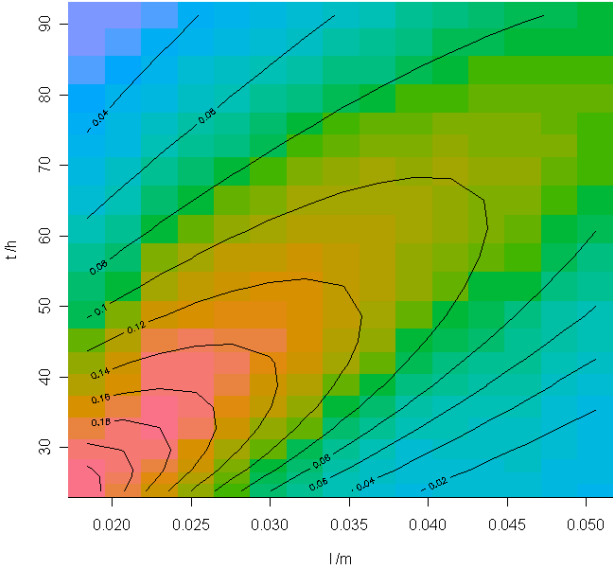


Figure 33. CXTFIT best-fit curves in the region unaffected by boundary effects.

Opalinus clay test sample. The sample OPA1 was made by compaction of a suspension of Opalinus clay powder in synthetic OPA pore water, which was also used as injection fluid together with 0.01 M KI as a carrier. Again, ^{124}I was applied as a tracer, injected as a pulse of 4 mL. The flow rate was 0.02 mL min^{-1} , and the

pressure was 0.3 MPa. 26 images were recorded during 50 hours (selection in Fig. 34). The images were considerably clearer than in the study with Kao because the scanner had been extended from 8 to 20 cassettes. However, significant image artifacts were still caused by initial technical deficiencies. The images generally show dispersive plug flow with minor lateral inequalities, but without preferential flow paths.

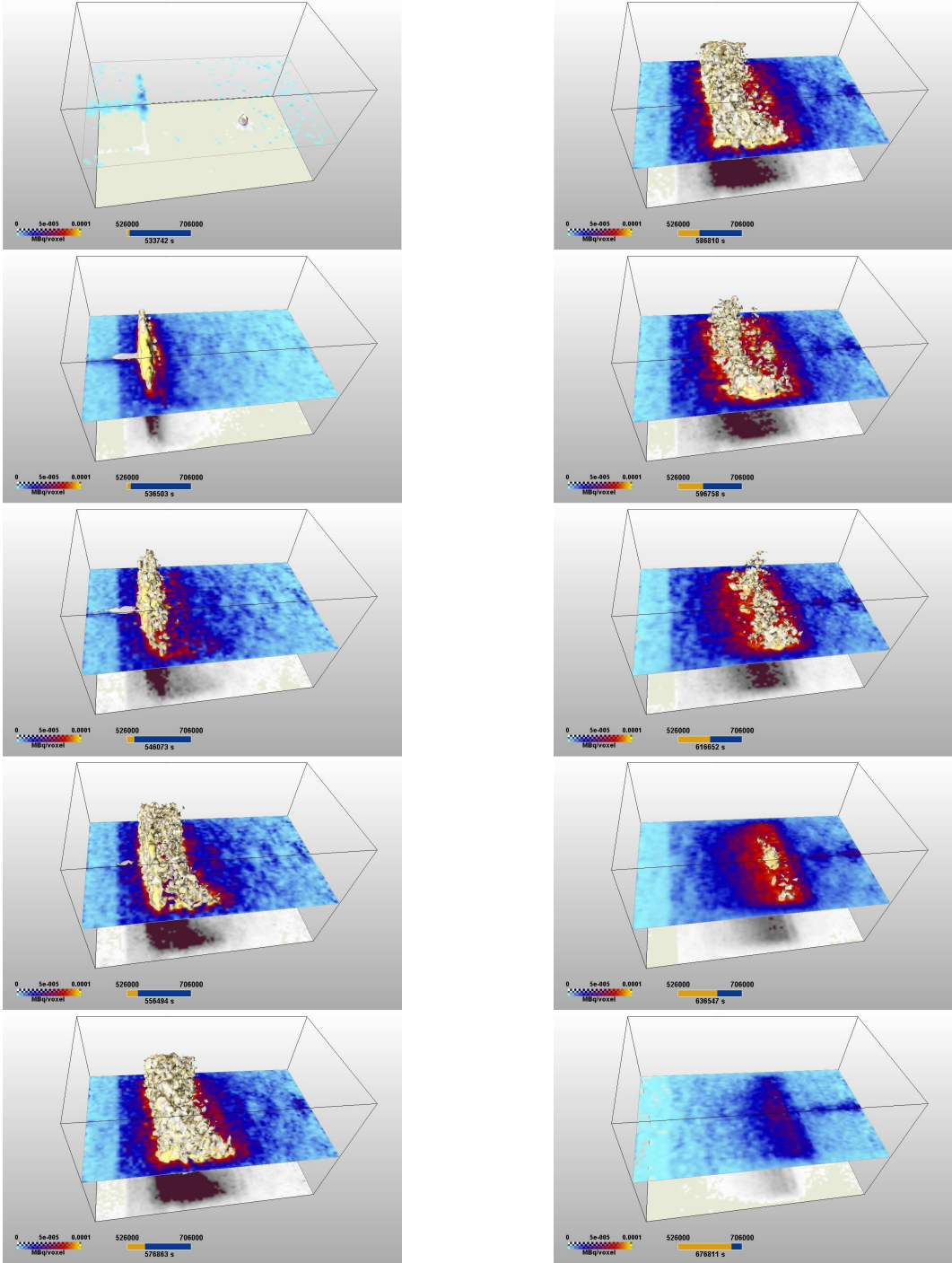


Figure 34. Conservative injection test with $[^{124}\text{I}]\text{KI}$ and OPA1 (projection at the bottom, central slice colour-coded, isosurface of distribution of maximum activity).

Smoothing splines with respect to time were applied to all 215000 points of the image. The maximum of the smoothing curve was identified as a convenient measure of the arrival time. This maximum value can be interpreted as transport efficiency of the individual spatial points. Low values of this maximum imply no significant contribution of this voxel to the transport process. Thus, a 3D-data set of the pathway efficiency (maximum value of activity) and of the arrival times (which can be interpreted as velocity distribution) could be derived (Fig. 35).

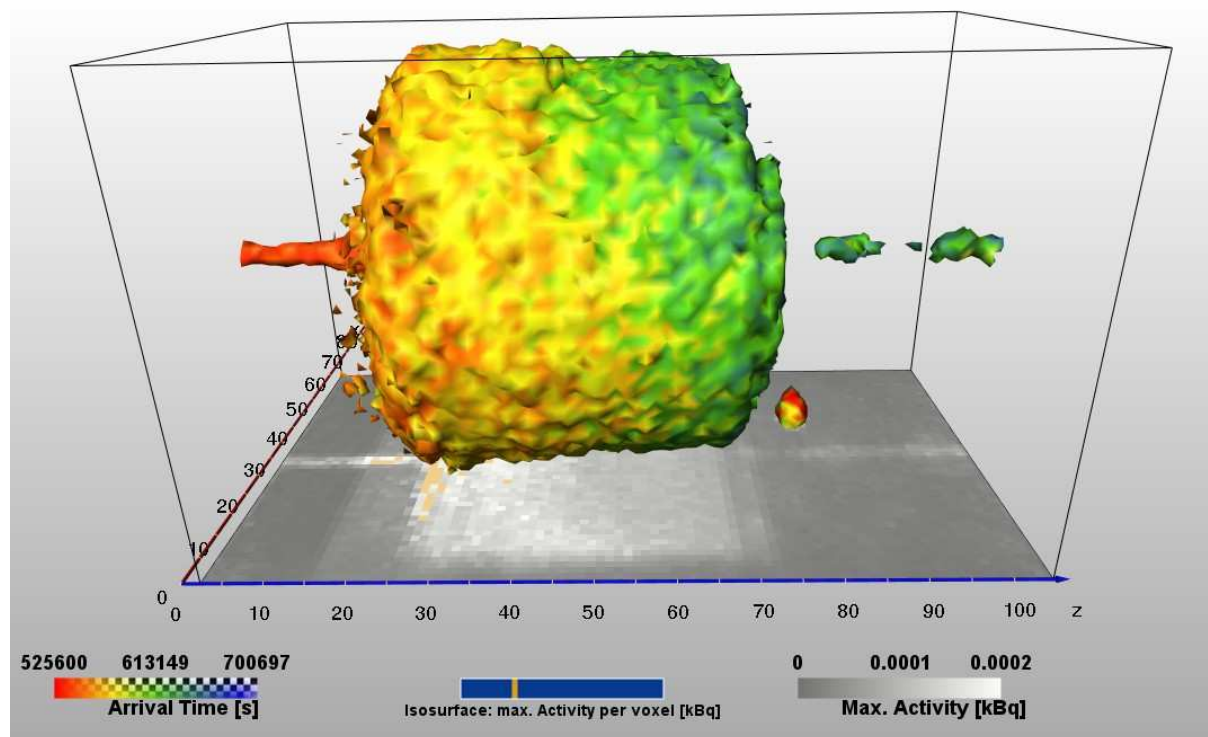


Figure 35. Travel time (colour-coded) and pathway efficiency (projection on the horizontal plane) for OPA1 (conservative tracer test), showing slight lateral differences.

A second study on OPA1 was conducted with Aldrich humic acid (50 mg L^{-1}), labelled with ^{124}I by the Iodogen method. It was injected into the sample without prior conditioning with HA solution. The sample contained the carrier solution from the preceding experiment (OPA water with 0.01 M KI). The flow rate was 0.01 mL min^{-1} , the pressure was 0.3 MPa . 32 images were taken during 10 days of injection (Figs. 36 and 37). During the whole period, the most part of detected ^{124}I remained immobile in the sample near the injection end plate, while a small portion travelled with a velocity corresponding to the preceding experiment. This fraction was identified as free iodide, probably a residue of the labelling procedure.

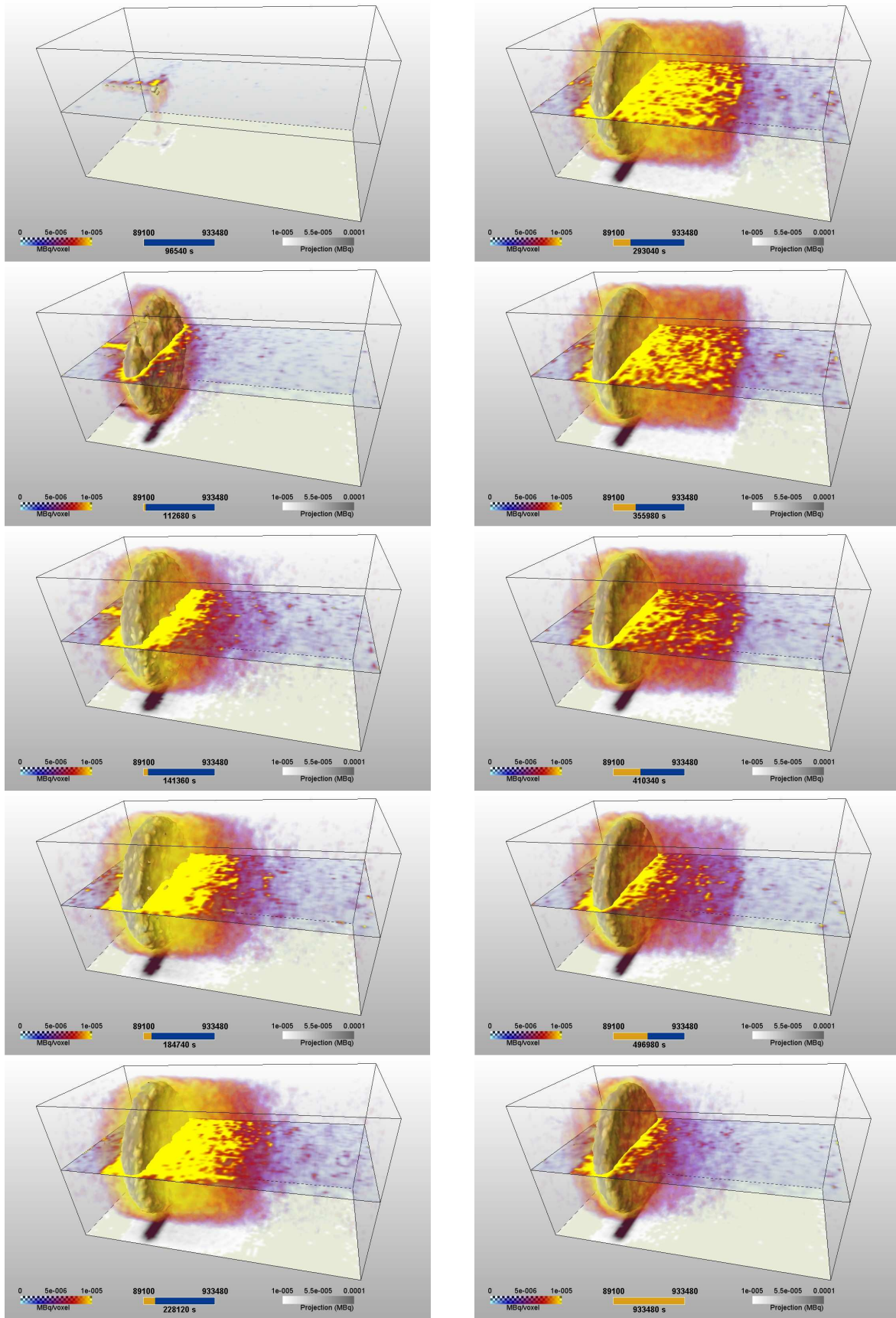


Figure 36. Flow test with ^{124}I -labelled HA and OPA1 (projection at the bottom, central slice colour-coded, isosurface of distribution of maximum activity).

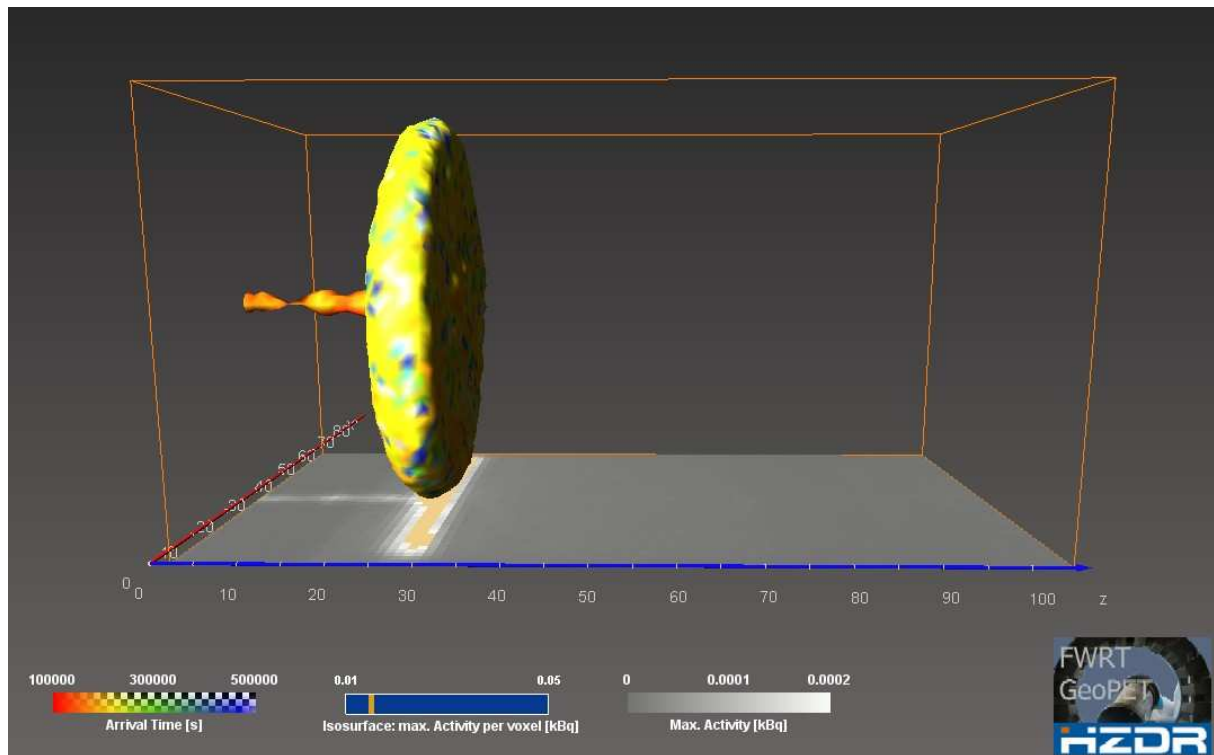


Figure 37. Travel time (colour-coded) and pathway efficiency (projection on the horizontal plane) for OPA1 (flow test with ^{124}I -labelled HA), showing immobility of the tracer at the inlet.

Synthetic sand-bentonite column Nagra1. Nagra1 is a compacted 80/20-sand-bentonite sample with an initial water content of 10%. The density after compaction was 1.5 g cm^{-3} (max. porosity ~ 0.65 , considering saturated conditions after compaction). After conditioning with 40 mL synthetic Grimsel formation water (“Grimsel water”) [67] at a flow rate of $0.001 \text{ mL min}^{-1}$, 100 mL of Grimsel water with ^{58}Co cobalt hexacyano complex (0.5 MBq mL^{-1}) were injected at the same flow rate. The first arrival of the tracer occurred after injection of 27 mL. The maximum specific activity of 0.07 MBq mL^{-1} was reached after injection of 60 mL. In spite of diffuse and noisy PET images (Fig. 38), probably due to the noise generated by the additional γ -activity of the non-ideal PET nuclide ^{58}Co , it can be seen that the tracer distribution is very inhomogeneous. During the whole period, the evolution of the tracer distribution was uneven and patchy, with a strong increase in activity from the axis to the cylinder surface and a steady gradient from the inlet to the outlet until termination of the injection period.

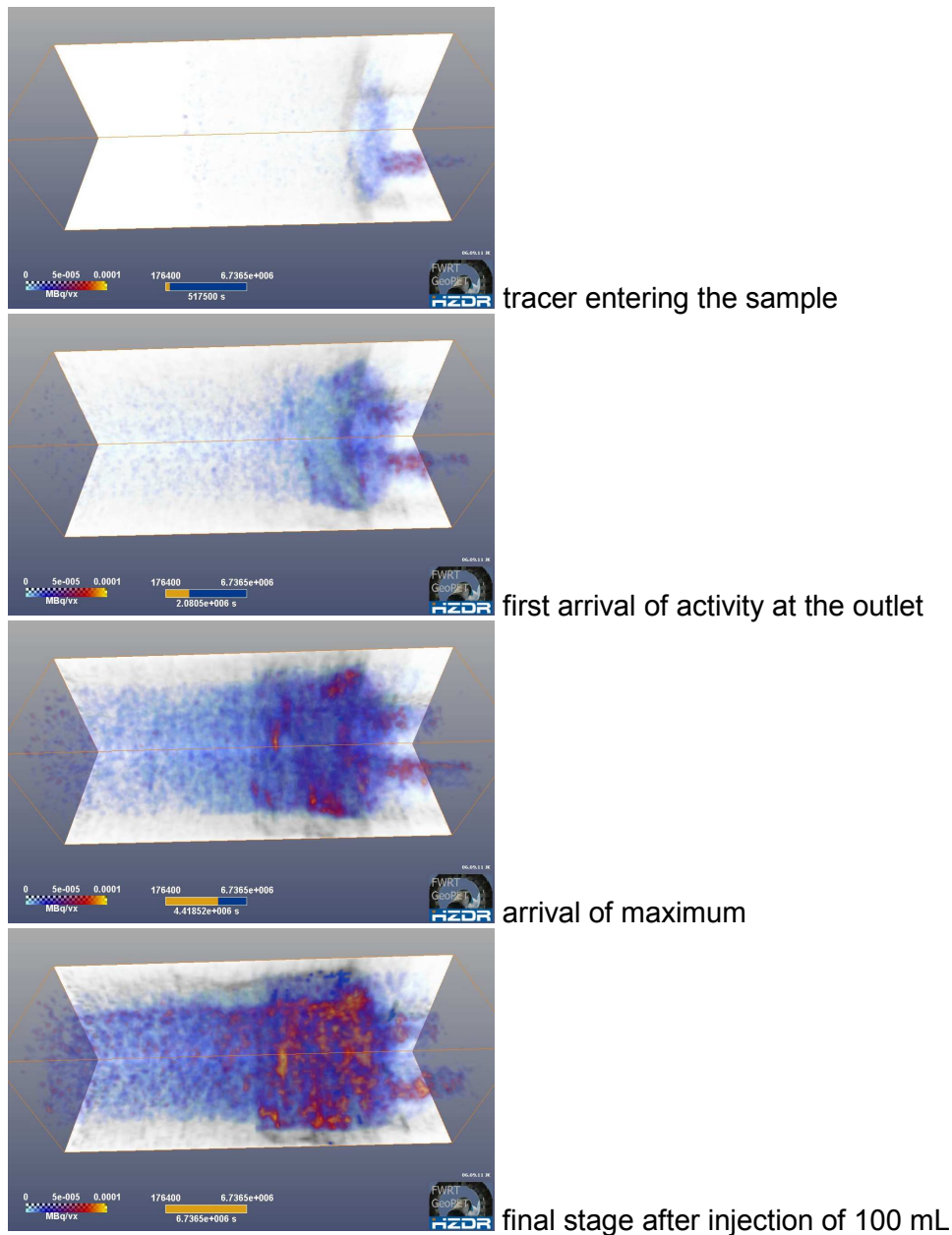


Figure 38. Transport of [^{58}Co]cobalt hexacyano complex as a conservative tracer in a sand-bentonite column. The images show a patchy and non-uniform tracer distribution.

3.5.2. Advection in rock cores

Äspö granite. X-ray computed microtomography (X- μ CT) and PET measurements were conducted with a granitic core from the hard rock laboratory Äspö (Fig. 39). Conservative tracers (F^- , I^-), marked with the positron-emitting radionuclides ^{18}F and ^{124}I , and Aldrich humic acid, labelled by complexation with ^{86}Y , were used as radiotracers to observe transport processes of both dissolved components and colloids in the crystalline matrix along a longitudinal fracture. Flow rates ranged from 0.1 to 0.001 mL min^{-1} . The volume of the tracer pulse was always 5 mL.

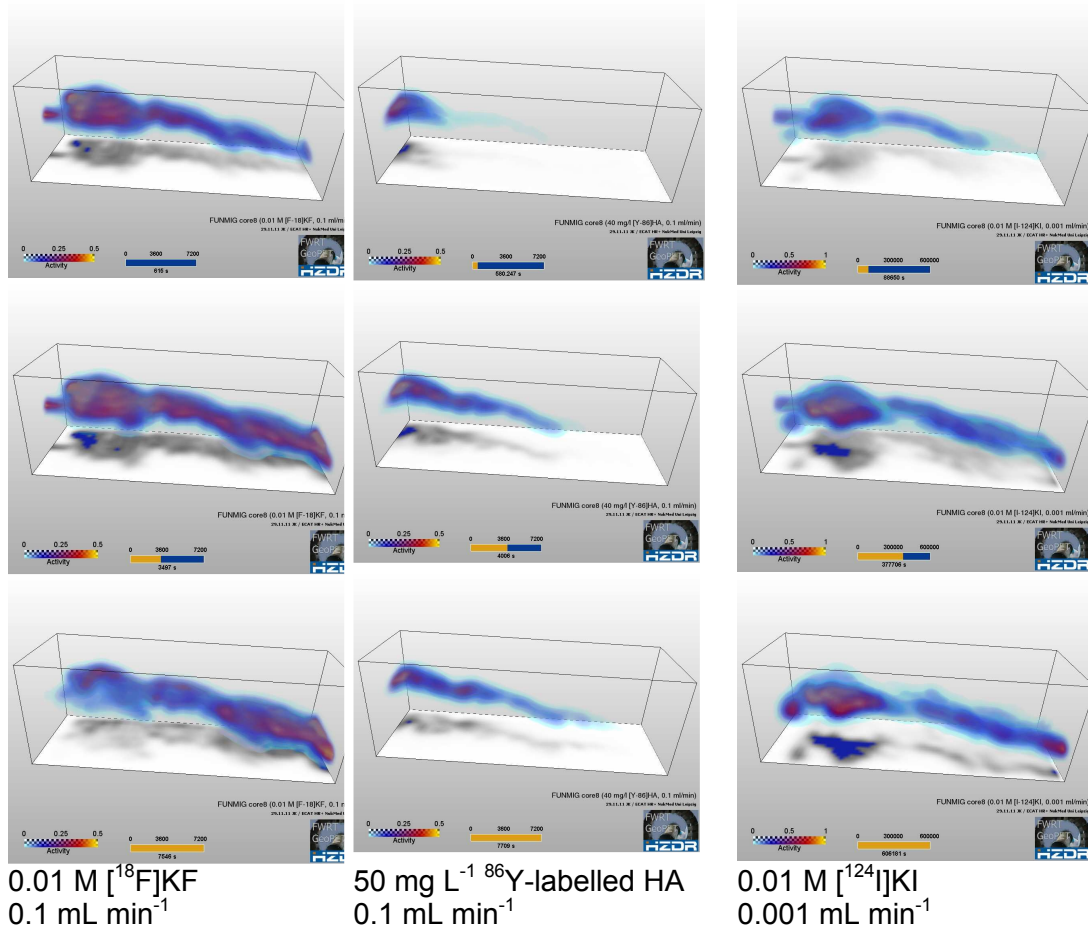


Figure 39. Transport of fluoride, HA and iodide in the granite core Äspö8. The images were taken for comparable injection volumes. The injection flow rate for iodide was considerably slower than those for the other tracers.

These experiments were performed with a medical PET scanner ECAT Exact HR+ (Siemens, Germany) at the clinic and polyclinic for Nuclear Medicine, University of Leipzig. The spatial resolution of this scanner is ~ 5 mm, which is far beyond the aperture of the fracture. Nevertheless, the characteristics of the transport processes are significant: In all cases, the flow path is strongly localised, with some zones of stronger “accumulation” of activity. Probably, these are zones with lower flow velocity, where the specific activity (per volume) attains higher values than in zones with short times of residence. The measurements with fluoride and with HA were conducted at the same flow rate. The transport of the HA is more localised to one tortuous line and is strongly delayed compared to fluoride. The pulse did not arrive at the outlet during the experiment. The activity distribution of iodide, which was injected at a much lower flow rate, is similar to the activity distribution of fluoride for a comparable injected volume. However, the transport path of iodide appears to be more localised and less diffuse than that of fluoride. This effect is not related to imaging issues since additional gamma lines of ¹²⁴I should cause more noise and thus more diffuse images. Obviously, the higher kinetic energy due to the higher flow rate causes a stronger dispersion effect within the fracture.

The general behaviour – localised flow paths and local tracer accumulations – was reproduced by Lattice-Boltzmann simulations based on the segmented image of the

fracture (Fig. 40). These simulations were conducted at the University of Mainz, Institute of Geosciences.

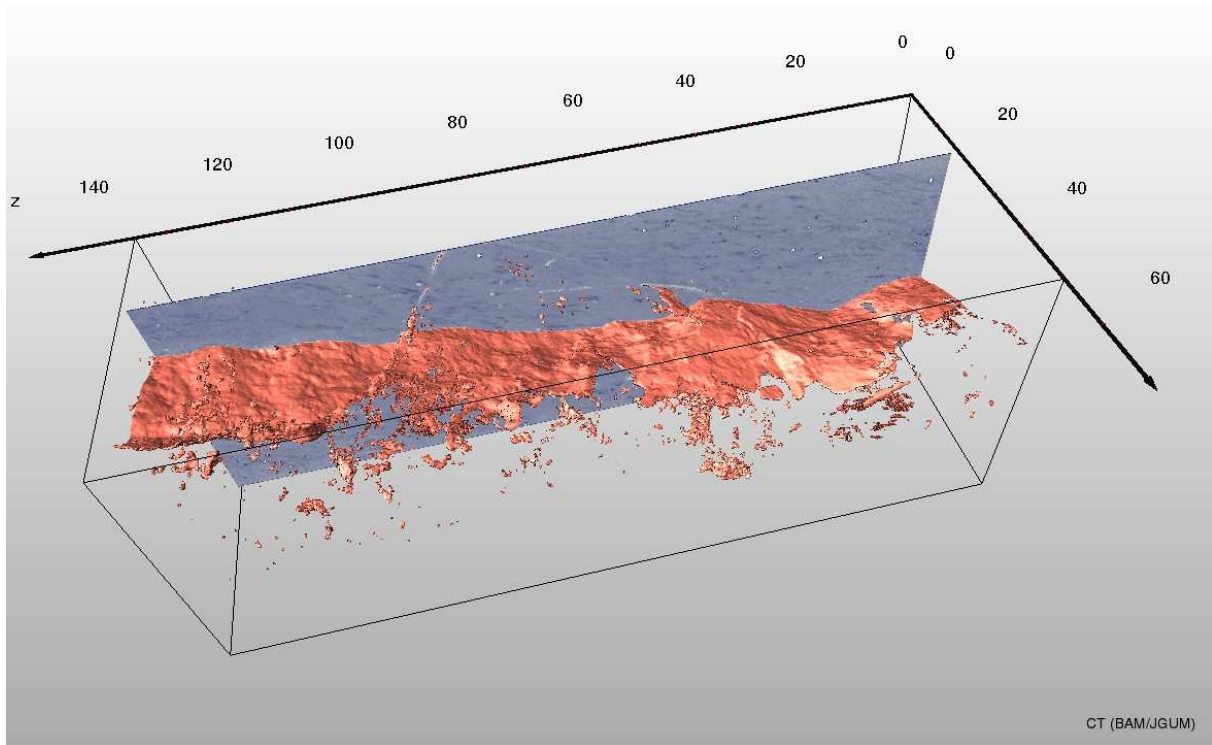
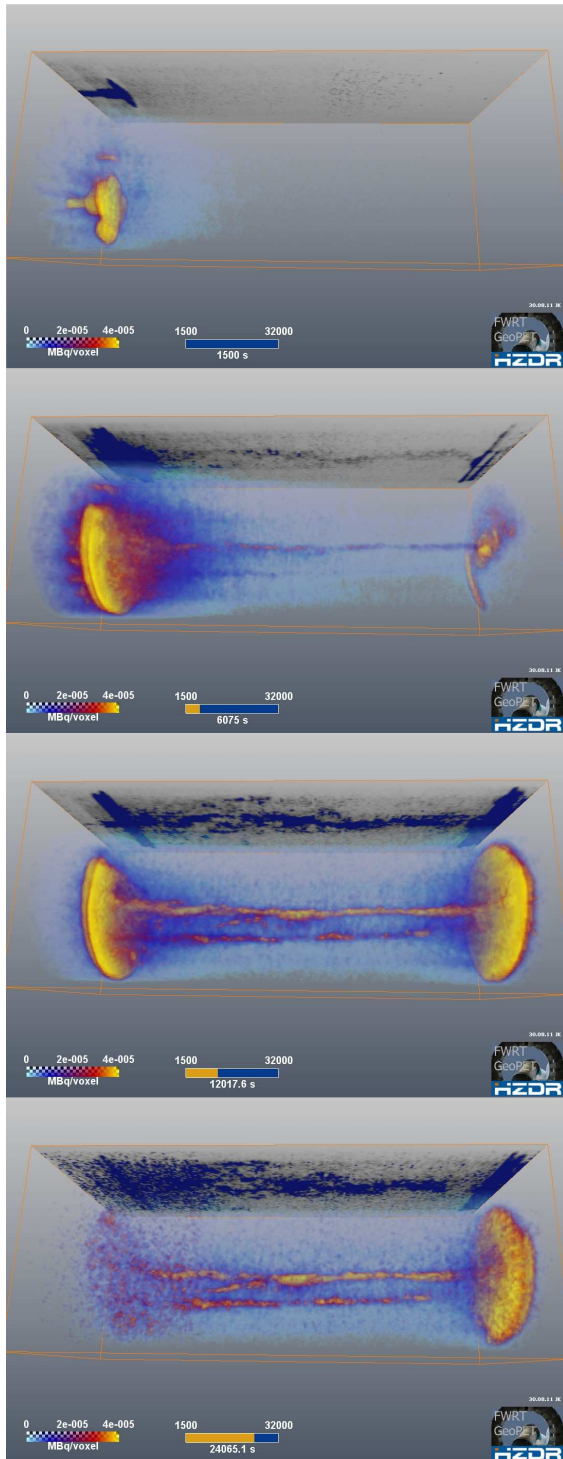


Figure 40. Projection of the X- μ CT image (produced by BAM, Berlin, processed by the Institute of Geosciences, University of Mainz), with the segmented fracture.

Grimsel granite Nagra2. A granite core from a fracture zone of the Grimsel test site was provided by Nagra (Switzerland) for flow experiments with PET monitoring. The test procedure was similar to the experiments with the Äspö sample, but now conducted with the higher-resolving ClearPET in our laboratories, which allowed a considerably longer observation period. 24 images have been recorded during the injection of 0.001 M [^{18}F]KF in synthetic Grimsel water over 12 hours at a flow rate of 0.1 mL min $^{-1}$ (Fig. 41).



25 min, $V = 1.5$ mL

100 min, $V = 9$ mL (5 mL tracer solution and 4 mL carrier solution)
 first appearance of the tracer at the outlet after 120 min

200 min, $V = 17$ mL

400 min, $V = 34$ mL
 maximum activity at the outlet after ~ 450 min

Figure 41. PET monitoring of the flow in the axially fractured Grimsel granite core Nagra2, flow rate 0.1 mL min^{-1} , Grimsel water with ^{18}F , tracer pulse length 5 mL.

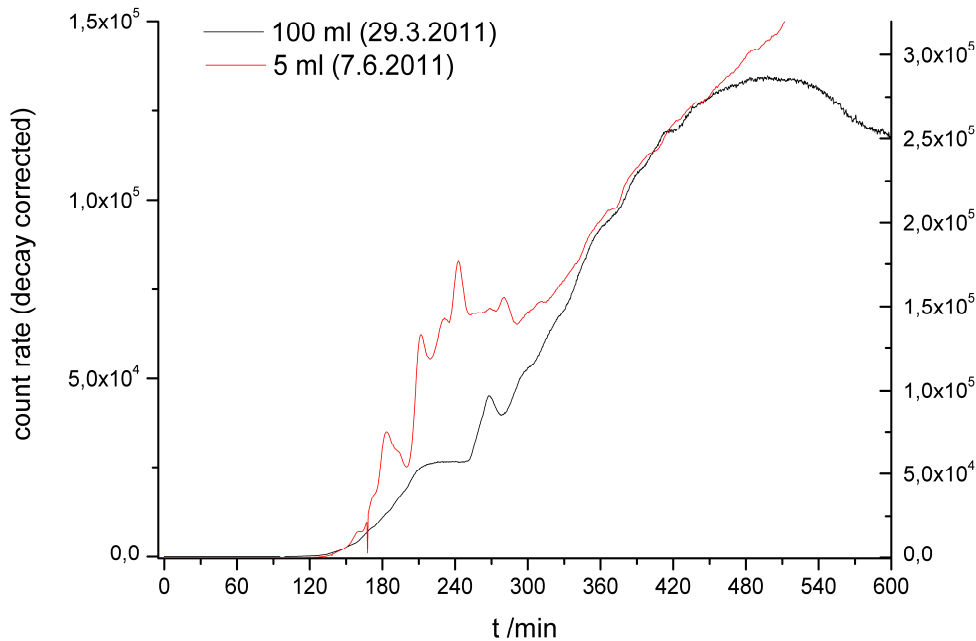


Figure 42. Break-through curves for the sample Nagra2 for two different tracer pulse lengths (red: 5 mL, black: 100 mL). Decay-corrected count rate measured by means of the flow-through counter “GABI” (Raytest, Germany).

With ClearPET, the resolution is close to the order of the maximum fracture aperture of 0.5 mm - 3 mm. However, two distinct pathways, passed with different velocities, are clearly discernable. The fast central pathway was quickly passed within ~ 20 min. Therefore, the temporal variations during the break-through were not resolved. For technical reasons, the inlet into the sample is equipped with a sintered glass filter plate (pore size 1 μ m), which causes accumulation of the tracer in this zone and temporal smoothing of the input pulse. This is the reason for much longer apparent residence times observed in the break-through curves recorded at the outlet (Fig. 42).

The tracer at inlet and outlet causes background gradients of scattered radiation which appear as activity clouds near the end planes. A scatter correction of the PET data would considerably reduce this effect. An appropriate method for high scatter fractions is in development, but not yet applicable. In the zones with low background, the benefit of the higher resolution compared to the medical scanner is obvious. Features of the tortuous flow path are now observable.

3.5.3. Diffusion

Grimsel granite Febex1. This Grimsel granite core originates from the FEBEX experiment (FUN05-001, 5.18m). An axial blind hole was drilled into a section of the core, which appeared to be intact. The end plane was sealed, leaving a port connecting the hole to a fluid injection pump. All other surfaces of the sample were open to atmosphere. In a first step, the borehole was filled with 0.01 M $[^{18}\text{F}]\text{KF}$. Carrier solution was then injected at a flow rate of 0.02 mL min^{-1} . 15 PET images were recorded during the experiment. These measurements were carried out with the partially equipped ClearPET scanner, yielding lower image quality.

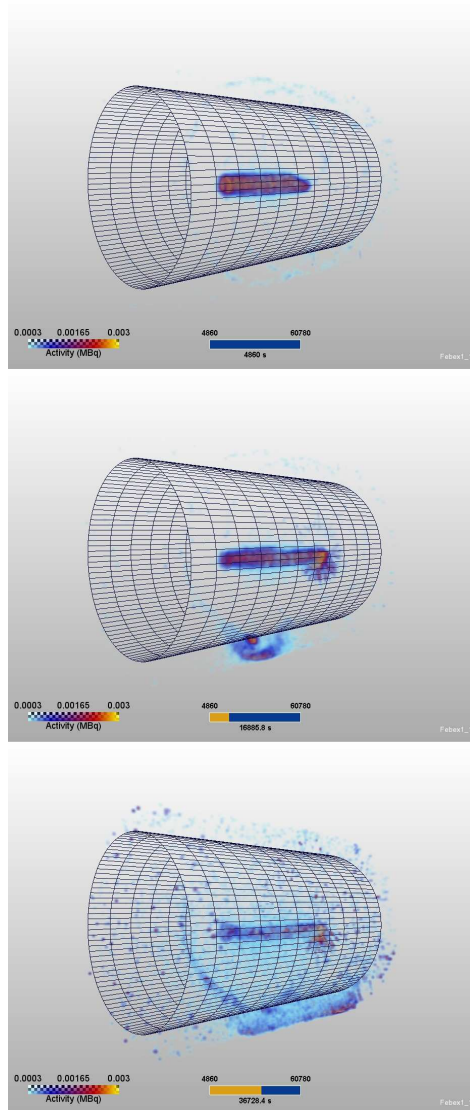


Figure 43. PET images taken during injection of $[^{18}\text{F}]\text{KF}$ solution into Grimsel granite, sample Febex1. The tracer was filled into an axial blind hole, followed by injection of carrier solution.

The images (Fig. 43) are noisy, which is caused by the limited number of detectors. However, the central source was initially clearly visible. No effect of the injection was observable at the beginning, apart from the decrease in activity in the borehole due to dilution. After about 2 hours, the images showed activity appearing as a ring on the shell of the cylinder. Later on, seepage of fluid through a fracture became obvious. This effect – clearly visible source and sink, but no detectable activity between – was frequently observed in following experiments. It is due to the fact that activity below the local background radiation cannot be detected. This local background depends on the general background, but also on the fraction of scattered radiation and thus on the experimental conditions.

Another experiment was conducted with ^{124}I in synthetic Grimsel water. The “labelled fluid” was filled into the blind hole. Then, the sample was left to stand for 20 days without external driving pressure, wrapped in aluminum foil.

This test (Fig. 44) showed diffusional spreading of the tracer into the sample. Here, no direct loss through the fracture was observed. The tracer gradually “vanishes” under the background level. This level is rather high because the partially equipped scanner was applied. Furthermore, ^{124}I emits additional gamma radiation in the sensitive energy range. Nonetheless, these results were promising in that they indicated the feasibility of spatially resolved diffusion experiments. Applying the fully extended scanner and higher specific activity (reduction of the borehole volume) would certainly yield improved images.

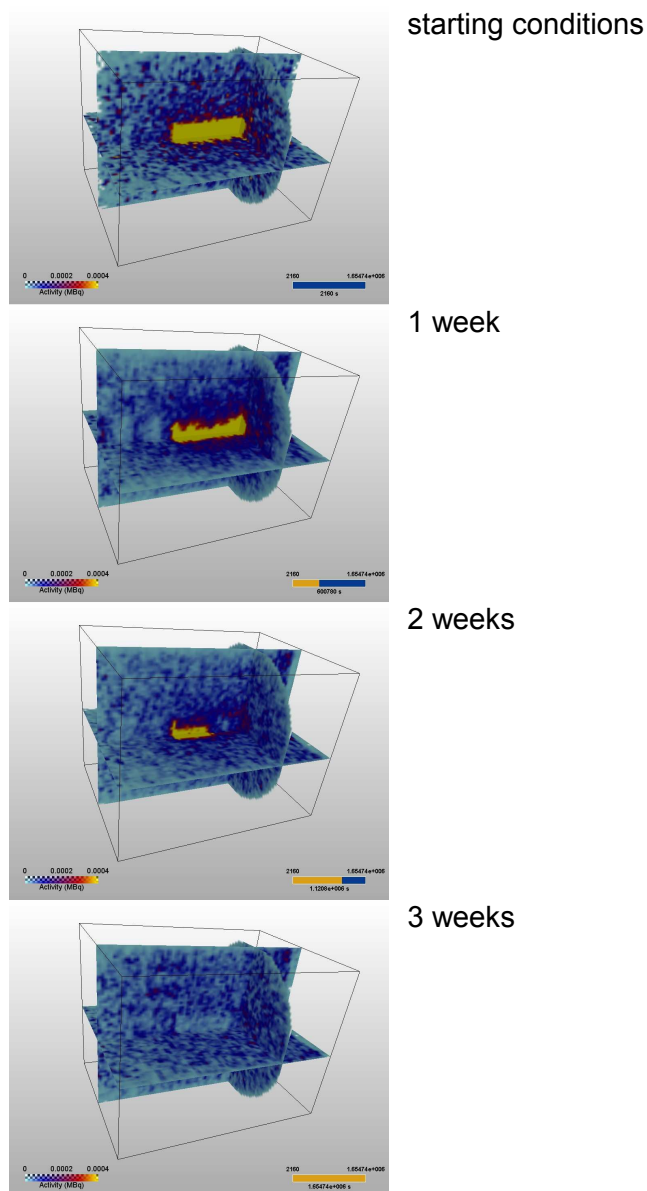


Figure 44. Diffusion of 0.001 M ^{124}I NaI in the fractured Grimsel granite core Febex1, starting from an axial blind hole.

Opalinus clay core OPA2. This sample is an intact clay core. It was completely cast into resin, leaving a central circular gap (thickness 0.1 mm, diameter 50 mm) for fluid injection. Synthetic Opalinus clay pore water with ^{124}I as a tracer was injected at a flow rate of $0.006 \text{ mL min}^{-1}$. 1 mL of “labelled fluid” ($0.001 \text{ M } [^{124}\text{I}]\text{I}^-$ in synthetic pore water, 75 MBq) were injected, followed by 20 mL of carrier solution. The pressure was steadily increasing up to 1 MPa, but no fluid appeared at the outlet. 24 images were recorded during this injection phase (Fig. 45).

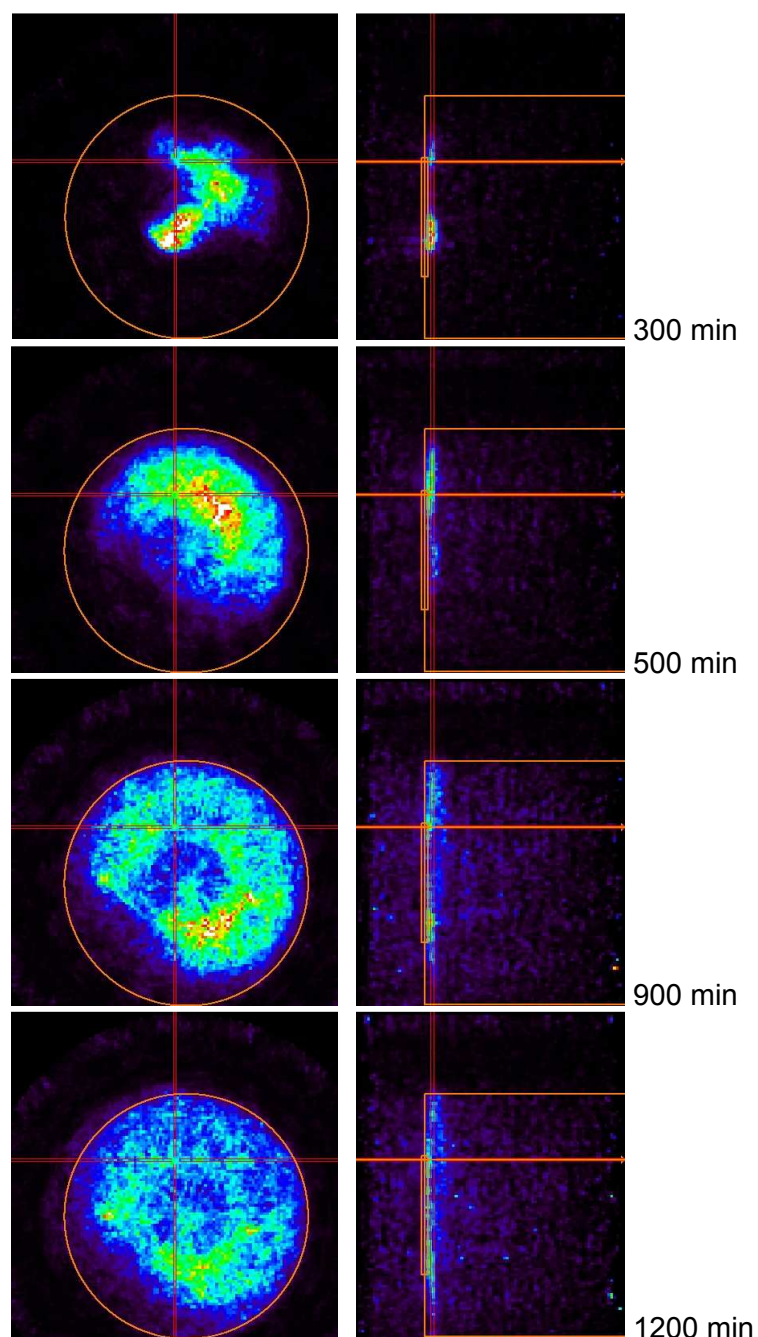


Figure 44. PET images of the OPA2 sample taken during injection of $[^{124}\text{I}]\text{I}^-$ in pore water. Left: radial slice, right: vertical slice at the position of the red lines, orange: geometry of the sample and the injection zone (without decay correction).

The images in Fig. 45 show that the tracer migrates from the injection gap into the slit between resin and rock material. The image after 300 min represents the termination of the tracer pulse. After that, the carrier solution flushes the injection gap, while the tracer migrates through distinct zones into the sample.

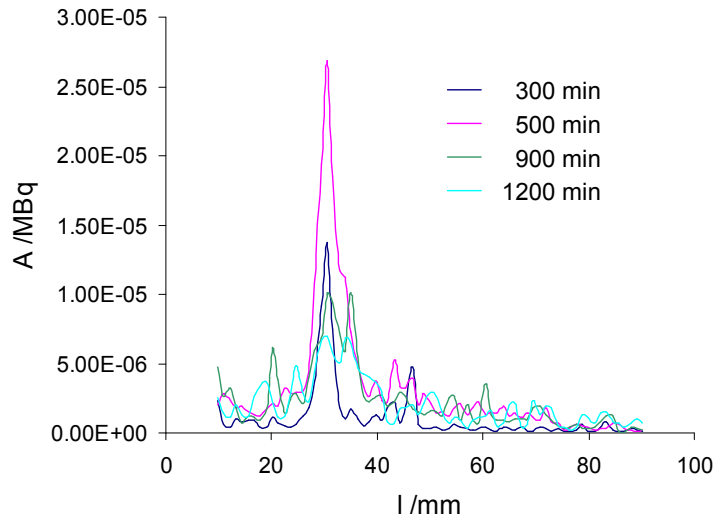


Figure 46. Activity profile along the paraxial line in Fig. 45 (without decay correction).

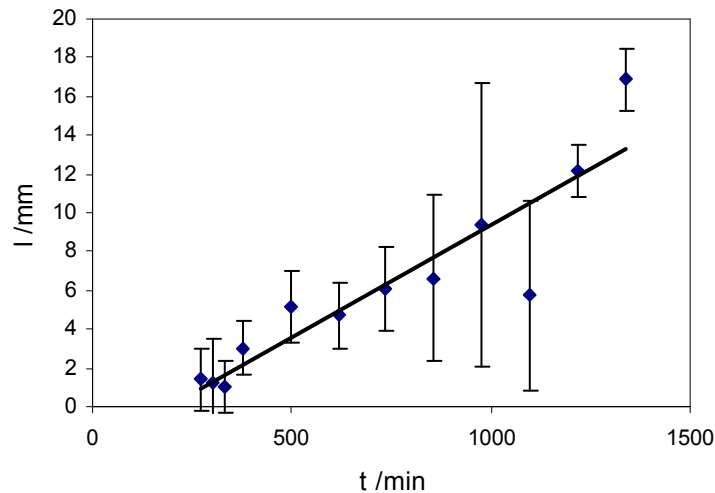


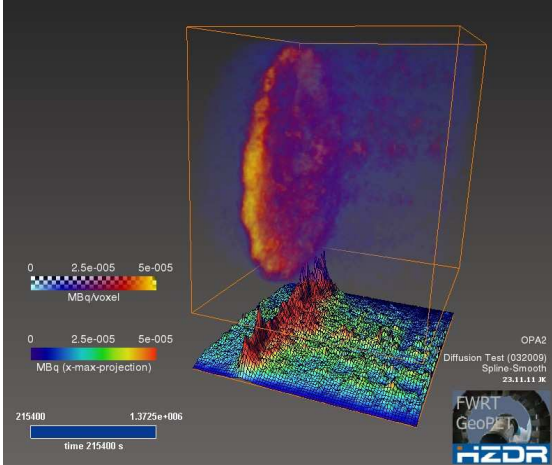
Figure 47. Spatial FWHM of the peak zone (20 mm - 45 mm) in Fig. 46.

Fig. 46 shows one paraxial profile of a zone with high activity. The left side of the peak is determined by the end plate, and the right flank is slowly moving into the material. A Gauss fit to the peaks for each time step yields the spatial FWHM (Fig. 47), from which we determined a local velocity of $(0.72 \pm 0.08) \text{ mm h}^{-1}$.

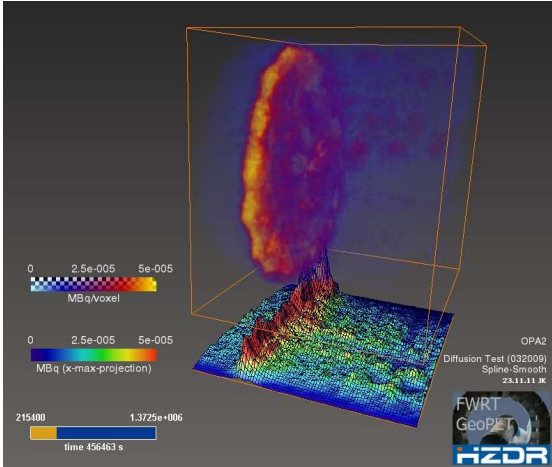
Here, we have to consider irregular conditions because the increasing pressure shows that either the sample contained air which was increasingly compressed, or reactions between pore water and rock material occurred and caused clogging of pathways.

Principally, this method allows deriving local velocities and their distribution on the millimeter scale in media with extremely low permeability, where (within reasonable time frames) the tracer enters only into a thin layer in the millimeter range. This example thus demonstrates that ultra-low fluid permeabilities together with the velocity distribution can be determined from time-dependent PET observations as a non-destructive method.

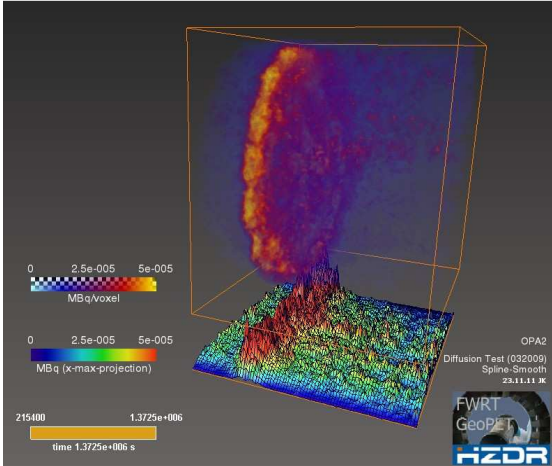
After reaching the threshold pressure of 1 MPa, the pump was stopped, and the evolution of the tracer distribution – driven by diffusion only – was recorded during the decay period of the tracer over 14 days (Fig. 48).



start of diffusion after 2.5 d



5.3 d



15.8 d

Figure 48. Diffusion of $[^{124}\text{I}]^-$ in OPA2 after the injection period (see Fig. 46).

No significant changes in the point-wise tracer distribution were observable during this diffusion period of 2 weeks. Nevertheless, the slice-wise integral (projection at the bottom of the images in Fig. 48) was slightly broadening with time. The total progress of the “diffusion front” was in the order of 1 mm in 14 days (0.07 mm d^{-1}), i.e., below the resolution of the PET scanner. Obviously, longer observation periods are required in Opalinus clay in order to derive parameters.

Opalinus clay cores BLT13/7. Samples were prepared from an Opalinus clay core (drill hole BLT13/7). The core samples (diameter 10 cm) had been shrink-wrapped after drilling and then stored. They were cut into 8 cm long sections. Immediately after cutting, the samples were impregnated with epoxy and then completely cast in epoxy resin. An axial blind drill hole (diameter 5 mm, depth 50 mm, volume 1 mL) was drilled into the samples and then charged with synthetic Opalinus clay pore water. The bore was provided with a closing screw.

It was found that the fluid was rapidly sucked into the sample bulk volume. Over a period of 3 months, about 30 mL of solution had to be added until the fluid level apparently stabilised. After this resaturation period, the holes were cleaned and filled with $0.001 \text{ M } [^{124}\text{I}]\text{KI}$ in synthetic Opalinus clay pore water. The samples were stored at 20°C or 50°C , and about 10 PET images were taken until the activity of the tracer decayed below the detection threshold (Figs. 49 and 50). This threshold depends on the specific activity and thus on the tracer distribution.

After 10 days, the tracer in the samples stored at 50°C had spread over the complete sample and fell below the detection threshold (Fig. 50). The tracer distribution in the samples stored at 20°C did not reach this uniform distribution before decay below the threshold.

In principle, the evolution of the tracer distribution could be fitted to the 2D-circular solution of the diffusion equation in order to derive a diffusion coefficient for Γ . However, we clearly observe 3D-anisotropy. Therefore, the assumptions of this equation are not valid. Instead, a 3D-FEM analysis is currently being conducted with the COMSOL Multiphysics optimisation module, aiming at the derivation of an apparent diffusion tensor [68].

Fig. 49 shows that the fluid was again lost into the bulk volume during the tracer test. Obviously, the spreading is by far too fast to be caused by molecular diffusion, and the loss of water indicates that suction causes advective transport.

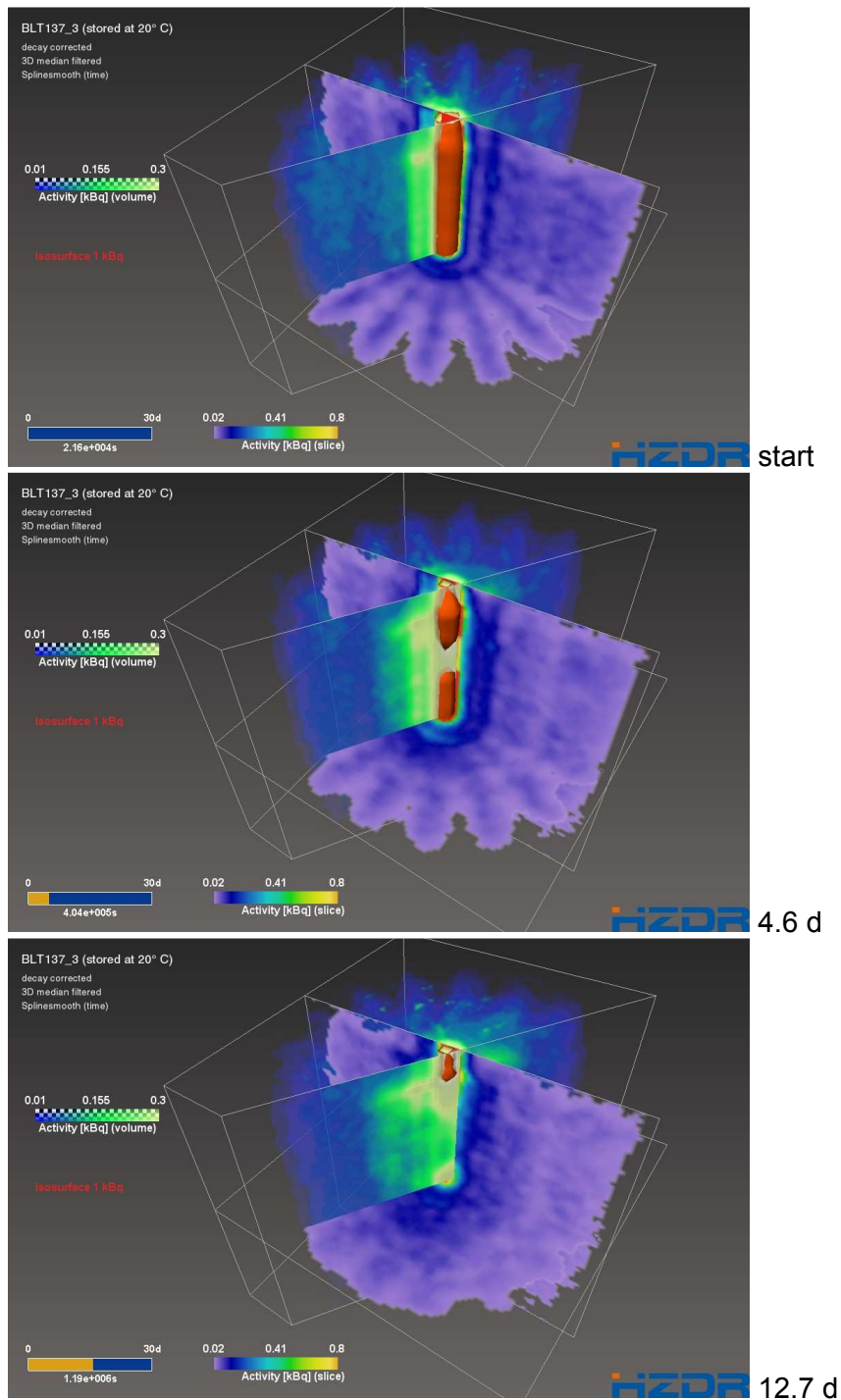


Figure 49. Diffusion of $[^{124}\text{I}]^-$ from an axial line source in Opalinus clay (BLT13/7) at 20°C. The red isosurface marks the maximum of the tracer distribution, where labelled fluid is present. The reduced activity at the center is caused by the formation of an air bubble, and after 20 days, the drill hole was nearly dry.

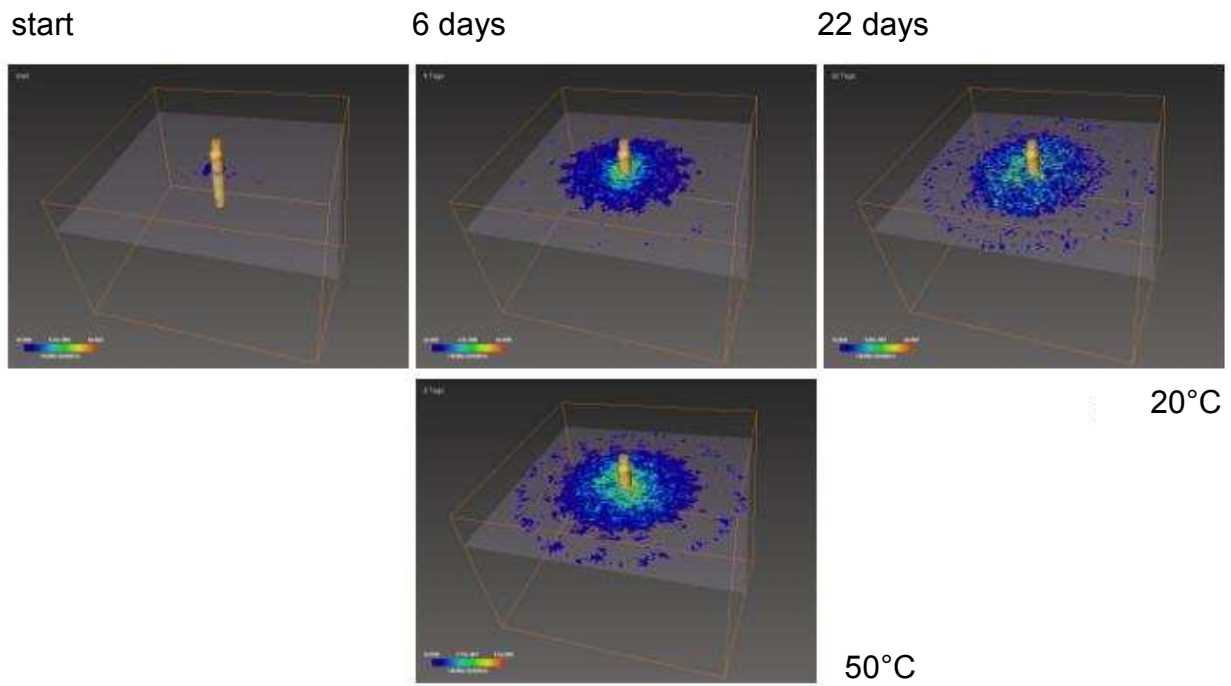


Figure 50. Diffusion in Opalinus clay (BLT13/7) from an axial line source (yellow surface). The samples were stored at 20°C (upper row) or 50°C (lower image).

The most meaningful zone for evaluating the diffusion process is far away from the source and therefore always near the noise level. This noise level is caused to a large extent by scattered events, which also produce blurring with similar characteristics like tracer diffusion. In order to identify these scatter characteristics, and – if possible – to filter or correct scattered events, we conducted Monte Carlo simulations with OpenGATE (see Fig. 7). The scatter fraction was determined with these simulations to be as high as 75%. Simulation results in comparison with measured images are shown in Fig. 51. It is obvious that the deceptive cloud of apparent activity around the source, as well as star-shaped and circular artifacts, are produced by scattered events, which are projected by the STIR OSMAPOS algorithm into low-sensitivity zones near the source of scatter. It is possible, and currently under progress, to develop a scatter correction algorithm that is based on OpenGATE simulations of the experimental conditions.

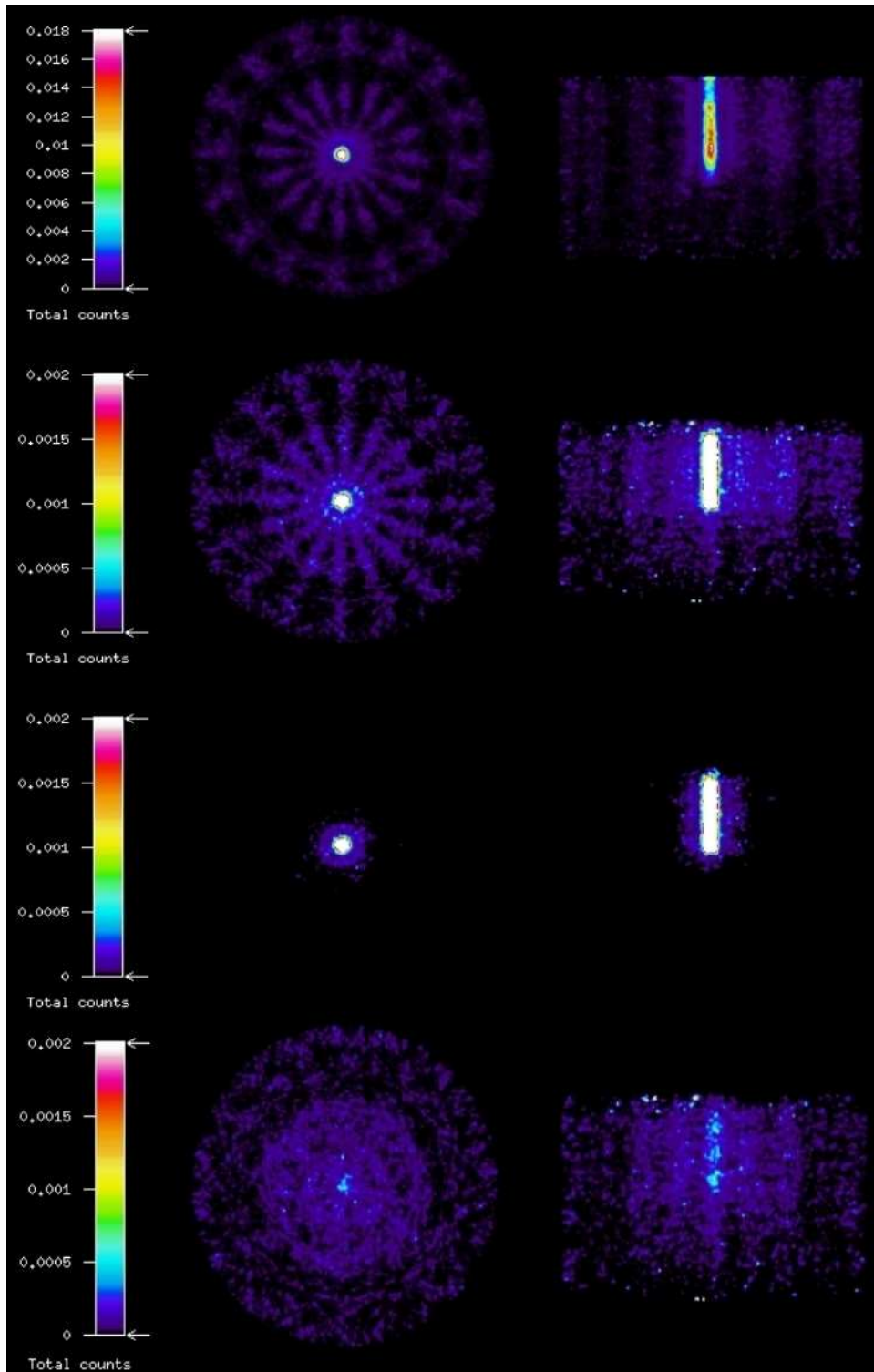


Figure 51. Reconstructions of measured and simulated results for the initial conditions (line source in Opalinus clay) of the experiment with BLT13/7 (see Fig. 48). Left: transaxial (x-y) views, right: vertical (x-z) cross sections. Images in the topmost row represent the measured image. Images in the second row are based on all coincidences (true and scattered) from the respective simulation. The images in the third row represent the reconstruction of the simulated true coincidences without scattered events. The bottom row of images represents the reconstruction based only on the simulated scattered coincidences.

Halite test samples. Two halite test samples (half-cylinders, diameter 10 cm, thickness 5 cm) from the Staßfurt region (Saxony-Anhalt, Germany) were furnished with radial blind holes (diameter 5 mm, depth 3 cm). One sample was charged with synthetic Q-solution, according to the formation fluid, the other one with 50% diluted Q-solution, according to the water in the hanging wall of the salt formation (Buntsandstein). The solutions have been “labelled” with ^{124}I . The holes were closed, and the samples were scanned for 19 days (Fig. 52). During this period, no changes could be observed in the images.

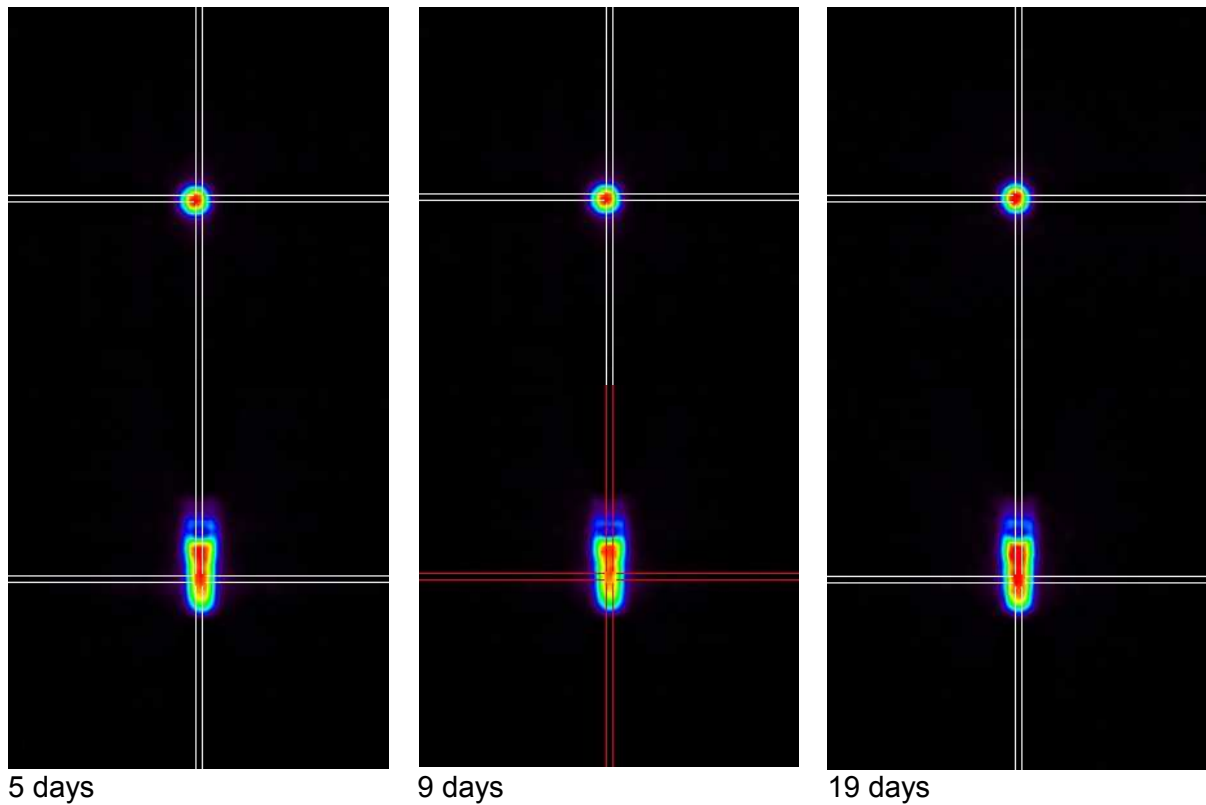


Figure 52. Diffusion test with $[^{124}\text{I}]\text{NaI}$ in Q-solution for a halite sample. No movement was to be observed during 19 days.

4. Conclusions and outlook

In terms of sorption properties, clay barriers are known to be superior to other possible host formations for a final repository. In the event of pH drops, however, release of contaminant metals is to be expected. Humic-bound transport would deteriorate the situation, but the investigations within this project have shown that metal adsorption onto clay materials is increased by the presence of humic matter throughout the acidic pH range. Surprisingly, similar results were also obtained for propionic acid and lactic acid as representatives of low-molecular-weight organic matter, which is most abundant in natural clay material. It appears that a mobilisation of metals in consequence of acidification is generally counteracted by organic complexants in clay systems.

Although the general trends of the effect of humic acid can be explained by the pH dependences of metal-humate complexation and humic acid adsorption, quantitative estimates by means of the linear additive model did not reproduce the experimental data. Most likely, this may be ascribed to selectivities in complexation and adsorption within the polydisperse system of humic molecules. Studies with fractionated humic material might be helpful to substantiate this reasoning. Identifying the criteria for the applicability of the linear additive model is of fundamental importance since this approach is implicit in most conceptual models that consider humic-bound transport. The assumption must be verified for every individual system under consideration.

As another prerequisite for transport modelling, adsorption of humic matter must be reversible because a dynamic process is assumed. In this respect, our studies led to different results. On the one hand, it was found that humic and fulvic acids cannot be desorbed from kaolinite on dilution. By tracer exchange experiments with ^{14}C -labelled materials, however, it could be demonstrated for the first time that a dynamic equilibrium exists, albeit the exchange process takes much more time than the adsorption process at the bare surface (more than one month compared to several hours for fulvic acid). Consequently, in order to assess whether a steady equilibrium can be maintained in flow systems, the kinetics of adsorption is certainly not a valid criterion.

Furthermore, kinetic effects must be considered that lead to an increasing inertness of metal-humic complexes. These stabilisation processes also affect competitive reactions. In complexation studies with purified humic substances, equilibration times must be long enough to cover these phenomena, which occur on different time scales. A fundamental understanding of the molecular processes involved is indispensable. This project significantly contributed to gaining more insight in this respect. The wide-spread notion that humic-bound metals undergo an in-diffusion process, moving from weak peripheral sites to strong internal sites, turned out to be inapplicable. A delayed degradation of polynuclear species in touch with humic colloids does not occur in general. An on-site stabilisation is most probable, even though spectroscopic evidence was only obtained for instantaneous structural rearrangements induced by bound metals. Subsequent changes on the time scale of the kinetic effect can only be minor. Nonetheless, in view of these ageing processes, the reversibility of metal-humate complexation needs to be examined in more detail. Tracer exchange studies, performed in a similar way as was done with the adsorption systems, appear to be a promising approach.

The ClearPET scanner is a relatively new instrument, utilised for geoscientific applications during the project period. Therefore, the results of the PET studies are provisional to some extent. Significant improvements of the images are expected from enhanced and new reconstruction codes. Error analysis will be possible with the establishment of MC simulations.

Nevertheless, the impact of rock structure on transport phenomena could be clearly shown. Up to now, all our studies on rock cores with real structure showed strong deviations from homogeneity. In contrast, the samples compacted from suspensions showed a widely homogeneous transport, which could be conveniently fitted with a one-dimensional CXTFIT model. However, the homogeneously compacted sample Nagra1 (sand-bentonite) shows considerable radial variations in the tracer concentration, probably due to the general difficulty of preparing homogeneous large-diameter specimen from moist clay powder. Even the sample OPA1 shows deviations from laterally homogeneous flow, but to a minor extent.

Therefore, our working hypothesis is that homogeneous transport is an idealised notion, which may be convenient for simplified models, but which is rarely realised. One of the aims of studies on heterogeneous transport is the transformation of parameters determined in batch experiments to the conditions of real, consolidated material. In most cases, effective parameters for volume and active surface area have to be anticipated, which reflect the heterogeneous response of the medium to the process, and which can be considerably smaller than the total quantities. Such effective parameters can be derived from usual break-through curves. However, only methods for spatially resolved process observation give insight into the causes of reduced efficiencies in the pore space.

We observed some untypical tracer spreading in Opalinus clay, together with a loss of fluid into the sample. This spreading is too fast to be caused by pure molecular diffusion [69, 70]. We had to suppose that the sample was only partially saturated with water, which caused suction into small pores. This was due to damage and alteration of the cores during recovery and storage. Similar effects have been reported in Refs. [71-73]. Such processes are, however, also relevant to real scenarios; they are likely to occur in excavation damaged zones as well, and therefore deserve further attention.

Such fast spreading did not occur in rock salt, although these samples contained visible fractures. In the recently finished project 02C1536, it could be shown that two different styles of propagation of conservative tracers occur in salt rocks. If the distribution in the medium is finely dispersed, we often observe disappearance of the tracer between inlet and outlet as the activity falls below the detection threshold, or we find an effuse, not necessarily homogeneous tracer cloud. However, in some cases, the tracer concentration over larger ranges may be derived as integral value. This propagation style presumably occurs in dense, fine-pored material. In fractured matrices, soils and macroporous material, we frequently observed strongly localised transport pathways. Here, we were able to align PET experiments with X- μ CT-based Lattice-Boltzmann simulations. We found accordance in the major structure, but additional transport pathways were visible in the PET image which could not be segmented in the X- μ CT image.

Strong localisation was also present in crystalline rocks that were investigated in the framework of this project. The fractured samples showed distinct flow paths on the fracture plane, not a diffuse cloud that filled the complete fracture volume. Thus, the effective transport volume is limited to these restricted pathways. Consequently, retarding interactions of contaminants will be limited to this reduced internal surface area. In spite of this zoning, humic acid as a potential carrier was strongly retarded in the granite core from Äspö.

In summary, all tracer propagation processes that we made visible by the PET method turned out to be more complex than anticipated. Simple models that describe the influence of the bulk material on the basis of 2 or 3 parameters (e.g., porosity, internal surface area) probably overestimate the retention, i.e., they underestimate the transport velocity. Instead, process-dependent parameters must be adopted.

5. References

- [1] Lieser, K.H., Ament, A., Hill, R., Singh, R.N., Stingl, U., Thybusch, B., *Radiochim. Acta* 49 (1990) 83-100.
- [2] Dearlove, J.P.L., Longworth, G., Ivanovich, M., Kim, J.I., Delakowitz, B., Zeh, P., *Radiochim. Acta* 52/53 (1991) 83-89.
- [3] Kim, J.I., Zeh, P., Delakowitz, B., *Radiochim. Acta* 58/59 (1992) 147-154.
- [4] Choppin, G.R., *Radiochim. Acta* 58/59 (1992) 113-120.
- [5] Liu, J., Lippold, H., Wang, J., Lippmann-Pipke, J., Chen, Y.H., *Chemosphere* 82 (2011) 866-871.
- [6] Liu, J., Wang, J., Chen, Y.H., Lippold, H., Lippmann-Pipke, J., *J. Environ. Sci.-China* 22 (2010) 1695-1702.
- [7] Zachara, J.M., Resch, C.T., Smith, S.C., *Geochim. Cosmochim. Acta* 58 (1994) 553-566.
- [8] Samadfam, M., Sato, S., Ohashi, H., *Radiochim. Acta* 82 (1998) 361-365.
- [9] Lippold, H., Lippmann-Pipke, J., *J. Contam. Hydrol.* 109 (2009) 40-48.
- [10] Cacheris, W.P., Choppin, G.R., *Radiochim. Acta* 42 (1987) 185-190.
- [11] Choppin, G.R., Clark, S.B., *Mar. Chem.* 36 (1991) 27-38.
- [12] Rao, L., Choppin, G.R., Clark, S.B., *Radiochim. Acta* 66/67 (1994) 141-147.
- [13] King, S.J., Warwick, P., Hall, A., Bryan, N.D., *Phys. Chem. Chem. Phys.* 3 (2001) 2080-2085.
- [14] Geckeis, H., Rabung, T., Ngo Manh, T., Kim, J.I., Beck, H.P., *Environ. Sci. Technol.* 36 (2002) 2946-2952.
- [15] Artinger, R., Kienzler, B., Schüßler, W., Kim, J.I., *J. Contam. Hydrol.* 35 (1998) 261-275.
- [16] Schüßler, W., Artinger, R., Kienzler, B., Kim, J.I., *Environ. Sci. Technol.* 34 (2000) 2608-2611.
- [17] Schüßler, W., Artinger, R., Kim, J.I., Bryan, N.D., Griffin, D., *J. Contam. Hydrol.* 47 (2001) 311-322.
- [18] Warwick, P.W., Hall, A., Pashley, V., Bryan, N.D., Griffin, D., *J. Contam. Hydrol.* 42 (2000) 19-34.
- [19] Bryan, N.D., Barlow, J., Warwick, P., Stephens, S., Higgo, J.J., Griffin, D., *J. Environ. Monit.* 7 (2005) 196-202.
- [20] Lippold, H., Eidner, S., Kumke, M.U., Lippmann-Pipke, J., *Appl. Geochem.* 27 (2012) 250-256.
- [21] Seibert, A., Mansel, A., Marquardt, C.M., Keller, H., Kratz, J.V., Trautmann, N., *Radiochim. Acta* 89 (2001) 505-510.
- [22] Wyllie, M.R.J., Rose, D., *Trans. AIME* 189 (1950) 105-118.
- [23] Lorenz, P.B., *Nature* 189 (1961) 386-387.
- [24] Shen, L., Chen, Z., *Chem. Eng. Sci.* 62 (2007) 3748-3755.
- [25] Richter, M., Gründig, M., Zieger, K., Seese, A., Sabri, O., *Radiochim. Acta* 93 (2005) 643-651.
- [26] Gründig, M., Richter, M., Seese, A., Sabri, O., *Appl. Geochem.* 22 (2007) 2334-2343.
- [27] Kulenkampff, J., Gründig, M., Richter, M., Enzmann, F., *Phys. Chem. Earth* 33 (2008) 937-942.
- [28] Aiken, G.R., in: Aiken, G.R., MacKnight, D.M., Wershaw, R.L., MacCarthy, P. (Eds.), "Humic substances in soil, sediment and water: geochemistry and isolation", Wiley-Interscience, New York 1985, pp. 363-385.
- [29] Stevenson, F.J., "Humus Chemistry. Genesis, Composition, Reactions", John Wiley and Sons, New York 1994.
- [30] Mansel, A., Kupsch, H., *Appl. Radiat. Isot.* 65 (2007) 793-797.
- [31] Fraker, P.J., Speck, J.C., *Biochem. Biophys. Res. Commun.* 80 (1978) 849-857.
- [32] Lund, T.J., Koretsky, C.M., Landry, C.J., Schaller, M.S., Das, S., *Geochem. Trans.* 9 (2008) 9.
- [33] Borden, D., Giese, R.F., *Clays Clay Min.* 49 (2001) 444-445.
- [34] Huertas, J.F., Chou, L., Wollast, R., *Geochim. Cosmochim. Acta* 62 (1998) 417-431.

- [35] Vejsada, J., Hradil, D., Řanda, Z., Jelínek, E., Štulík, K., *Appl. Clay Sci.* 30 (2005) 53-66.
- [36] Gonçalves, M.A., Figueiras, J., in: *Actas do VIII Congresso de Geoquímica dos Países de Língua Portuguesa, Aveiro (Portugal) 2005*, pp. 513-518.
- [37] Moronta, A., Ferrer, V., Quero, J., Arteaga, G., Choren, E., *Appl. Catal. A-Gen.* 230 (2002) 127-135.
- [38] Fan, M., Boonfueng, T., Xu, Y., Axe, L., Tyson, T.A., *J. Colloid Interface Sci.* 281 (2005) 39-48.
- [39] Summarising Report "Wechselwirkung und Transport von Actiniden im natürlichen Tongestein unter Berücksichtigung von Huminstoffen und Tonorganika", BMWi, 2012, in preparation.
- [40] Hiraide, M., Tillekeratne, S.P., Otsuka, K., Mizuike, A., *Anal. Chim. Acta* 172 (1985) 215-221.
- [41] Schubert, J., *J. Phys. Colloid. Chem.* 52 (1948) 340-350.
- [42] Levin, C.S., Hoffmann, E.J., *Phys. Med. Biol.* 44 (1999) 781-799.
- [43] Zaidi, H., Hasegawa, B., *J. Nuc. Med.* 44 (2003) 291-315.
- [44] Zakhnini, A., Kulenkampff, J., Sauerzapf, S., Pietrzyk, U., Lippmann-Pipke, J., *Comput. Geosci.* (2012), in preparation.
- [45] Auffray, E., Bruyndonckx, P., Devroede, O., Fedorov, A., Heinrichs, U., Korjik, M., Krieguer, M., Kuntner, C., Lartizien, C., Lecoq, P., Leonard, S., Morel, C., Mosset, J.B., Pedrini, C., Petrosyan, A.G., Pietrzyk, U., Rey, M., Saladino, S., Sappey-Marinié, D., Simon, L., Streun, M., Tavernier, S., Vieira, J.M., Ziemons, K., *Nucl. Inst. Meth. A* 527 (2004) 171-174.
- [46] Ziemons, K., Auffray, E., Barbier, R., Brandenburg, G., Bruyndonckx, P., Choi, Y., Christ, D., Costes, N., Declais, Y., Devroede, O., Dujardin, C., Fedorov, A., Heinrichs, U., Korjik, M., Krieguer, M., Kuntner, C., Largeron, G., Lartizien, C., Larue, H., Lecoq, P., Leonard, S., Marteau, J., Morel, C., Mosset, J.B., Parl, C., Pedrini, C., Petrosyan, A.G., Pietrzyk, U., Rey, M., Saladino, S., Sappey-Marinié, D., Simon, L., Streun, M., Tavernier, S., Vieira, J.M., *Nucl. Inst. Meth. A* 537 (2005) 307-311.
- [47] Sempere Roldan, P., Chereul, E., Dietzel, O., Magnier, L., Pautrot, C., Rbah, L., Sappey-Marinié, D., Wagner, A., Zimmer, L., Janier, M., Tarazona, V., Dietzel, G., *Nucl. Inst. Meth. A* 571 (2007) 498-501.
- [48] Thielemans, K., Mustafovic, S., Tsoumpas, C., IEEE Nuclear Science Symposium Conference Record, 2007, pp. 2174-2176.
- [49] Thielemans, K., <http://stir.sourceforge.net>.
- [50] Baddeley, A., Turner, R., *J. Stat. Softw.* 12 (2005) 1-42.
- [51] Berger, M.J., Hubbell, J.H., Seltzer, S.M., Chang, J., Coursey, J.S., Sukumar, R., Zucker, D.S., Olsen, K., <http://physics.nist.gov/xcom>.
- [52] Jan, S., Santin, G., Strul, D., Staelens, S., Assie, K., Autret, D., Avner, S., Barbier, R., Bardies, M., Bloomfield, P.M., Brasse, D., Breton, V., Bruyndonckx, P., Buvat, I., Chatziioannou, A.F., Choi, Y., Chung, Y.H., Comtat, C., Donnarieix, D., Ferrer, L., Glick, S.J., Groiselle, C.J., Guez, D., Honore, P.F., Kerhoas-Cavata, S., Kirov, A.S., Kohli, V., Koole, M., Krieguer, M., van der Laan, D.J., Lamare, F., Largeron, G., Lartizien, C., Lazaro, D., Maas, M.C., Maigne, L., Mayet, F., Melot, F., Merheb, C., Pennacchio, E., Perez, J., Pietrzyk, U., Rannou, F.R., Rey, M., Schaart, D.R., Schmidlein, C.R., Simon, L., Song, T.Y., Vieira, J.M., Visvikis, D., Van de Walle, R., Wieers, E., Morel, C., *Phys. Med. Biol.* 49 (2004) 4543-4561.
- [53] Weber, S., Morel, C., Simon, L., Krieguer, M., Rey, M., Gundlich, B., Khodaverdi, M., *Nucl. Inst. Meth. A* 569 (2006) 381-385.
- [54] <http://www.r-project.org>.
- [55] Toride, N., Leij, F.J., van Genuchten, M.T., Research Report 137, US Salinity Laboratory, USDA, ARS, 1999.
- [56] Paulenová, A., Rajec, P., Kandráč, J., Sasköiová, G., Tothóvová, E., Bartoš, P., Švec, V., Góra, R., *J. Radioanal. Nucl. Ch.* 246 (2000) 617-622.
- [57] Zhou, Q., Maurice, P.A., Cabaniss, S.E., *Geochim. Cosmochim. Acta* 65 (2001) 803-812.

- [58] Hur, J., Schlautman, M.A., *J. Colloid Interface Sci.* 264 (2003) 313-321.
- [59] Reiller, P., Amekraz, B., Moulin, C., *Environ. Sci. Technol.* 40 (2006) 2235-2241.
- [60] Lakshman, S., Mills, R., Patterson, H., Cronan, C., *Anal. Chim. Acta* 282 (1993) 101-108.
- [61] Tanaka, T., Nagao, S., Sakamoto, Y., Ohnuki, T., Ni, S., Senoo, M., *J. Nucl. Sci. Technol.* 34 (1997) 829-834.
- [62] Christl, I., Kretzschmar, R., *Geochim. Cosmochim. Acta* 65 (2001) 3435-3442.
- [63] Courdouan, A., Christl, I., Rabung, T., Wersin, P., Kretzschmar, R., *Environ. Sci. Technol.* 42 (2008) 5985-5991.
- [64] Lippold, H., Evans, N.D.M., Warwick, P., Kupsch, H., *Chemosphere* 67 (2007) 1050-1056.
- [65] Marquardt, C.M. (Ed.), "Migration of actinides in the system clay, humic substances, aquifer", *Wiss. Berichte FZKA 7407*, Karlsruhe 2008.
- [66] Akitt, J.W., Greenwood, N.N., Khandelwal, B.L., Lester, G.D., *J. Chem. Soc., Dalton Trans.* (1972) 604-610.
- [67] Hoehn, E., Eikenberg, J., Fierz, T., Drost, W., Reichlmayr, E., *J. Contam. Hydrol.* 34 (1998) 85-106.
- [68] Schikora, J., Diploma Thesis, Dresden Technical University, 2012, in preparation.
- [69] Van Loon, L.R., Baeyens, B., Bradbury, M.H., *Appl. Geochem.* 20 (2005) 2351-2363.
- [70] Garcia-Gutierrez, M., Cormenzana, J.L., Missana, T., Mingarro, M., Martin, P.L., *Phys. Chem. Earth* 31 (2006) 523-530.
- [71] Arson, C., Gatmiri, B., *Phys. Chem. Earth* 33 (2008) S407-S415.
- [72] Savoye, S., Page, J., Puente, C., Imbert, C., Coelho, D., *Environ. Sci. Technol.* 44 (2010) 3698-3704.
- [73] Jougnot, D., Revil, A., Lu, N., Wayllace, A., *Water Resour. Res.* 46 W08514 (2010) 1-17.

Berichtsblatt

1. ISBN oder ISSN geplant	2. Berichtsart Abschlussbericht
3a. Titel des Berichts „Contributions to modelling actinide transport in potential host rock formations: Elementary processes and influence of heterogeneous structures“	
3b. Titel der Publikation geplant (Das Projekt war Bestandteil des Verbundvorhabens „Wechselwirkung und Transport von Actiniden im natürlichen Tongestein unter Berücksichtigung von Huminstoffen und Tonorganika“. Die Abschlussberichte zu den einzelnen Projekten werden im Rahmen eines zusammenfassenden Gesamtberichtes durch KIT veröffentlicht.)	
4a. Autoren des Berichts (Name, Vorname(n)) Lippold, Holger Kulenkampff, Johannes Gründig, Marion Zakhnini, Abdelhamid	5. Abschlussdatum des Vorhabens 30.06.2011
	6. Veröffentlichungsdatum 2012 (geplant)
4b. Autoren der Publikation (Name, Vorname(n)) Marquardt, Christian M. (Hrsg.)	7. Form der Publikation KIT-Bericht
8. Durchführende Institution(en) (Name, Adresse) Helmholtz-Zentrum Dresden-Rossendorf (HZDR) Institut für Radiochemie Forschungsstelle Leipzig* Permoserstr. 15 04318 Leipzig * bis Dezember 2009: Institut für Interdisziplinäre Isotopenforschung (IIF)	9. Ber.-Nr. durchführende Institution
	10. Förderkennzeichen ^{*)} 02E10176
	11a. Seitenzahl Bericht 71
	11b. Seitenzahl Publikation
13. Fördernde Institution (Name, Adresse) Bundesministerium für Wirtschaft und Technologie (BMWi) 11019 Berlin	12. Literaturangaben 73
	14. Tabellen 4
	15. Abbildungen 52
16. Zusätzliche Angaben 3 weitere Veröffentlichungen sind in wissenschaftlichen Fachzeitschriften erschienen.	
17. Vorgelegt bei (Titel, Ort, Datum)	
18. Kurzfassung Die Wirksamkeit geologischer Barrieren im Umfeld eines Endlagers beruht auf ihrem hydraulischen Abdichtvermögen und ihren chemischen Rückhalteeigenschaften. Tongestein als mögliche Wirtsfornation zeichnet sich durch eine besonders hohe Adsorptionskapazität gegenüber radioaktiven Schwermetallen (z.B. Actiniden) aus. Durch deren Wechselwirkung mit mobilen organischen Bestandteilen natürlicher Tone (Huminstoffe, Carbonsäuren) kann diese Funktion jedoch unterwandert werden. Generell kann auch die heterogene Struktur geologischer Matrices zu einem beschleunigten Transport führen. Im Rahmen des Projektes wurde die Datenbasis zur Bewertung des Rückhaltevermögens von Tonen in Abhängigkeit von geochemischen Randbedingungen wesentlich erweitert. Dabei ermöglichte der Einsatz von Radiotracer die Einstellung adäquater Konzentrationsverhältnisse. Einer Mobilisierung von Metallen durch Desorption infolge pH-Wert-Abnahme wird durch die Präsenz von Tonorganika prinzipiell entgegengewirkt. Ein Schwerpunkt lag auf der Verbesserung des Grundverständnisses der mobilitätsbestimmenden Prozesse als Voraussetzung für die Entwicklung von Transportmodellen. Dies betrifft insbesondere den Gleichgewichtscharakter von Wechselwirkungs- und Adsorptionsvorgängen sowie deren Verknüpfung zur Beschreibung komplexer Systeme anhand weniger Parameter. Abweichend von gleichgewichtsthermodynamischen Modellansätzen ist die Huminstoffkomplexbildung mehrwertiger Metalle durch langsame Stabilisierungsprozesse gekennzeichnet, die näher charakterisiert werden konnten. Das Vorliegen dynamischer Adsorptionsgleichgewichte gemäß üblicher Modellannahmen konnte für Huminstoffe erstmals nachgewiesen werden. Durch die methodische Erschließung der Positronen-Emissions-Tomographie als Radiotracerverfahren für orts- und zeitauflösende Transportstudien an geologischen Probekörpern wurden grundlegend neue Erkenntnisse zu Fließverhalten und Stoffausbreitung in möglichen Barrierematerialien (Tone, Kristallingestein) gewonnen. Zur Minimierung von Bildartefakten wurden Monto-Carlo-Simulationen durchgeführt. Das Ausbreitungsverhalten in realen, druckentlasteten Tonbohrkernen stellt sich deutlich komplizierter dar als reine molekulare Diffusion. Untersuchungen an klüftigem Granit haben ergeben, dass sich oft stark lokalisierte Transportpfade ausbilden und damit nur ein geringer Teil des verfügbaren Hohlraumvolumens genutzt wird.	
19. Schlagwörter Adsorption, Diffusion, Endlager, Granit, Huminstoffe, Komplexbildung, Kristallingestein, Metalle, Migration, Mobilisierung, Radioaktiver Abfall, Radionuklide, Rückhaltung, Sicherheitsbewertung, Tomographie, Ton, Tonorganika, Transport	
20. Verlag Karlsruher Institut für Technologie (KIT)	21. Preis

^{*)} Auf das Förderkennzeichen des BMBF soll auch in der Veröffentlichung hingewiesen werden.

Document Control Sheet

1. ISBN or ISSN planned	2. Type of Report Final Report
3a. Report Title "Contributions to modelling actinide transport in potential host rock formations: Elementary processes and influence of heterogeneous structures"	
3b. Titel of Publication planned (The project was part of the joint project "Interaction and transport of actinides in natural clay rock considering humic substances and clay organics". The final reports of the individual projects will be published within the framework of a comprising report by KIT.)	
4a. Author(s) of the Report (Family Name, First Name(s)) Lippold, Holger Kulenkampff, Johannes Gründig, Marion Zakhnini, Abdelhamid	5. End of Project 30 June 2011
	6. Publication Date 2012 (planned)
4b. Author(s) of the Publication (Family Name, First Name(s)) Marquardt, Christian M. (Ed.)	7. Form of Publication KIT Report
8. Performing Organization(s) (Name, Address) Helmholtz-Zentrum Dresden-Rossendorf (HZDR) Institute of Radiochemistry Research Site Leipzig* Permoserstr. 15 04318 Leipzig Germany * until December 2009: Institute of Interdisciplinary Isotope Research (IIF)	9. Originator's Report No.
	10. Reference No. 02E10176
	11a. No. of Pages Report 71
	11b. No. of Pages Publication
13. Sponsoring Agency (Name, Address) Bundesministerium für Wirtschaft und Technologie (BMWi) (Federal Ministry of Economics and Technology) 11019 Berlin Germany	12. No. of References 73
	14. No. of Tables 4
	15. No. of Figures 52
16. Supplementary Notes 3 further publications appeared in peer-reviewed scientific journals.	
17. Presented at (Title, Place, Date)	
18. Abstract The efficiency of geological barriers in the environment of a final repository is based on their hydraulic sealing capabilities and chemical retention properties. Clay rock as a possible host formation is characterized by a very high adsorption capacity for radioactive heavy metals (e.g., actinides). Interaction of metals with mobile organic constituents of natural clays (humic substances, organic acids) may, however, affect this barrier function. The heterogeneous structure of geological matrices in general may cause accelerated transport as well. Within the framework of the project, the database for an assessment of the retention capabilities of clays in dependence on geochemical conditions was considerably extended. Application of radiotracers allowed studies at adequate concentrations. A mobilization of metals by desorption in consequence of acidification is generally counteracted in the presence of clay organics. A major focus was set on an improvement of basic process understanding as a prerequisite for the development of transport models. In particular, the equilibrium character of interaction and adsorption processes was considered, as well as their combination for describing complex systems by means of few parameters. Deviating from modelling approaches on the basis of equilibrium thermodynamics, humate complexation of higher-valent metals is characterized by slow stabilization processes, which were investigated in detail. For humic substances, the existence of dynamic adsorption equilibria (according to common modelling assumptions) could be demonstrated for the first time. By utilizing Positron Emission Tomography as a radiotracer method for space- and time-resolved transport studies with geological samples, fundamental new insights were gained in respect of flow behaviour and mass transport in possible barrier materials (clays, crystalline rock). Monte Carlo simulations were conducted in order to minimize image artifacts. Propagation in real, decompressed drill cores of clay turned out to be much more complicated than pure molecular diffusion. Investigations with jointed granite have shown that strongly localized transport paths often develop. Thus, only a minor fraction of the available void volume is used.	
19. Keywords Adsorption, Clay, Clay Organics, Complexation, Crystalline Rock, Diffusion, Final Repository, Granite, Humic Substances, Metals, Migration, Mobilization, Radioactive Waste, Radionuclides, Retention, Safety Assessment, Tomography, Transport	
20. Publisher Karlsruhe Institute of Technology (KIT)	21. Price